



UNIVERSITÀ
DEGLI STUDI
FIRENZE

DOTTORATO DI RICERCA IN FISICA E ASTRONOMIA

CICLO XXIX

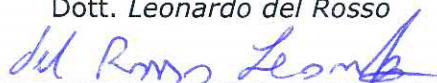
COORDINATORE Prof. Massimo Gurioli

A compound of water and molecular hydrogen giving rise to a new porous water structure

Settore Scientifico Disciplinare FIS/03

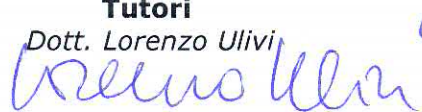
Dottorando

Dott. Leonardo del Rosso

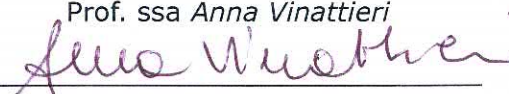


Tutori

Dott. Lorenzo Ulivi

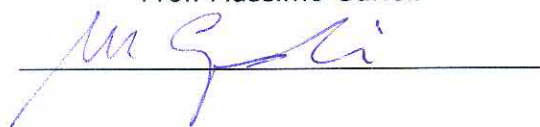


Prof. ssa Anna Vinattieri



Coordinatore

Prof. Massimo Gurioli



Anni 2013/2016

*Alla mia famiglia,
a Martina*

*“Non so perché, ma lui mi piace. E’ indiscutibilmente
una bella musica. Deve essere così.”*
[Shiigi Munenori]



Contents

Introduction	1
I The physical system	7
1 The polymorphism of ice	9
1.1 The structure of ice <i>Ih</i>	10
1.2 The other phases of ice	14
2 High pressure gas hydrates	21
2.1 Clathrate and filled ice	22
2.2 Hydrogen hydrates	25
2.2.1 Hydrogen clathrate-hydrate	27
2.2.2 Hydrogen filled ices	31
2.2.3 The stable C_0 -phase	32
2.3 The thermodynamic stability of emptied structure	33
II Experimental methods	35
3 Synthesis of the sample in the C_0-phase	37
3.1 High pressure apparatus	37
3.2 Sample synthesis and recovering	39

4	Raman spectroscopy	41
4.1	The Raman effect	41
4.1.1	Vibrational Raman spectroscopy on molecules	44
4.1.2	Vibrational Raman spectroscopy on crystals	47
4.2	Raman apparatus	50
4.2.1	Calibration of the spectrometer	53
5	Neutron scattering	57
5.1	The scattering law	59
5.2	Neutron diffraction	63
5.3	Inelastic neutron scattering from the hydrogen molecule	67
5.4	Neutron spectrometer: TOSCA	70
5.4.1	Scientific case: the clathrate-hydrates on TOSCA	74
5.5	Neutron diffractometers: OSIRIS and WISH	76
III	Experimental results and discussion	83
6	Raman data of the C₀-phase and ice XVII	85
6.1	The Raman characterization of the C ₀ -phase	85
6.2	The annealing treatment and the discovery of ice XVII	91
6.3	The porosity of ice XVII	95
6.3.1	Quantitative study on hydrogen adsorption	96
6.3.2	Ortho-para conversion	103
6.3.3	Metastability of ice XVII	106
7	Neutron spectroscopy on ice XVII	109
7.1	Lattice vibrational modes in ice XVII	112
7.2	The hydrogen dynamics in refilled ice XVII	114

8	Experimental results on structure	119
8.1	Preliminary X-rays structural check of pristine sample	119
8.2	Structure refinement of ice XVII	120
8.3	Structural studies on filled ice	129
8.3.1	The C ₀ -phase filled ice as synthesized	129
8.3.2	Refilled ice XVII	138
8.4	Single molecule potential in filled ice	140
9	Conclusions	143
	Bibliography	147



Introduction

The study of the structure and the dynamics of the solid binary mixtures of water and molecular hydrogen has large interest, both for the comprehension of fundamental aspects, related to the quantum behaviour of the confined hydrogen molecules, and for applicative aspects, related to the characterization of new compounds suitable for technological applications, among which the hydrogen storage is surely the most suggestive.

The purpose of this thesis is to present the main experimental results concerning one phase of this solid mixture synthesized at 400 MPa and 255 K, and its behaviour when a thermal annealing treatment is applied, up to the complete release of hydrogen gas and to the formation of a new form of ice, namely *Ice XVII*.

The binary system H_2 - H_2O exhibits several crystalline stable phases, depending on the range of pressure and temperature considered. A possible solid form of this mixture is the clathrate-hydrate (sII-structure) [1], which is stable at pressure higher than 100 MPa. Other stable phases have the form of the so-called filled ice, found with the C_1 and C_2 structure [2], which are stable at higher pressure, namely at values higher than 0.7 and 2.3 GPa, respectively. Only recently two experimental studies [3, 4] have discovered a new phase of the hydrogen-water system, named C_0 -phase filled ice, that is stable in the intermediate thermodynamic region between sII clathrate and C_1 -phase filled ice. The structure of the C_0 -phase has never been completely

resolved, because only X-rays data are available and their interpretation has been quite ambiguous [5, 6]. Also the dynamic characterization of this phase was not exhaustive at the moment of the start of this study [4, 6].

So, given the state of art in this field of research, the initial aim of our work has been the study of the hydrogen filled ice compound in the C_0 -phase. In our high-pressure laboratory (ISC-CNR, Italy) we have been able to synthesize this compound, and to recover it at room pressure and liquid nitrogen temperature. Then we have performed a complete *ex situ* Raman characterization of the vibrational motions of both the host and guest molecules in the C_0 -structure.

Low density solid water structures, as those formed by clathrate-hydrates, have risen large interest since the discovery in 2014 of ice XVI, a new form of ice which is obtained by emptying a sII neon clathrate hydrate [7]. Furthermore, an empty clathrate structure, named sIII, has been theoretically proposed as a stable phase of water under negative pressure [8]. These works strongly contribute to the discussion about the role of the guest molecule in the stabilization of the hydrate structure. In this perspective, after the study of the filled ice sample as synthesized, we have applied a thermal annealing treatment, i.e. to keep the sample at a temperature of about 110 K under dynamic vacuum for about 1 hour, in order to study the possibility of removing H_2 guest molecules from the H_2O host framework. By means of Raman spectroscopy we have verified that all the hydrogen molecules contained in the sample have been removed by the described treatment, and only slight structural modifications on the H_2O framework, inferred by dynamics data, have occurred. Thus, in this way, we have verified the mechanical stability of the emptied C_0 -structure, that is metastable up to 130 K. As a matter of fact, this is a new metastable form of water ice, and we have called it *Ice XVII*, according to the actual nomenclature for the crystalline phases of ice (see Endnote A).

A really interesting and surprising property of this new form of ice is its porosity, i.e. its capacity of adsorbing gas, even at pressure well below the atmospheric one. By using Raman spectroscopy, we have measured the adsorption and desorption isotherms at several different temperatures, demonstrating the reversibility of this adsorption process. This property sheds new light on possible future applications in the hydrogen storage field [9, 10]. Anyway this aspect is out of the scope of the thesis work.

Another dynamic characterization has been performed by using TOSCA spectrometer (ISIS facility, RAL, U.K.), measuring the vibrational dynamics of the guest hydrogen molecule inside the pristine C_0 -structure and in ice XVII, obtained after the same annealing treatment mentioned above. The refilling has been made with two different mixture of hydrogen, one ortho-rich and one para-rich, in order to facilitate the assignment of the observed spectral bands.

The structure of our samples has been investigated by neutron diffraction. A first structural characterization of the pristine sample has been performed by WISH diffractometer (ISIS facility, RAL, U.K.). In this case, the presence of spurious guests inside the water structure, as nitrogen molecules, adsorbed by the sample during its handling in the liquid nitrogen bath, prevents the refinement of this structure. The determination of the structure of D_2O ice XVII has been done by means of neutron diffraction measurements, performed on OSIRIS diffractometer (ISIS facility, RAL, U.K.). We have studied the temperature dependence of the lattice parameters in the range of stability of this solid phase, and also performed some diffraction measurements on ice XVII after a refilling with hydrogen, obtaining a quantitative behaviour of the lattice parameter as a function of hydrogen content (see Endnote B). We used OSIRIS and a sample containing H_2 instead of D_2 because we aimed to measure also quasi-elastic scattering for studying the H_2 diffusive motion. Moreover by means of OSIRIS data we cannot draw any conclusion about the true structural

symmetry of the refilled sample, since a complete set of diffraction data on a fully deuterated sample has not been measured yet.

The subjects just introduced above will be developed in this thesis, which is divided into three parts, devoted, respectively, to the introduction of the scientific case, to the description of the experimental methods and to the discussion of the experimental results, following the chapters scheme reported below:

- In the first chapter we recall the polymorphism of ice by means of a description of the water phase diagram, discussing the role played by the proton-disorder and the metastability in the different forms which ice may assume.
- In the second chapter we give a description of the high pressure gas hydrates, namely clathrates and filled ices, recalling in detail the properties of these solid inclusion compounds in the case of the binary system H_2 - H_2O , and the description of a new form of metastable ice, namely ice XVI, obtained by completely removing the guest molecules from the sII neon clathrate.
- The experimental methods used for the study of the C_0 -phase of hydrogen filled ice and of ice XVII, obtained by an annealing treatment of the pristine filled ice sample, are illustrated in the third, fourth and fifth chapters. In particular we describe the experimental apparatus used for the high pressure synthesis and sample recover, and the experimental techniques, i.e. Raman and neutron spectroscopy, and neutron diffraction, used for the dynamical and structural characterization of the sample.
- The results concerning the sample dynamics, obtained by means of Raman and neutron spectroscopy, are discussed in the sixth and seventh

chapters. Moreover, after the description of the annealing procedure applied on the pristine sample to produce ice XVII, we show the dynamic properties of this new form of ice, showing also a quantitative study about its capacity of hydrogen adsorption.

- Lastly, in the eighth chapter, we discuss the neutron diffraction measurements performed to resolve the crystalline structure of ice XVII and to study the structural behaviour during annealing and refilling of ice XVII.

Endnotes

- A** The discovery of the new form of ice, together with the complete Raman characterization of the C₀-phase, empty C₀-structure (ice XVII) and the quantitative study about its adsorption capacity, have been recently published:

del Rosso, L., Celli, M. & Ulivi, L. New porous water ice metastable at atmospheric pressure obtained by emptying a hydrogen-filled ice. *Nature Communication* **7**, 13394 (2016). DOI: 10.1038/ncomms13394

- B** All the results about the structural characterization obtained by OSIRIS data are the subject of a recent publication:

del Rosso, L., Grazzi, F., Celli, M., Colognesi, D., Garcia-Sakai, V. & Ulivi, L. Refined structure of metastable ice XVII from neutron diffraction measurements. *The Journal of Physical Chemistry C* (2016). DOI: 10.1021/acs.jpcc.6b10569

Part I

The physical system



Chapter 1

The polymorphism of ice

Ice is the most common crystalline substance on Earth and it is omnipresent, both on the surface and in the atmosphere of our planet. Ice is ubiquitous also on other celestial bodies of the solar system, such as comets, asteroids or icy moons of the giant planets. On Earth, the presence of ice in the atmosphere is part of the delicate equilibrium between incident and emitted radiation and in this sense is essential for life. Outside Earth ice attains crystal structures that are probably different from the ice *Ih*, the usual ice. These exotic structures can be produced in a laboratory and have been studied since the beginning of last century.

Water molecule (H_2O) is one of the simplest in chemistry, however the properties of liquid water and those of ice cannot be derived consistently from one single model of the water molecule [11]. The H_2O molecule is constituted by an oxygen atom linked with two hydrogen atoms by a covalent bond, which is indicated by the symbol $\text{O}-\text{H}$. The chemical bonding that occurs between two water molecules is the hydrogen bond, and it is usually indicated by the symbol $\text{O}-\text{H}\cdots\text{O}$. It arises when a hydrogen atom lies between two highly-electronegative atoms, especially oxygen. The hydrogen atom remains covalently bound to the oxygen one, so the water molecule keeps its identity.

This bond is characterized by a binding energy intermediate between that of the covalent and the van der Waals bonds. The hydrogen bond plays the main role for shaping the properties of both the liquid and the solid, in particular it is responsible for the tetrahedral bonding of the molecules in ice.

Water exhibits several solid structures [12]. Normal ice, the solid that forms cooling water at atmospheric pressure, is indicated by *Ih* since the time (1900) when other forms of ice were discovered by Tammann [13] by the application of pressure. The suffix *h* is commonly added to distinguish this hexagonal form of ice from the cubic one *Ic*. The discussion of the crystalline structure of ice *Ih*, which will be the subject of next sections, already underline a feature which will be a leitmotiv to characterize the different forms of ice, that is, the disorder of the protons.

Among the solid forms of ice, one should count also the amorphous ices. They are characterized by having no long-range order, as in the liquid phase, but with a frozen molecular arrangement. They can be formed at liquid nitrogen temperature by vapour deposition or pressurizing ice *Ih* or *Ic* at about 1 GPa. Making reference to the density of ice *Ih* (about 0.92 g cm^{-3} at standard pressure), they are classified in two main groups, the low-density amorphous ice, with a density at atmospheric pressure of about 0.94 g cm^{-3} , and the high-density amorphous, whose recovered samples have a density of about 1.17 g cm^{-3} .

1.1 The structure of ice *Ih*

The structural model for ice *Ih* was proposed by Pauling in 1935 [14]. The oxygen atoms occupy the crystallographic sites of a hexagonal lattice, and each water molecule is linked tetrahedrally with four other molecules of water by means of hydrogen bonds. A drawing of *Ih* structure is reported in Figure

1.1. In this model there is no long-range order in the orientations of water

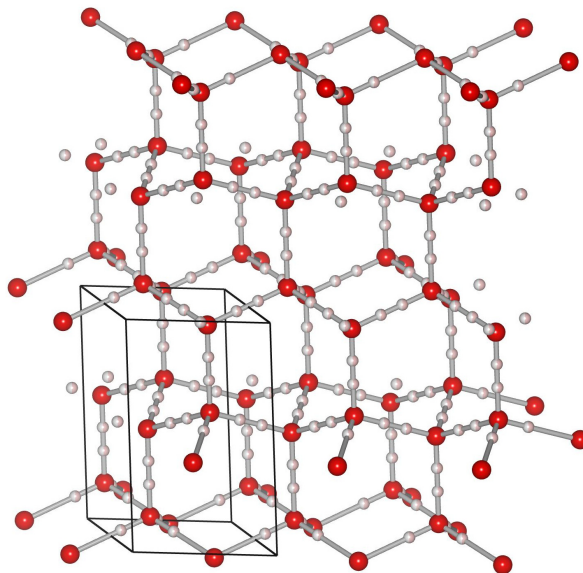


Figure 1.1: *Prospective drawing of the structure of ice Ih, produced with software VESTA [15]. Each hydrogen crystallographic site is half-occupied to take into account the disordered nature of the Ih ice form.*

molecules, i.e. the positions of the protons in the ice crystal lattice have no spatial periodicity, and for this reason the structure of the common ice Ih is defined *disordered*. Along each hydrogen bond between two adjacent oxygen atoms there are two possible sites for the protons, while around each oxygen atom four possible sites for protons are present. These sites are occupied randomly by hydrogen atoms, and the average structure can be described by an half-hydrogen model, in which each hydrogen crystallographic site is half-occupied. This approach is usually adopted in the traditional crystallography, and the orientational disorder of the water molecules, which results from the proton disorder, is often neglected during structural refinements. The disorder has a static (structural) character and is not due to the quantum properties of the hydrogen nucleus, as instead happens for the electron in the benzene

molecule. The amplitude of the zero-point motion of a proton is only 0.1 Å, so that individual molecules retain their identity. However, the positions of the hydrogen atoms in the lattice must be compatible with the so-called Bernal-Fowler (BF) rules [16]: (1) each oxygen atom is covalently bound to two atoms of hydrogen; (2) there must be one and only one hydrogen atom on each hydrogen bond.

The proton disorder contributes to the entropy of ice, which has a non-zero value at $T = 0$, and which can be calculated with simple considerations. The energy of the water crystal is almost the same for any configuration of hydrogen atoms consistent with the BF rules. We recall here that in a thermodynamic system, the entropy S is expressed by the Boltzmann relation

$$S = k_B \ln W \quad (1.1)$$

where k_B is the Boltzmann constant and W is the number of possible configurations that the system can assume. For an estimation of this number, let's consider an ice crystal consisting of N water molecules, with $N \gg 1$ (this will allow us to ignore the effect of the crystal surfaces). Each water molecule can assume six different and equally probable orientations in the lattice and there are $2N$ hydrogen bonds. Ignoring for the moment the second BF rule, there are 6^N possible arrangements of N molecules. Considering all these arrangements, one gives rise to four types of bonds between two adjacent molecules (i.e. HH, H-, -H, - -, where H and - indicate the presence or absence of hydrogen in the site). Only two out of four satisfy the second BF rule, so there is a probability of $(\frac{1}{2})^{2N}$ that all bonds are correct. The total number of acceptable configurations W of the crystal is therefore given by

$$W = 6^N \left(\frac{1}{2}\right)^{2N} = \left(\frac{3}{2}\right)^N, \quad (1.2)$$

and, for one mole of ice, the entropy yields

$$S = N_A k_B \ln \left(\frac{3}{2}\right) \simeq 3.371 \text{ J K}^{-1} \text{ mol}^{-1}. \quad (1.3)$$

According to the third law of thermodynamics, lowering the temperature there should be a transition toward a more ordered phase, in which the water molecules adopt the energetically most favoured orientations. However, this transition does not occur in pure ice Ih. In fact, even if this transition is thermodynamically accessible, it is not kinetically favoured because of the highly cooperative nature of molecular reorientation in ice, preventing these ordering transition to occur.

The presence of some defects in the lattice can play a key role in facilitating the ordering process. Any violation of the BF rules is called defect and a schematic view is shown in Figure 1.2. In particular, if ions H_3O^+ and/or OH^- are present in the crystal (i.e. violation of the first BF rule) the defect is called ionic, while if between two oxygen atoms there are two or no hydrogen atoms (i.e. violation of the second BF rule) the defect is called orientational or Bjerrum, of type D or L respectively. In the presence of a defect, the adjacent

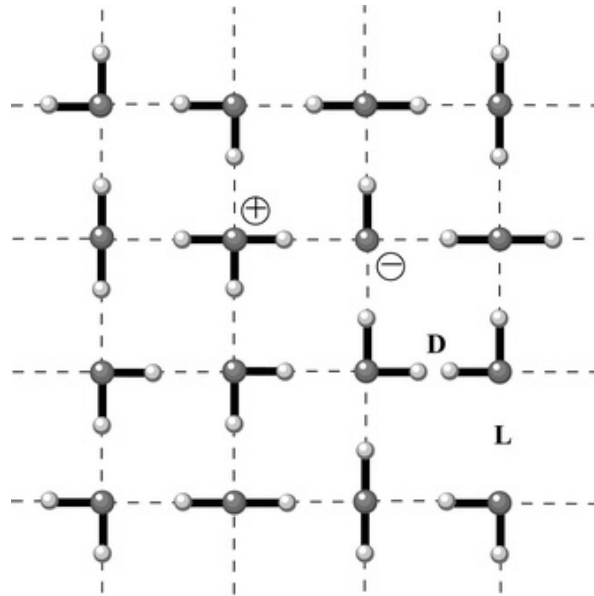


Figure 1.2: *Schematic 2D drawing of water crystal structure. The symbols + and - indicate the ionic defects H_3O^+ and OH^- , while the letters D and L indicate the orientational defects.*

water molecules can in turn reorient themselves, hence causing the migration of the defect along the various lattice sites. The concentration of the defects is related to the temperature of the solid and their presence implies a higher energy for the crystal. At high temperatures the defects diffuse in the crystal structure. On the contrary, at low temperatures the defects have less mobility, hence any ordering process is prevented and the proton disorder is frozen. As a matter of fact, the system is in an equilibrium state characterized by a relative minimum of the free energy. At low temperature, a complete proton order cannot be achieved in the crystal structure, since the available thermal energy is not sufficient to overcome the potential barrier that separates the disordered phase from the ordered one. In other words, the ordering process would have a very long kinetics, related to phenomena of quantum tunnelling, making it experimentally not observable. For promoting the ordering process, it is necessary to increase the number of defects by doping the ice with strong acids or bases, with a concentration low enough to not affect the crystal structure of the ice. In this way the potential barrier is drastically lowered and the process can be thermally activated, with a relatively fast kinetics, that makes the disorder-order transition experimentally observable.

1.2 The other phases of ice

Nowadays at least seventeen different ice forms have been discovered. Those crystalline phases, whose existence has been experimentally demonstrated, are conventionally labelled in the chronological order of discovery by Roman numbers.

The ice phases, characterized by different molecular arrangements, can be classified depending on their thermodynamic state (stable or metastable), disposition of the hydrogen atoms in the water lattice (proton ordered or disor-

dered) or structure (crystalline or amorphous). A schematic phase diagram of water is reported in Figure 1.3, while all the known crystalline phases are summarized in Figure 1.4. The solid lines, that delimit the thermodynamic

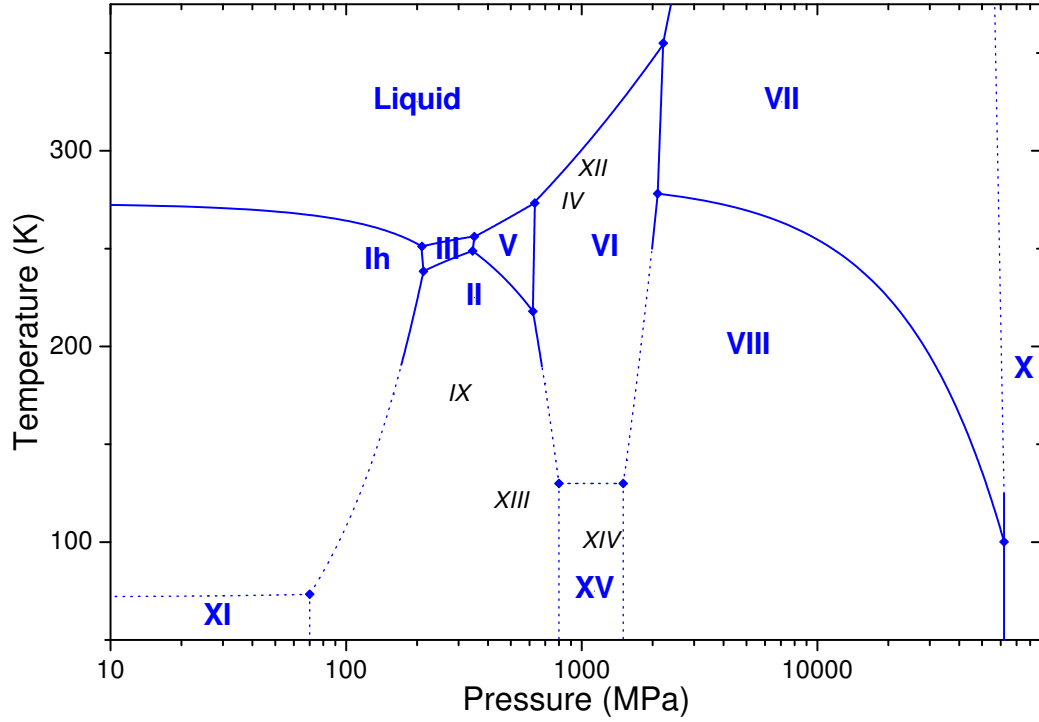


Figure 1.3: *The phase diagram of water in semi-logarithm scale [17, 18]. The symbols represent the triple points, while the solid and dashed lines represent, respectively, the experimentally determined and the extrapolation of the two-phase equilibrium lines. The blue labels indicate the stable phases, while the metastable phases are labelled in black italic font with smaller size.*

range of stability of the different ice phases, indicate the thermodynamic condition for which the two phases are in equilibrium with one another. The intersection points of these lines are the triple points, where three phases of water are in equilibrium. Along the phase boundary lines, the value of the Gibbs free energy is the same for either phase. This consideration leads to some constraints concerning the slope of the phase lines, that are expressed by

the Clausius-Clapeyron equation

$$\frac{dT}{dP} = \frac{\Delta V}{\Delta S}, \quad (1.4)$$

where ΔV and ΔS are the difference in volume and entropy between equal amounts of the two phases considered, respectively. The negative slope of the liquid-Ih line reflects the lower density of this solid phase compared to the liquid one, while the positive slope of the melting line of other phases of ice indicates that these (high-pressure) ice phases have a density higher than the liquid. Considering the transition line between two solid phases, the proton-order of the ice structures has to be taken into account. Indeed the equilibrium line between two structures with a similar value of entropy ($\Delta S \simeq 0$), i.e. either ordered or disordered, is almost vertical, while the line is tilted if this is the boundary between a disordered and ordered ice form.

The stability and metastability of ice For a given value of pressure P and temperature T , more than one ice structure can be obtained, and each one is characterized by the Gibbs free energy $G(P, T) = U + PV - TS$. The phase with the lowest value of $G(P, T)$ is the stable one, while the others are called metastable. Several ice forms (e.g. Ic [19], IV [20], IX [21], XII [22] and amorphous [12]) have no stability region but can be formed following a particular thermodynamic path or by means of nucleating agents. The cubic ice Ic, for example, is a metastable variant of ice Ih in which the crystalline structure has a cubic symmetry. It is obtained by vapour deposition between 130 and 150 K or by heating between 120 and 170 K of any high-pressure ice phase, once it is recovered at room pressure in liquid nitrogen bath. Ice Ic transforms completely into ice Ih at about 200 K, while the inverse transformation does not occur.

Moreover, some forms of ice, stable at high pressure, are metastable well outside their thermodynamic stability region. Usually these ice forms can be

Disordered ice phase	Ordered ice phase	Notes
I _h	XI	Basic dopant (KOH) necessary for promoting the ordering
I _c	-	
-	II	
III	IX	Doping not necessary for ordering
IV	-	
V	XIII	Acid dopant (HCl) necessary for promoting the ordering
VI	XV	Acid dopant (HCl) necessary for promoting the ordering
VII	VIII	Doping not necessary for ordering
	X*	Symmetric hydrogen bonds
XII	XIV	Acid dopant (HCl) necessary for promoting the ordering
XVI	-	Emptied sII-phase (neon clathrate-hydrate)
XVII	-	Emptied C ₀ -phase (hydrogen filled ice)**

*Sometimes this phase is not classified as ordered.

**This phase is the subject of the present work.

Figure 1.4: *Summary scheme of the actually known crystalline forms of solid water. The various phases are grouped in the disordered-ordered ice pairs.*

recovered at room pressure and at liquid nitrogen temperature, allowing one to study them easily with different experimental techniques, even outside a pressure cell. In this case the metastability is due to the low temperature that hinders the process of transformation into the stable phase.

Only recently another form of metastable ice (XVI) has been produced by emptying a sII neon clathrate [7]. This topic will be treated in the next chapter.

The ordered forms of ice Ice XI is the ordered form of ice *I_h*, which is produced by cooling below the transition temperature (72 K) a sample of KOH-doped ice *I_h*. Ice XI was first observed by Kawada et al. [23] by means of measurements of dielectric permittivity, while only later calorimetric [24] and diffraction measurements [25] gave a detailed description of this form of ice. Recently new forms of ordered ices, namely ice XIII, XIV and XV have been discovered by doping ices V, XII and VI, respectively, with hydrochloric acid [26, 27]. The phenomenon of the proton ordering was also observed in simple clathrates of THF (tetrahydrofuran) by means of calorimetric and dielectric techniques [28, 29]. Anyway there are other forms of ice that are characterized by a proton-ordered crystal structure, i.e. ice II, VIII, IX, and these are obtained without involving any chemical doping [21, 30, 31]. All the disordered-ordered ice pairs are summarized in Figure 1.4.

The symmetric hydrogen bond Also ice X is sometimes classified as an ordered form of ice [32]. Anyway, in this case, due to the extreme condition necessary for its stability (pressures higher than 100 GPa), the water molecules in the crystal lattice are so close to each other that the hydrogen bonds are symmetrized, i.e. the two possible sites for a proton on a hydrogen bond are merged into one at the center of the bond, thus the protons on the hydrogen bonds lie in a single potential well. Another case of symmetric ice is represented

by ice VII [31], even if this form is proton-disordered. Indeed the hydrogen bonds in ice VII are characterized by a shallow double potential well and the proton may be delocalized thermally or quantum mechanically, e.g. by means of zero-point motion or tunnel effect, thus causing the bond symmetrization.

Chapter 2

High pressure gas hydrates

The term “gas hydrate” indicates a wide family of solid and non-stoichiometric compounds of hydrogen-bonded water molecules (host) and hydrophobic species (guest), typically atomic gas like He, Ne and Ar or molecular gas like H₂, N₂, CH₄ and CO₂. In these compounds no hydrogen bond or other chemical bonds between guest and water molecules are involved. The guest-host interaction is driven by van der Waals and repulsive forces, well represented by means of Lennard-Jones-like potential. Typically these compounds are thermodynamically stable at pressure higher than one atmosphere and/or at lower temperature than ambient temperature.

Historically the discovery of hydrates occurs at the begin of 19-th century as a scientific curiosity [33]. More recently the hydrates have aroused interest in many fields. The discovery that gas hydrates could create plugs in gas pipelines, even at temperatures above the ice point [34], has driven an intense research activity for application in the natural gas industry. Also the geophysicists have shown interest in these compounds, since the discovery of hydrates in permafrost [35] and ocean depth [36]. In the last decades it has been supposed that natural gas hydrates could be present also on extraterrestrial objects, e.g. Mars, Saturn or comets [37].

2.1 Clathrate and filled ice

Clathrate-hydrates are crystalline inclusion compounds in which a water host lattice traps small guest atoms or molecules in polyhedral cavities, usually called *cages* [38]. The water molecules in the lattice are tetrahedrally coordinated and connected by hydrogen bonds as in ordinary ice. The oxygen atoms constitute the vertices of the polyhedron while each edge corresponds to a hydrogen bond between two adjacent water molecules. Considering a single generic cage, each water molecule has three links towards other molecules of the same cage, while the fourth bond links it with one molecule not belonging to the same cage. In the following the polyhedra are indicated using the Jeffrey notation, which for a pentagonal dodecahedral cage reads 5^{12} , and for a hexakaidecahedral cage constituted by twelve pentagonal faces and four hexagonal faces reads $5^{12}6^4$.

Different types of clathrate cages, represented in Figure 2.1, may form, depending on the dimensions and shape of the guest molecules. The stability of the cavity is provided by the repulsive component of the guest-host interaction and by the attractive forces between water molecule belonging to adjacent cavities. The presence of some empty cavities doesn't affect the stability of the whole crystalline structure [7, 39], leading to non-stoichiometric compounds. This issue will be discussed in detail at the end of this chapter. Generally, for a given value of pressure, the solidification temperature of a clathrate is higher than that of pure water at the same pressure. For example, at room pressure, the solidification of a liquid solution of water and THF occurs at about $+4^{\circ}\text{C}$. The synthesis of a clathrate of a given gas can be facilitated by the presence of a second type of guest molecule, usually called *promoter*, that fills the larger cages of a given structure and gives stability to it, thus lowering significantly the synthesis pressure. The clathrate that contains only one specie of guest is called *simple*, while if two species of guest are trapped, the clathrate is called

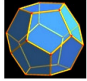
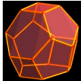
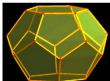
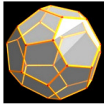
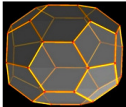
	Geometry	Jeffrey notation	Average cavity radius (Å)
	Pentagonal dodecahedron	5^{12}	3.9
	Irregular dodecahedron	$4^3 5^6 6^3$	4.0
	Tetrakaidecahedron	$5^{12} 6^2$	4.3
	Hexakaidecahedron	$5^{12} 6^4$	4.7
	Icosahedron	$5^{12} 6^8$	5.8

Figure 2.1: *Shape of the most common cavities in gas clathrate-hydrate [38]. The average cavity radius will vary with temperature, pressure and guest composition.*

binary.

The type and dimension of guests also determine the crystallographic structure, which is different from that of common ice *Ih* and from those of other ice phases. Until today at least six types of clathrate structures have been experimentally determined [40, 41] or theoretically proposed [42], even at negative pressure [8]. Among the most common structures, two are cubic (sI and sII) and one is hexagonal (sH) [38, 43, 44]. Their properties are summarized in Figure 2.2. For a given guest, the hydrate structure depends also on the pressure [45]. Indeed, taking for example the case of methane hydrate, many experiments performed by means of Raman spectroscopy [46], X-rays and neutron diffraction [47, 48], have demonstrated that this type of hydrate can assume

Structure name	Lattice type	Space group	Cavity geometry	Examples of guest molecule
sI	cubic	Pm $\bar{3}$ n (no. 223)	5 ¹² 5 ¹² 6 ²	methane, carbon dioxide, hydrogen sulfide
sII	face-centered cubic	Fd $\bar{3}$ m (no. 227)	5 ¹² 5 ¹² 6 ⁴	hydrogen, nitrogen
sH	hexagonal	P6/mmm (no.191)	5 ¹² 5 ¹² 6 ⁸ 4 ³ 5 ⁶ 6 ³	iso-pentane, neohexane

Figure 2.2: *Main clathrate structures of natural gas clathrate. The number in parenthesis in the space group column refers to the International Table for Crystallography [49].*

three different structures, depending on the pressure applied in the synthesis process. At room temperature, in the range of pressure between 20 MPa and 120 MPa, the methane clathrate is characterized by the sI crystalline structure, while at higher pressure, i.e. over 500 MPa and 600 MPa, the methane hydrate has the sII and sH structure, respectively.

At very high pressure, i.e. about 1 GPa or above, the stable structure of many gas hydrate does not correspond to any clathrate structure, but is the so called filled ice one. In this type of inclusion compound the cage structure, typical of clathrate, is substituted by an ice-related one, whose voids are filled by guests (atoms or molecules). In many case, e.g. with CH₄, N₂, Ar and Kr as guests, the structure of filled ice is similar to the common *Ih* [50], though

other forms of ice can be obtained, e.g. the proton-ordered ice II with He as guest atom [51]. On the contrary, in particular conditions hydrogen filled ice has a peculiar structure. Hydrogen hydrates will be widely illustrated in the next section.

2.2 Hydrogen hydrates

The discovery of hydrogen hydrate is quite recent [1, 52] and in the last two decades they have been widely studied, mainly for energetic application. Indeed many efforts were addressed for hydrogen storage applications [53, 54], since these compounds are able to trap hydrogen in molecular form and to release it without involving any chemical reaction. Furthermore, using promoting molecules, e.g. THF, it is possible to synthesize these compounds at moderate pressure (about 5 MPa) even if this goes to the detriment of their hydrogen storing capacity. The hydrogen hydrate were studied also from fundamental physics point of view, since these compounds provide a simple example of a quantum particle trapped in 3-D non-harmonic potential [55, 56].

Depending on thermodynamic parameters, i.e. pressure and temperature, the phase diagram of the hydrogen-water mixture, reported with black line in Figure 2.3, exhibits a stable liquid phase and several stable solid compounds (Ih , sII, C_0 and C_1). It is important to note that for the binary system H_2 - H_2O there is always a coexistence of a H_2 -rich fluid phase (generally vapour), and a H_2O -rich phase (liquid or solid). So, as usual for binary system, the thermodynamic stability regions for the different phases are delimited by three-phase equilibrium lines and quadruple points. At higher temperature the H_2O -rich phase is a liquid solution of molecular hydrogen dissolved in water [57]. In this case the absolute concentration of molecular hydrogen varies with pressure and results very low, even at high pressure (about 2.5% H_2 molar ratio at

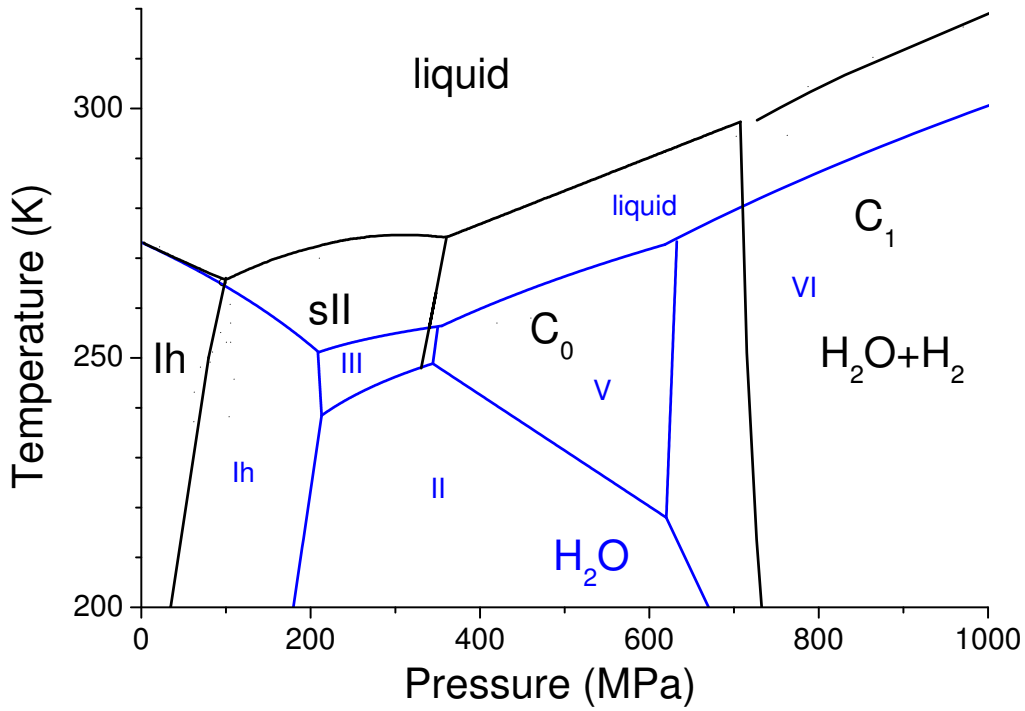


Figure 2.3: Phase diagram of the water-hydrogen mixture (black lines) and pure water [12, 58] (blue lines). The solid black lines summarize the available experimental data [2, 3, 4, 52, 59, 60, 61], and they will be discussed in next sections. The range of stability of the C_2 -phase is out of this diagram at higher pressure values.

pressure of 200 MPa and temperature of 280 K). This fact is related to the hydrophobicity of the hydrogen molecule. At low temperature, i.e. below 270 K, the H_2O -rich phase is a solid compound, whose crystalline structure depends again on pressure. Following the diagram in Figure 2.3, at the lower pressures, the stable phase is the normal hexagonal ice Ih in coexistence with hydrogen gas [60], characterised by a hydrogen concentration comparable with that of the liquid phase. The other crystalline structures are the sII clathrate and three forms of filled ice (C_0 , C_1 and C_2). The filled-ice phases will be described in detail in next sections.

Comparing the phase diagram of hydrogen-water with that of pure water (black and blue line of Figure 2.3, respectively), it is evident that, for a given values of pressure and temperature, the H_2O -rich solid phase of hydrate and pure ice do not assume the same crystal structure, since the presence of the hydrogen molecule in the hydrates deeply influences the water molecules arrangement around the H_2 molecules. Furthermore it is interesting to note the effect of guest molecule in widening the stability region of the solid phase, since the hydrogen clathrate or filled ice are also stable in a portion of liquid-phase region of pure water diagram. For example, at pressure of 200 MPa, the liquid-solid transition in the hydrate compound occurs at about 273 K, while in pure water occurs 20 K lower, i.e. 253 K. This aspect highlights the role of guest-host interactions in the stabilization of the hydrate structures under pressure.

2.2.1 Hydrogen clathrate-hydrate

The hydrogen clathrate hydrate has a sII structure, with 136 water molecules per unit cell, arranged in 16 “small cages” 5^{12} (SC), and 8 “large cages” $5^{12}6^4$ (LC) [1, 59, 62, 63]. Its synthesis requires a pressure of about 100 MPa at a temperature close to 0°C . Adding an help molecule like tetrahydrofuran, which is engaged in the large cage, the minimum pressure for the formation of this binary clathrate ($\text{THF} + \text{H}_2$) drops to about 5 MPa. Anyway, in the following we focus our attention on the H_2 simple clathrate.

The occupation of the cages by the guest molecules depends on the clathrate synthesis pressure, and at higher pressures multiple occupation of a single cage can occurs. The maximum storage level can be obtained by increasing the pressure and decreasing the temperature of clathrate synthesis. Assuming a maximum filling of 1 molecule in the SC and 4 molecules in the LC [64], the maximum amount of hydrogen stored in the clathrate, expressed as molar

percentage (i.e. the number of moles of H_2 per mole of H_2O), can reach a value of

$$\frac{(1 \cdot 16) + (4 \cdot 8)}{136} \simeq 35 \% . \quad (2.1)$$

This value is much higher if compared with that of the liquid phase in thermodynamic conditions close to clathrate synthesis ($P \simeq 200$ MPa at $T \simeq 273$ K), that is approximately 2 %.

The synthesis of the clathrate can be performed either from the liquid or solid phase [60]. As usually happens in solidification processes from the liquid phase, the transition from a liquid solution of hydrogen in water requires a moderate subcooling before obtaining the clathrate phase. This phenomenon is described by the well known nucleation theory [38, 65], and the growth kinetics is limited by the slow H_2 molecule diffusion in the liquid water [59, 66]. On the contrary, the transition from ice *Ih* to clathrate is more rapid [59, 63, 67] due to the more rapid diffusion of H_2 molecule in ground ice.

In the past the experimental study on this compounds has been performed by means of different spectroscopic techniques, both in situ and ex situ. Among these Raman spectroscopy turned out to be an effective and versatile tool for studying clathrates, not only from a dynamical point of view, but also for some structural aspects [63, 64, 66, 68]. In order to illustrate an example of low temperature Raman spectrum of hydrogen clathrate and what information can be deduced from it, in the upper panel of Figure 2.4 the vibrational band of HD clathrate synthesized at 1700 bar is reported [64]. Since for HD the ortho-para distinction does not apply, the low temperature HD clathrate spectrum has fewer spectroscopic features than the H_2 one, a characteristic which simplifies the interpretation of the data. The vibrational band shows at least four components, partially superimposed, which are attributed to intramolecular vibrations in different cages. The first peak, at about 3600 cm^{-1} , is due to a single molecule in the 5^{12} small cages, conclusion which is confirmed indirectly

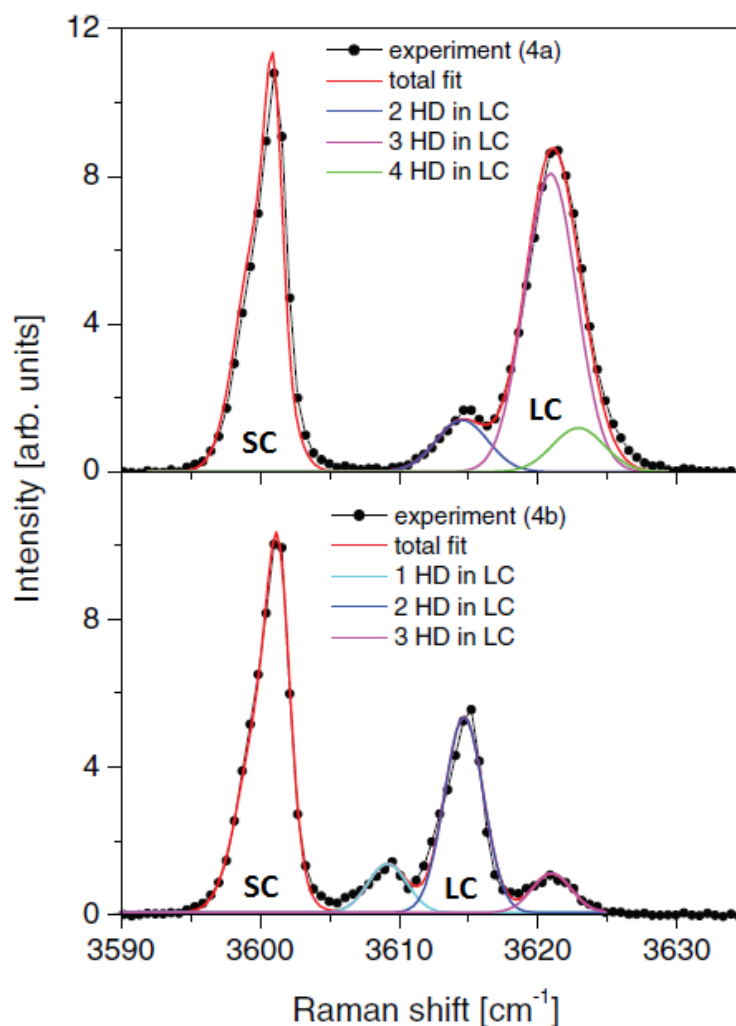


Figure 2.4: *Ex situ* low temperature Raman measurements of vibrational band of HD simple clathrate, taken from Ref. [64]. In the upper panel it is reported the spectrum of sample as synthesized at 1700 bar (experiment 4a), in the lower panel it is reported the spectrum of the sample after an annealing cycle (experiment 4b). In these experiments the use of HD as guest molecule significantly simplify the spectrum, since this molecule does not have ortho and para distinct components.

from measurements in the binary system HD + THF, where the HD molecule occupies only the small cages and its spectrum consists only of a single peak

at the same frequency. The other peaks are present only in the spectra of simple clathrate and are due to one or more molecules trapped in the $5^{12}6^4$ large cages. Each molecule inside a large cage with multiple occupancy vibrates on average at the same frequency of the other molecule contained in the same cage. Thus from the relative intensity and frequency of different peaks it is possible to deduce the H_2 -occupation of the large cages. In this way it has been demonstrated that the synthesis pressure of clathrates determines the degree of occupation of the large cages. Moreover, by submitting the clathrate to heating and cooling cycles, the average large cage occupation tends to decline, as shown in the lower panel of Figure 2.4. This could correspond to a migration of the molecules from the large cages with the highest occupancy to those with lower occupancy. Increasing temperature, the repulsion between the guest molecules tends to overcome the potential barrier formed by the LC hexagonal faces, each of which, in sII structure, is shared by two adjacent cavities. This allows the migration of the guest molecule in other cages and also the release from the solid sample. In addition to what exposed above, it is interesting to note that the spectrum of the gas trapped in the clathrate is shifted to lower frequencies compared to the same spectrum of free gas. For example in the case of the measurements carried out by Strobel et al. [63], the frequency of the $Q_1(0)$ and $Q_1(1)$ lines of the hydrogen molecules in the small cages of the clathrate are moved to -34 cm^{-1} compared to the frequency of the same lines measured in the gas. Additionally, by increasing the cage occupation, the lines move towards higher frequencies (Figure 2.4). The shift of the clathrate spectrum towards lower frequencies respect to the free gas, and the trends for the vibrational frequencies of guest molecules inside cages with different occupation suggest that in presence of a scarcely occupied cavity the attractive contribution of the guest-host interaction potential is dominant. As cage occupation number increase, each guest molecule has a lower free vol-

ume, thus the contribution of the repulsive interaction potential between guest molecules themselves and between the guest molecules and the water molecules starts to increase, inducing the higher frequency shift experimentally observed.

2.2.2 Hydrogen filled ices

In the high pressure region, i.e. above 0.35 GPa, the stable phases of the binary system $\text{H}_2\text{-H}_2\text{O}$ exhibit structures of the so called filled-ice type. In these compounds the hydrogen molecules are trapped in the voids of the water molecules skeleton. These compounds were studied by Vos et al. since 1993 by means of both Raman spectroscopy and X-ray diffraction in diamond-anvil cell, which allows to reach some tens of GPa [2].

Between 0.7 and 3.1 GPa the $\text{H}_2\text{-H}_2\text{O}$ mixture crystallizes in the so called C_1 filled ice structure, characterized by a hexagonal unit cell and $R\bar{3}$ space group. This structure, drawn in Figure 2.5, is proton-ordered and strictly resembles that of ice II and of He hydrate [51], where the water molecules are arranged in a channel-like configuration that can host the guest H_2 molecules. Moreover, this structure is distinct from that of the pure water in the same thermodynamic conditions, i.e. ice VI. Considering a single unit cell, 6 hydrogen molecules are contained every 36 water molecules, thus the maximum hydrogen content (1/6 hydrogen molar ratio) is lower than sII clathrate one.

In the region of higher pressure, i.e. between 2.3 and 30 GPa, another solid phase of this system is stable and is called C_2 , while between 2.3 and 3.1 GPa there is a coexistence region for the C_1 and C_2 phases. In the C_2 -phase the crystalline structure of the water molecules has the same symmetry of cubic ice Ic, that is space group $Fd\bar{3}m$, but with a larger unit cell volume due to the presence of hydrogen molecules that fill the voids of water lattice. The overall structure can be viewed as two interpenetrating fcc sublattices as shown in Figure 2.6. One sublattice is constituted by proton-disordered water

molecules and the other by randomly oriented hydrogen molecules, with an ideal stoichiometry $\text{H}_2\text{-H}_2\text{O}$ of 1:1, since there are 8 hydrogen molecules and 8 water molecules per unit cell. This structure recalls that of pure ice VII where, however, there are two H_2O not-linked Ic sublattices.

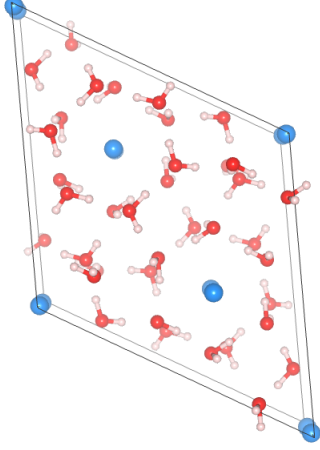


Figure 2.5: *Prospective drawing of the structure of filled ice in the C_1 -phase.*

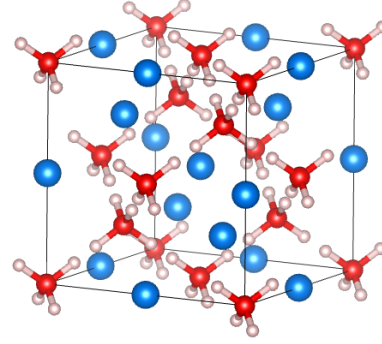


Figure 2.6: *Prospective drawing of the structure of filled ice in the C_2 -phase.*

2.2.3 The stable C_0 -phase

Recently two experimental studies [3, 4] were carried out at low temperature (100-270 K) and have demonstrated the presence of a further stable phase, named C_0 , in the region 360-700 MPa, that is intermediate between the stability region of the sII clathrate and the C_1 -phase (Figure 2.3). Before our work, the crystal structure of the C_0 -phase was under debate in the scientific community. The first structural model, later named C_0 -I, was proposed by Efimchenko et al. [3] after ex situ X-rays diffraction measurements on a recovered sample at room pressure and 80 K. The space group assumed is the $P3_112$, with oxygen atoms fully occupying $3a_1$ and $3b$ sites, and half occupying $3a_2$

sites. Even if the $3a_1$ and $3b$ oxygens already form a network of tetrahedrally coordinated water molecules, their position would prevent physically correct hydrogen bonds with the other molecules of the lattice. Subsequently Strobel et al. [4] suggest two possible structures, indicated by sT' , with space group $P4_2/mnm$ and oxygen atoms in $4d$ and $8j$ sites, that can give rise to a tetrahedrally bonded structure, and α -quartz, with space group $P3_221$ and oxygen atoms in $3a$ and $6c$ sites. However, this last model does not have a realistic oxygen bonding network and it has not been considered any more. Smirnov et al. [5] have examined theoretically these proposed models and have suggested sT' and C_0 -II, that is a variant of the C_0 -I with $3a_2$ sites not occupied, as viable candidates. At present only X-rays diffraction measurements have been performed and their analysis allows only to discriminate between different structural models, without being able of indexing unambiguously the diffraction profiles. Hence for a correct determination of the C_0 -structure, including the determination of the hydrogen atoms position, it is necessary to measure neutron diffraction patterns and, if possible, refine it by Rietveld analysis.

2.3 The thermodynamic stability of emptied structure

The role of guest molecules in the stability of hydrate crystals has been subject to various investigations since their discovery [38]. Generally, the hydrate compounds are not stoichiometric, since some cages may be empty, without affecting the stability of the crystalline structure. In the case of sI and sII structures, a complete cage filling is difficult to achieve. Experimentally [64, 69] it has been observed that the structure of sI and sII clathrate is stable even with partial filling of small cages by guest molecules. A recent experimental study on hydrogen clathrate [66], performed during the growth of the clathrate from

liquid phase, demonstrates the subsequent presence of small and large empty cages. On the contrary, in the case of the sH structure both types of cavities must be occupied in order to provide stability to the solid compound [38]. However, until recently it has been believed that the presence, albeit partial, of guest molecules in the cages is essential for the stability of the crystal, because the water skeleton would collapse without them.

One experimental study has recently demonstrated that at least one of these clathrate structures exists in its metastable state, if preserved at low temperature, even in absence of guest molecules [7]. In this experiment a neon sII clathrate-hydrate is kept under vacuum at constant temperature of 142 K for 5 days and neutron diffraction measurements finally have shown the complete evacuation of the host clathrate structure. In this way a new form of ice has been obtained, namely ice XVI, whose mechanical stability is verified up to 145 K. The study of the metastability of filled ice compounds in absence of guest has never been addressed and this is one of the purpose of our work.

Part II

Experimental methods



Chapter 3

Synthesis of the sample in the C_0 -phase

3.1 High pressure apparatus

The synthesis of the samples in the C_0 -phase is a challenging technical target. A good amount of ice and hydrogen gas should be maintained at high pressure (above about 4 kbar) and low temperature (about 253 K), i.e. within the thermodynamic stability region of the C_0 -phase for a certain amount of time. For this purpose we used a copper-beryllium autoclave, designed and manufactured at the ISC-CNR laboratories (Figure 3.1). The Cu-Be alloy is characterized by high hardness and yield strength, and high thermal conductivity. In addition, it is not susceptible to the so called “hydrogen embrittlement” [70], that is the adsorption and subsequent diffusion of hydrogen, which reduces the ductility of many metals and their fracture stress. The high pressure seal between the upper plug and the autoclave body is obtained by the use of a “Bridgman seal” [71]. This method is based on the use of a soft gasket material, usually copper, that undergoes a pressure that increases with the internal gas pressure. It is well known that this methodology is reliable up to very high pressure. The

autoclave has an internal available volume of about 22 cm^3 , which allows us to prepare an amount of sample sufficient to several different analysis. The



Figure 3.1: *Cu-Be autoclave used for the synthesis of the sample in the C_0 -phase.*



Figure 3.2: *The Nova Swiss membrane compressor suitable for hydrogen gas pressurization.*

modest cooling needed for the synthesis is obtained by placing the autoclave in a temperature controlled bath (water and ethylene glycol at about 50 %vol) circulating in an external chiller. A gas bottle with 99.995% pure hydrogen is connected to the input valve of a membrane compressor (Nova Swiss, Figure 3.2). The autoclave is connected by a valve to the output of the compressor. In the portion of circuit between the autoclave and the compressor there is a high pressure transducer (HBM P2VA2/7000 bar) with a declared accuracy of $\pm 0.3 \%$ of the nominal full scale reading in the entire working range (0.2 - 7.0 kbar). An overall picture of the mounted high pressure apparatus is reported in Figure 3.3.



Figure 3.3: *The entire high pressure apparatus as appears during the sample pressurization. The autoclave is placed in refrigerant liquid bath contained in polystyrene box (yellow circle).*

3.2 Sample synthesis and recovering

Several instances of solid H_2 - H_2O compound are produced using a standardized procedure. A few grams of ice powder are introduced in the autoclave, previously cooled below 273 K. All this operations are carried out in dry nitrogen atmosphere, realized inflating a plastic bag with a continuous flow of nitrogen gas. Once the autoclave is closed and connected to the high pressure circuit, it is placed into the thermostatic bath and maintained cold ($\simeq 255$ K) for few hours in order to obtain a completely thermalization of the sample. Af-

ter this procedure, the ice sample is exposed isothermally to hydrogen gas at a pressure in the range or above 4.3 kbar. Prudentially, the sample is left under pressure for a few days, even though, while rising pressure during synthesis, an abrupt decrease of the rate of pressure rise has been observed at about 3.6 kbar, which is a clear indication of a large hydrogen adsorption by the ice and the start of phase transition.

After the synthesis, in order to recover the sample at ambient pressure, the autoclave is quenched in a liquid nitrogen bath and, after the release of pressure, it is opened. Then the sample is recovered in the form of a fine powder. The transfer process, either for ex-situ measurements or for dewar storing, is a delicate process and has to be accomplished in a liquid nitrogen bath and dry-nitrogen atmosphere in order to avoid unintentional heating and humidity condensation, that would compromise the sample quality. In any case, to check the quality of each sample batch, a small amount of powder is submitted to a rapid offline check with Raman spectroscopy at liquid nitrogen temperature, thus verifying the absence of ice Ih or other spurious phases.

The same synthesis procedure is applied for the samples that have been investigated by X-rays diffraction at CRIST facility (University of Florence, Italy), except that in this case a drop of water is frozen from the beginning inside few common x-rays glass capillaries, 10-15 mm long. The frozen water occupies a capillary length of about 1 mm. The capillaries are inserted in the autoclave, where they undergo the same standardized procedure, and are then recovered and handled at liquid nitrogen temperature.

Chapter 4

Raman spectroscopy

One of the experimental techniques used in this thesis to study the vibrational dynamics of hydrates is based on the phenomenon of the Raman effect in light-scattering. Raman spectroscopy is widely used in chemical-physics for studying the vibrational dynamics of molecular compounds in the different states of aggregation of the matter. Moreover, it represents a very useful tool for investigating the interaction of a physical system with its environment, which may give a characteristic signature in Raman spectrum. Basic principles are treated in several books (e.g. [72]). Here we recall briefly the basis of the Raman effect theory and give some examples about its use in the field of physics of matter.

4.1 The Raman effect

When a monochromatic radiation of frequency ω_0 , typically in the visible region, hits on a material system, part of the radiation is scattered in different directions respect to the direction of propagation of the incident light. The spectrum of the scattered light, besides containing the component at frequency ω_0 , whose intensity is generally dominant, includes a series of weaker compo-

nents (“Raman”) at frequencies $\omega \neq \omega_0$. The energies E , corresponding to the frequencies ω , i.e.

$$E = \hbar \Delta\omega = \hbar |\omega_0 - \omega|, \quad (4.1)$$

where \hbar is the reduced Planck constant, are characteristic of the transitions between energy levels of the material. Raman radiation originates from the oscillation of electric dipoles induced by an external field of excitation. Considering a molecule that can vibrate without performing any rotation or translation and applying the quantum theory of time-dependent perturbations, it is possible to obtain a formula for the intensity of the scattered Raman radiation [72]. The molecular system in the vibrational state i is perturbed by the electromagnetic radiation. The electric field of the electromagnetic wave (treated classically) can be expressed by

$$\mathbf{E} = \mathbf{E}_0 e^{-i\omega_0 t} + \mathbf{E}_0^* e^{i\omega_0 t}. \quad (4.2)$$

Moreover, it is assumed that the energy of the incident radiation is much smaller than that of any electronic transition of the sample. Using the first-order perturbation theory and taking into account only the electric dipole term, the first-order induced transition electric dipole is given by

$$\mathbf{P}_{fi}^{(1)} = (\alpha)_{fi} \mathbf{E}_0 e^{-i(\omega_0 - \omega_{fi})t} + (\alpha)_{fi}^* \mathbf{E}_0^* e^{i(\omega_0 - \omega_{fi})t}, \quad (4.3)$$

where

$$(\alpha_{xy})_{fi} = \frac{1}{\hbar} \sum_{r \neq i, f} \left(\frac{(p_y)_{fr} (p_x)_{ri}}{\omega_{rf} + \omega_0} + \frac{(p_x)_{fr} (p_y)_{ri}}{\omega_{ri} - \omega_0} \right) \quad (4.4)$$

is the matrix element of the generic component (xy) of the polarizability tensor between the initial vibrational state i and the final f , $\omega_{fi} = \omega_f - \omega_i$ and \mathbf{p} is the electric dipole moment operator. If ω_{fi} assumes a value higher, equal or lower than 0, the moment (4.3) describes Raman Stokes, Rayleigh or Raman

anti-Stokes scattering at frequencies $\omega_0 - |\omega_{fi}|$, ω_0 and $\omega_0 + |\omega_{fi}|$ respectively. Taking into account also the Boltzmann factor for the different populations of the initial and final state, the Raman power for unit solid angle follows a law as

$$I_S \propto \frac{(\omega_0 - \omega_{fi})^4}{1 - e^{-\frac{\hbar \omega_{fi}}{k_B T}}} \quad (4.5)$$

$$I_{AS} \propto \frac{(\omega_0 + \omega_{fi})^4}{e^{\frac{\hbar \omega_{fi}}{k_B T}} - 1}, \quad (4.6)$$

where k_B is the Boltzmann constant.

The polarizability is determined by the wave functions and the energy levels of the system, hence the properties of the scattering molecules affect the characteristic of the scattered radiation. In particular, the symmetry properties of the molecule, and of each roto-vibrational state, play an important role in determining the Raman activity or inactivity of each transition. For a general transition, from the state i to the state f , to be Raman active at least one component of the transition polarizability tensor (see Eq. 4.4)

$$(\alpha_{\rho\sigma})_{fi} = \langle f | \alpha_{\rho\sigma} | i \rangle, \quad \text{with } \rho, \sigma = x, y, z, \quad (4.7)$$

must be non-zero. Thus, as the general rule for this transition to be Raman active is that the representation carried by the matrix element of the polarizability tensor, that is the direct product of the representations carried by the molecular states and by one of the components of α , contains the totally symmetric representation. This general conditions can be obtained in the framework of group theory and of the theory of point group representation [73].

In the two followings sections we present the Raman effect measured both on almost isolated molecules (e.g. in the gas state) and on solids (e.g. regular crystal).

4.1.1 Vibrational Raman spectroscopy on molecules

Since we are interested in studying the dynamics of the nanoconfined hydrogen molecule, it could be useful for the following discussion to recall some examples in which this dynamics has been efficiently studied with Raman spectroscopy.

In the case of molecules, the polarizability α is the physical quantity which embeds the dynamics of the system. In a classical picture, it depends on the instantaneous positions of the atomic nuclei, which change in time as a consequence of both molecular rotation and vibration. A molecule with n nuclei possesses $3n - 3$ roto-vibrational degrees of freedom. In a first approximation, vibration and rotation are considered decoupled, thus allowing one to model independently the rotation of a rigid molecule, and the vibration of the molecule in the center-of-mass reference frame. The description of the vibrational dynamics passes through the definition of the normal modes, which rigorously applies to harmonic motion. To each normal coordinate, one associates one normal frequency. Each normal mode behaves as a quantum harmonic oscillator, having energy levels equal to $E_v = \hbar(v + 1/2)$. In the following the molecular transitions that we will consider are only those of a homonuclear diatomic molecule, as H_2 or D_2 . Therefore we will not describe further the theory of vibrational Raman scattering for polyatomic molecules.

For an isolated diatomic molecule, the roto-vibrational energy levels are calculated considering several correction to the model of a rigid rotor and harmonic oscillator. In the case of H_2 and D_2 , the molecular levels, commonly labelled with $E_{\nu,J}$, where ν and J are the quantum numbers of the vibrational and rotational state of the molecule, are known with extremely high precision. A fairly accurate expression was proposed by Herzberg [74]:

$$\begin{aligned}
 E_{\nu,J} = & \hbar\omega_e \left(\nu + \frac{1}{2} \right) - \hbar\omega_e x_e \left(\nu + \frac{1}{2} \right)^2 + \dots \\
 & + B_\nu J(J+1) - D_\nu J^2(J+1)^2 + \dots
 \end{aligned} \tag{4.8}$$

with $x_e \ll 1$, where

$$B_\nu = B_e - \alpha_e \left(\nu + \frac{1}{2} \right) + \dots \text{ with } B_e \gg \alpha_e \quad (4.9)$$

is the rotational constant related to the vibrational state with quantum number ν ,

$$D_\nu = D_e + \beta_e \left(\nu + \frac{1}{2} \right) + \dots \text{ with } D_e \gg \beta_e \quad (4.10)$$

is the correction to the rotational constant related to centrifugal effect, ω_e is the harmonic oscillation frequency, and α_e , β_e , and x_e are constants. For a rigid diatomic molecule B_e is directly related to the moment of inertia I

$$B_e = \frac{h}{8\pi^2 c I} = \frac{h}{8\pi^2 \mu r_e^2}, \quad (4.11)$$

where B_e is expressed in wavenumbers, with h and c that are the Plank constant and the velocity of the light, r_e is the distance of the nuclei and μ their reduced mass. The roto-vibrational energy levels are degenerate respect to the quantum number M related to the projection of the rotational angular momentum J_z on the z -axis of the laboratory fixed frame. In the following the transitions between different roto-vibrational states (ν, J) and (ν', J') are indicated by using the common spectroscopic notation (e.g. $S_0(1)$, $Q_1(0), \dots$), according to which the capital letter indicates the change in the rotational quantum number J , e.g. O, P, Q, R and S for $\Delta J = -2, -1, 0, 1$ and 2 , respectively, the subscript digit indicates the final vibrational quantum number and the digit in parenthesis is the initial rotational quantum number.

Let's consider the free hydrogen molecule in the gaseous state and in other environments. Due to the lightness of this molecule, and consequently, to the large value of its rotational constants, its rotational lines in pure rotational spectrum sit at relatively high frequency and are well separated from each other (e.g. about 350 cm^{-1} and 580 cm^{-1} in the case of $S_0(0)$ and $S_0(1)$ lines, respectively). For a similar reason, the rotational structure of the fundamental

vibrational band $Q_1(J)$ is observable as a set of lines separated by a quantity of the order of several cm^{-1} . The spectrum of this band is easily measurable

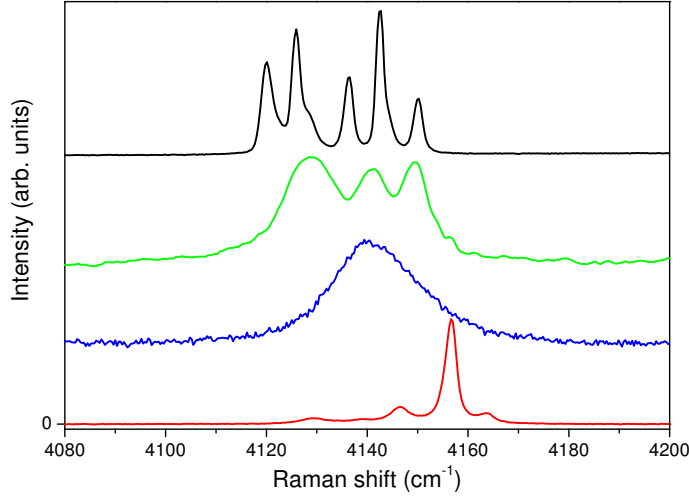


Figure 4.1: *Raman spectra of H_2 vibrational band for hydrogen gas (red line), hydrogen dissolved in liquid water solution (blue line) and hydrogen clathrate-hydrate (green line). These spectra are acquired in similar thermodynamic conditions (about 2 kbar pressure and few degree below 0°C). The spectrum of clathrate measured at 11 K and room pressure is reported with the black line.*

with a standard Raman apparatus (see next section) and is reported with the red line in Figure 4.1 for the H_2 molecule in the high pressure gas. In this spectrum it is possible to recognize at least four peaks corresponding to different molecular vibrational transitions $(\nu = 0, J) \rightarrow (\nu = 1, J)$, namely $Q_1(0)$ at 4164 cm^{-1} , $Q_1(1)$ at 4158 cm^{-1} , $Q_1(2)$ at 4147 cm^{-1} and $Q_1(3)$ at 4119 cm^{-1} , each having intensity proportional to the population of the corresponding rotational energy level involved. The overall band-shape in this spectrum is typical of the gas at those particular values of pressure and temperature. Anyway, this shape changes significantly if the hydrogen molecules are dissolved in liquid water [57], shown by the spectrum drawn as a blue line in Figure 4.1, demonstrating the strong interaction between hydrogen and water molecules.

In this case the band is shifted towards lower frequency and the components, belonging to different rotational levels, are superimposed, resulting in a single smooth and almost symmetric profile, that could be explained taking into account a collisional mechanism between H_2 and H_2O molecules [75]. If the hydrogen molecule is trapped in a solid host framework like a clathrate-hydrate [66], its interaction with the water cages gives rise to a Raman spectrum with a different shape. At cryogenic temperature (black line of Figure 4.1) several distinct components are observed, which have been interpreted as rising from molecules either hosted in the small cages or in the large cages, with occupation from one molecule per cage to four molecules per cage. Furthermore, from the peak intensity it is easy to deduce also the number of filled cages that are present in a given sample [64]. The spectrum of a hydrogen clathrate at a temperature a few degree below zero, reported with the green line in Figure 4.1, is characterized by three quite wide peaks. At this temperature the $Q_1(J)$ rotational components are not well resolved as it happens at cryogenic temperature and each peak is due to the vibrational motion of hydrogen guest molecule in different cage types, where the higher frequency peaks correspond to a cavity with lower free volume. These spectra are reported here to show, with examples, how the environment influences the vibrational spectrum of the H_2 molecule.

4.1.2 Vibrational Raman spectroscopy on crystals

In solid state physics Raman spectroscopy is used extensively to characterize lattice vibrations. Lattice vibrations are treated, in first approximation, as being harmonic. This leads to the description of the dynamics of the lattice in terms of the normal modes, as in the case of isolated molecules. The important difference is that, in the crystal, the harmonic excitation is described by one more parameter besides the oscillation frequency, that is the phonon wavevec-

tor \mathbf{q} . In a light scattering process, where the incident light is monochromatic with frequency ω_l and wavevector \mathbf{k}_l , the total momentum should be conserved, that is $\mathbf{q} = \mathbf{k}_l - \mathbf{k}_s$, where \mathbf{k}_s is the wavevector of the Stokes scattered radiation. In general, the light wavevector \mathbf{k}_l is much smaller than the typical phonon wavevectors. The maximum wavevector in the first Brillouin zone \mathbf{q}_M is of order π/d , where d is the lattice constant, and is typically three orders of magnitude larger than both \mathbf{k}_l and \mathbf{k}_s . Therefore, visible radiation couples with phonons having $\mathbf{q} \simeq \mathbf{0}$. This has an important consequence for what concerns the symmetry properties of the scattering cross section. The spatial symmetry of the crystal is formally described by its symmetry group, that is the group of all spatial transformations that leave the crystal invariant. These comprise rotations, reflections and translations. The complete theory of group representation cannot be summarized here and is widely treated in literature [76, 77]. We want to remark, however, that for disordered crystals, i.e. crystals where the translational symmetry is not perfectly fulfilled, the Raman spectrum is influenced by the large spread of force constants, and is often characterized by broad bands in place of narrow lines for ordered crystals.

Let's consider, for example, the optical phonons in ice, that give rise to a quite large Raman band, with a characteristic peak at about 230 cm^{-1} and a weaker one at 310 cm^{-1} . This example is discussed here because it will be useful for comparison with similar spectra measured in this work. A Raman spectrum of common ice Ih, measured at low temperature, is reported with black line in Figure 4.2. The overall shape of this band is the result of a superimposition of some Raman active modes [78], and can be used for identifying, from a dynamic point of view, the various ice structures, even the ordered ones. As explained in Chapter 1, in the common form of ice Ih the water protons are disordered. Anyway by the insertion of small quantities of chemically strong bases into ice structure, obtained freezing a slightly KOH-doped water solution (0.01 M), it

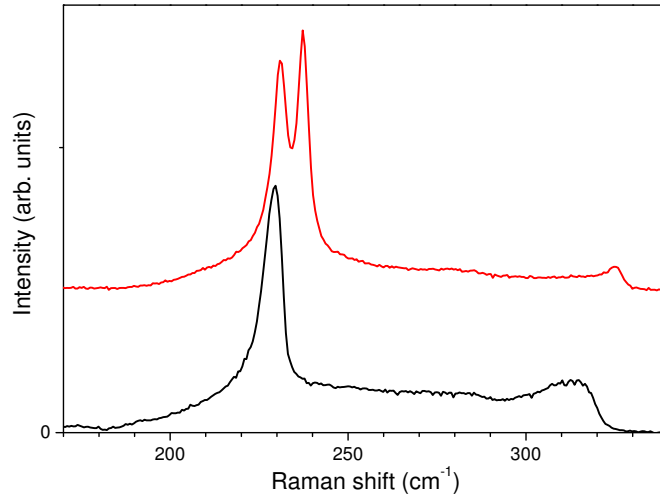


Figure 4.2: *Raman spectra of the lattice phonon band of H_2O ice Ih at 77 K (black line) and H_2O ice Ih, doped with KOH, in coexistence with its ordered form ice XI at 55 K (red line). The measurements are performed at room pressure.*

is possible to favour the kinetics of the ordering process, whose temperature of transition disorder-order is 72 K for H_2O ice Ih. In Figure 4.2 the spectrum of KOH-doped ice at temperature below the ordering transition is reported with red line. The appearance of two narrow peaks at 240 cm^{-1} and 330 cm^{-1} , is a strong signature of the proton-ordering of the water lattice, i.e. the transformation of a part of ice Ih into its corresponding ordered form ice XI [79, 80]. The comparison of the two spectra shown in Figure 4.2 demonstrate the potentiality of Raman spectroscopy, not only for a dynamical characterization of the solid system, but also as a signature to distinguish between different structural configurations.

4.2 Raman apparatus

Sample environment The Raman measurements presented in this work refer to several samples, previously synthesized according to the procedure described in Section 3.2. A small amount of sample powder (about 0.05 g) is safely transferred in a dry-nitrogen atmosphere from the vials stored in the dewar to the Raman optical cell, that is in thermal contact with the cold finger of a closed-cycle He cryostat (Leybold Coolpower 4.2GM). To avoid sample heating above liquid nitrogen temperature, the cryostat is turned on about one hour before the start of the transfer process. The aluminium optical cell (Figure 4.3), designed and manufactured at the ISC-CNR laboratories, is equipped with a 20 mm diameter optical window (Suprasil) and a stainless steel capillary, connected to a low pressure circuit for gas insertion or evacuation. The pressure seal between the window and the cell body is provided by an indium gasket. A temperature sensor (silicon diode) and a ceramic heater are in thermal contact with the cryostat cold finger for temperature control. By means of this apparatus the temperature of the sample cell can be set to any temperature between room temperature and 10 K and the gas pressure in the cell can be varied between few mbar and about 50 bar. It is possible to obtain also dynamic vacuum conditions, since the cell can be connected to vacuum pump.

The gas circuit is designed for providing volumetric measurements of the gas inserted into the cell or released by sample during heating. The circuit, shown in Figure 4.4, is connected to a hydrogen bottle, a gauge volume (180.3 cm³) equipped with two low pressure transducer (10 mbar and 100 mbar full scale, respectively), two intermediate pressure transmitter with 10 bar and 350 bar as full scale values respectively, both having an accuracy of 0.1% full scale value, and a turbomolecular vacuum pump.

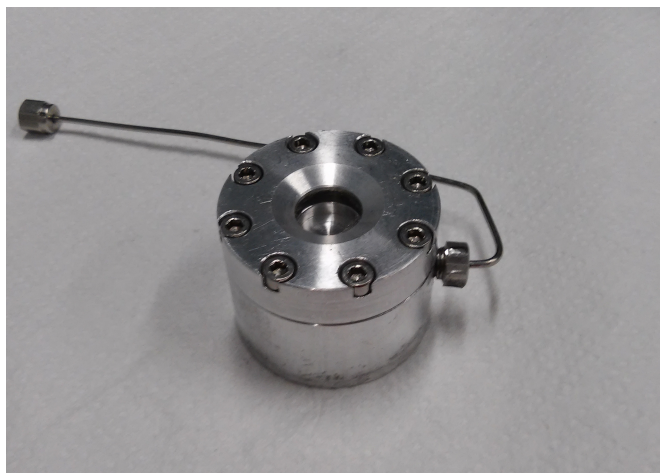


Figure 4.3: *The Raman optical cell.*

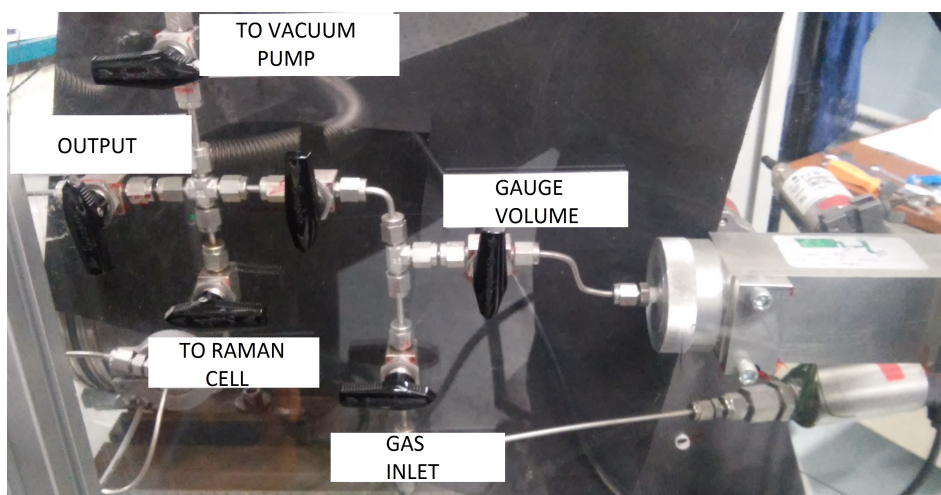


Figure 4.4: *The low pressure circuit used for volumetric measurements.*

The optical path The light source for the excitation of the Raman spectra is an Ar ion laser (Coherent Innova I 304-A), which emits at 514.5 nm a maximum power of 1.7 W. The laser is equipped with a “power-tracking” system, which maintains constant the output power, by optimizing the alignment of the optical cavity during operation. The laser beam is focused on the sample cell by means of one converging lens with a focal length of 125 mm. The

power of the laser beam on the sample is about 30 mW. The scattered light is collected in a quasi-backscattering geometry by a 40 mm converging lens and re-focused on the entrance slit of a spectrometer by a 70 mm converging lens. A “Super Notch” spectral filter is inserted between these two lenses to remove scattered radiation at the laser frequency, that would compromise the spectra, specially in the spectral region close to the laser frequency. Being the effective diameter of the collimated beam equal to 10 mm, the numerical aperture of the collection optics is $f/\# \simeq 7.0$, similar to the one of the monochromator ($f/\# \simeq 7.8$), and magnification of the image on the entrance slit is $M = 1.75$. The spectrometer is a first stage of a Czerny-Turner double monochromator (Spex 1401), having a focal length 850 mm, equipped with a holographic grating with 1800 grooves/mm. The grating movement, carried out with a stepping motor, is controlled by means of an external digital computer. The original exit slit of the first stage of the spectrometer has been replaced by a flange on which a Charge Coupled Device (CCD) detector is fixed (Andor C DU401A-BV), on the focal plane of the spectrometer exit mirror. The CCD has 1024 x 128 pixels, each one with linear dimensions 26x26 μm . In order to minimize the thermal noise, the CCD is cooled with a Peltier cell down to 200 K. The spectral resolution of the spectroscopy apparatus is 0.4 cm^{-1} . This has been measured considering the Full Width at Half Maximum (FWHM) of the 632.8 nm red line of a He-Ne laser, using 20 μm spectrometer entrance slit.

The choice of mounting the CCD detector in place of the exit slit of the first stage of the double monochromator, instead of using both stages, is a good compromise between efficiency and resolution. Moreover, in this case the spectral collection window is wider, thus allowing the acquisition in the same spectral window of the different bands of interest and avoiding subsequent spectral collections, that would require an intensity calibration. Stray-light may constitute a problem when a single-stage monochromator is used, but

this is almost completely eliminated by the Super Notch filter.

4.2.1 Calibration of the spectrometer

The scattered radiation, dispersed in frequency by the monochromator, is revealed by the CCD, which converts it into a digital signal saved on the computer connected to the detector. The recorded spectrum is expressed in number of counts for each of the 1024 CCD columns (channels). Therefore, in order to convert the acquired information in physical units, two calibrations are necessary:

- X-axis calibration, assigning to each CCD channel the corresponding wavelength. This has to be done for each spectral window, since spectral range depends from the grating position of the monochromator.
- Y-axis relative calibration, in order to obtain for each channel an intensity value proportional to the spectral intensity of the originally scattered light by the sample, hence taking into account the optical system efficiency and dark noise.

Wavelength calibration The spectrum used for wavelength calibration of the apparatus is emitted by a neon spectral calibration lamp placed in front of the monochromator entrance slit. The emission spectrum of neon, excited by an electric discharge, is formed by lines whose position is known with good accuracy [81]. Through a dedicated software, the proper wavelength can be assigned to the channel where the peak of the corresponding spectral line is located. Once a sufficient number of channels has been calibrated, typically not less than 4, the software uses a quadratic or cubic interpolation law to calibrate the entire x-axis. As an example, in Figure 4.5 we report one of the spectra used for this type of calibration. This procedure is performed each time the monochromator grating is moved, in order to avoid introduction of systematic

errors on wavelength values due to not perfect mechanical movement of the monochromator grating. The Raman spectrum is usually expressed as func-

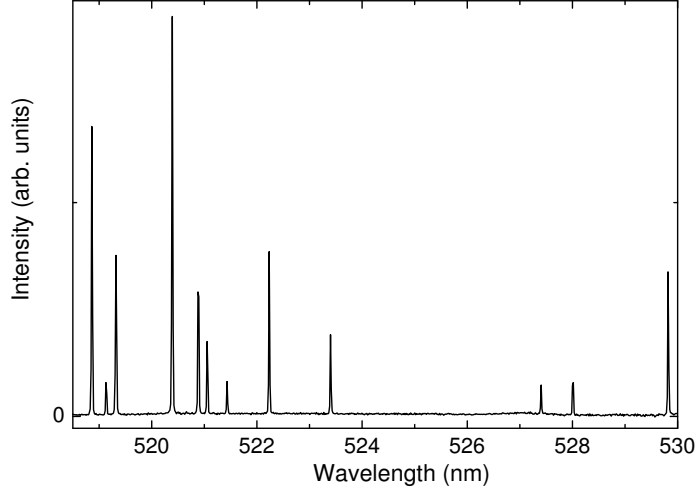


Figure 4.5: *Spectrum of neon calibration lamp in the spectral window centred at 524.77 nm.*

tion of the frequency shift from the excitation laser frequency (Raman shift), often using wavenumbers $\tilde{\nu} = \frac{1}{\lambda}$ instead of the frequency $\nu = \frac{c}{\lambda}$, where λ is the wavelength of the radiation in vacuum. Knowing the wavelength in air of the laser radiation ($\lambda_L = 514.53083$ nm [82]) and the wavelength in air corresponding to a given CCD channel (λ_a), the Raman shift, usually expressed in cm^{-1} , is given by

$$\Delta\tilde{\nu} = \tilde{\nu}_L - \tilde{\nu} = \left(\frac{1}{\lambda_L n(\lambda_L)} - \frac{1}{\lambda_a n(\lambda_a)} \right) , \quad (4.12)$$

where $\tilde{\nu}_L$ is the wavenumber of laser radiation, $\tilde{\nu}$ is the wavenumber corresponding to the channel illuminated by the radiation with wavelength in air λ_a and $n(\lambda_{L,a})$ is air refractive index at the wavelength in air $\lambda_{L,a}$. Difference of the index of refraction of air and vacuum may influence the correct calibration of the frequency scale, e.g. as much as 4 cm^{-1} in the region of the H_2 vibrational lines (4160 cm^{-1}), while the wavelength dependence of refractive

index n has little effect. The main source of error in this calibration procedure is related to the evaluation of the peaks of the spectral lines. It is estimated to be one pixel, that is 0.5 cm^{-1} .

Relative intensity calibration The control software of the CCD detector produces a file containing an intensity value for each channel. Each recorded spectrum is the sum of two subsequent acquisition of the same duration, typically of 120 s to obtain a satisfactory signal to noise ratio. In this way the software is able to remove any spurious feature, typically intense spikes, due to cosmic ray hitting the detector during data acquisitions.

For the spectra measured in the region $150\text{-}650 \text{ cm}^{-1}$, for which an accurate relative intensity analysis of the bands will be necessary, a data reduction process is applied all at once with a Fortran routine. Firstly, the raw spectrum is corrected for dark counts (measured switching off the laser excitation source) and for efficiency of the spectrometer (estimated with the spectrum of a white calibration lamp placed in the optical path of the scattered Raman radiation). Then a background is estimated by fitting the spectrum in some flat regions with a fourth-order polynomial curve, and it is subtracted (Figure 4.6). In other spectral regions, where a quantitative intensity analysis is not needed, only the background subtraction is performed.

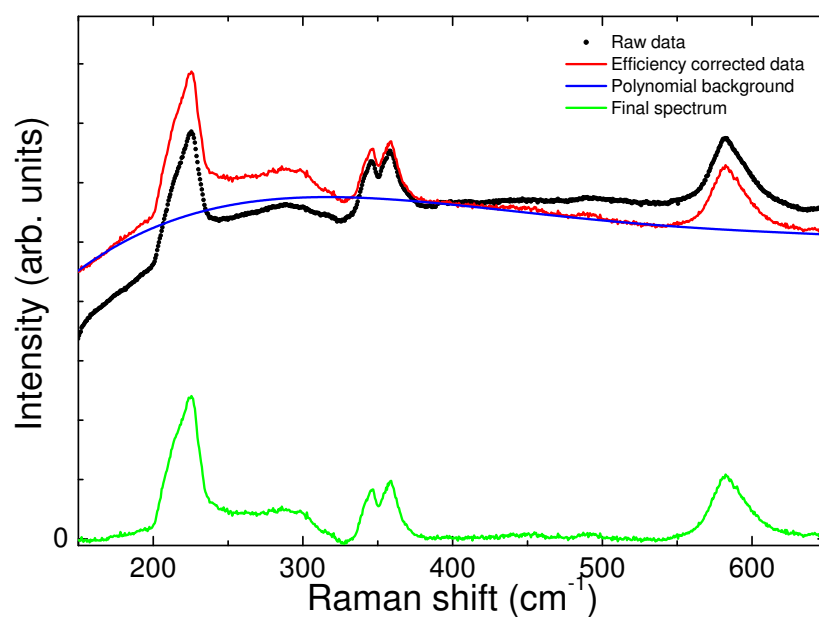


Figure 4.6: *Example of typical steps during data analysis of hydrate spectrum acquired in the region 150-650 cm⁻¹. In this figure is reported the experimental data as collected with black points, the spectrum after efficiency correction with red line, the polynomial curve estimating the background with blue line and the final spectrum after background subtraction with green line.*

Chapter 5

Neutron scattering

The other experimental technique that we have to introduce is the neutron scattering. It represents an effective technique for understanding the properties of materials, mostly on an atomic scale [83]. Nowadays it is widely used in different research fields, from basic to applied science, due to its complementarity with other experimental probes, e.g. photons. The neutron interacts with the atomic nucleus, and it is sensitive even to light atoms, as opposed to X-rays, which probe electronic clouds. The scattering cross section can vary substantially by passing from one element to the next, and also for different isotopes of the same element, as for hydrogen and deuterium (Figure 5.1). This peculiarity, in conjunction with the use of the isotopic substitution, allows one to evidence selectively specific aspects of a material system. Thermal neutrons, i.e. neutron having energy $E \simeq k_B T$, where T is room temperature, have wavelength and energy that match spatial scale and excitation energy characteristic of the condensed matter, allowing the determination of both static structure and dynamical properties of the investigated material. Being a particle with a mass ($m = 1.675 \cdot 10^{-27}$ kg), the neutron is able to exchange a wide range of energy and momentum, thus covering a large portion of the kinematic plane (\mathbf{Q}, ω) , especially when compared to other experimen-

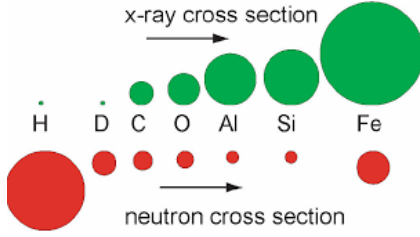


Figure 5.1: *Comparison between X-ray and neutron cross sections. The area of the circles is proportional to the scattering strength. The black arrows indicate increasing mass number.*

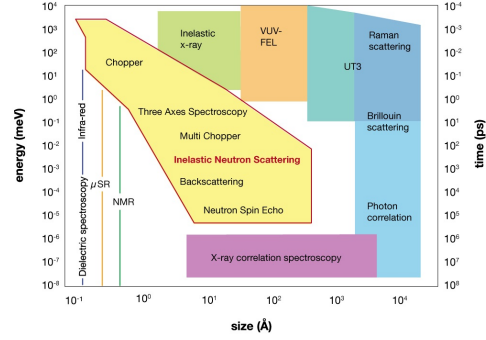


Figure 5.2: *Dynamic range for neutrons and some other probes used for studying the condensed matter.*

tal techniques (Figure 5.2). Another key property of the neutron is its zero charge. This fact leads to a large penetration depth and, consequently, the capacity of probing bulk properties of matter, without radiation damage on the investigated sample, which is a crucial point for studying living biological samples or cultural heritage. Furthermore, the neutron carries a magnetic moment, which opens the possibility to measure magnetic properties of matter. In addition, the interaction of neutrons with the material systems is weak, allowing the determination of the scattering law from experimental data within linear-response theory framework.

For the study of condensed matter only slow neutrons are considered, i.e. neutrons having kinetic energy

$$E = \frac{mv^2}{2} < 1 \text{ keV}, \quad (5.1)$$

where v is the neutron velocity. The wavelength λ of a neutron is defined by means of the usual de Broglie relation, and the modulus of the wavevector \mathbf{k} is

$$k = \frac{p}{\hbar} = \frac{2\pi}{\lambda}, \quad (5.2)$$

where p is the momentum of the neutron and \hbar is the reduced Plank constant. Combining these relations, energy can be expressed as

$$E = \frac{\hbar^2 k^2}{2m} = \frac{h^2}{2m\lambda^2}. \quad (5.3)$$

5.1 The scattering law

In a neutron scattering experiment the intensity of scattered neutrons is measured as a function of both the momentum transfer \mathbf{Q} , usually called scattering vector

$$\mathbf{Q} = \mathbf{k} - \mathbf{k}' \quad (5.4)$$

and energy transfer E

$$E = \hbar\omega = \frac{\hbar^2}{2m}(k^2 - k'^2), \quad (5.5)$$

where \mathbf{k} and \mathbf{k}' are the wavevectors of the incident and scattered neutron, respectively. These relations are derived directly from the conservation laws of momentum and energy in the scattering process, that is called elastic if $k = k'$, i.e. $\hbar\omega = 0$. However it is important to underline that in neutron scattering the conventional definition of “elastic” differs from the usual nomenclature of “elastic collision” in elementary physics. Indeed, in this sense all the neutron scattering events are elastic collisions.

The observed spectrum, i.e. the collected intensity of neutron scattered per energy unit by a monoatomic system, is given by

$$\frac{dI}{d\omega} = \Phi_0 N \frac{d^2\sigma}{d\Omega d\omega} \Delta\Omega \eta(\mathbf{k}') \quad (5.6)$$

where Φ_0 is the flux of incident neutrons, N is the number of scatterers, $\Delta\Omega$ is the solid angle in which the scattered neutrons are collected, and $\eta(\mathbf{k}')$ is the detection efficiency of neutrons with wavevector \mathbf{k}' . The term $\frac{d^2\sigma}{d\Omega d\omega}$ is the so called double differential scattering cross section and contains all the physical informations about the scattering system. This quantity corresponds to the number of neutrons scattered per time unit, unit solid angle and unit energy transfer, divided by the flux of the incident neutrons, by the number of scatterers and by the efficiency, and can be expressed using the Fermi's Golden Rule as follows:

$$\frac{d^2\sigma}{d\Omega d\omega} = \frac{1}{N} \left(\frac{m}{2\pi\hbar^2} \right)^2 \frac{k'}{k} \sum_{\lambda, \lambda', \sigma, \sigma'} p_\lambda p_{\sigma'} |\langle \mathbf{k}', \sigma', \lambda' | U | \mathbf{k}, \sigma, \lambda \rangle|^2 \delta \left(\omega + \frac{E_\lambda - E_{\lambda'}}{\hbar} \right), \quad (5.7)$$

where $|\lambda\rangle$ and $|\lambda'\rangle$ are the initial and final state of the scatterer with thermal population factor p_λ and energy $E_{\lambda, \lambda'}$, while σ and σ' are the spin state of incident and scattered neutron, respectively. The interaction potential U between the neutron and the sample nucleus at a fixed positions \mathbf{R}_j can be described by an effective potential, namely Fermi pseudopotential

$$U(\mathbf{r}) = \frac{2\pi\hbar^2}{m} \sum_j b_j \delta(\mathbf{r} - \mathbf{R}_j) \quad (5.8)$$

where the complex quantity b_j is named the scattering length of each nucleus and depends on both the isotope and the spin quantum number I of the nucleus. For the following discussion the imaginary part of b_j , that describes the energy-dependent absorption process, and the spin states $\sigma^{(i)}$ can be neglected. Making use of plane waves

$$|\mathbf{k}\rangle = e^{i\mathbf{k}\cdot\mathbf{r}} \quad (5.9)$$

to describe the state of the incident (and scattered) neutrons, it is easy to obtain the final formula for the cross-section for the scattering per atom from

an ensemble of nuclei, each one characterized by a scattering length b_j , that is

$$\frac{d^2\sigma}{d\Omega d\omega} = \frac{1}{N} \frac{k'}{k} \left(\frac{1}{2\pi} \right) \sum_{j,j'} b_j b_{j'} \int \langle e^{-i\mathbf{Q}\cdot\mathbf{R}_{j'}(0)} e^{i\mathbf{Q}\cdot\mathbf{R}_j(t)} \rangle e^{-i\omega t} dt. \quad (5.10)$$

This final formula can be rewritten in term of the dynamical structure factor $S(\mathbf{Q}, \omega)$, that is the space-time Fourier transformation of the van Hove space-time pair correlation function $G(\mathbf{r}, t)$

$$S(\mathbf{Q}, \omega) = \frac{1}{2\pi} \int \int G(\mathbf{r}, t) e^{i\mathbf{Q}\cdot\mathbf{r}} e^{-i\omega t} d\mathbf{r} dt. \quad (5.11)$$

By means of the theory of the correlation functions, the $G(\mathbf{r}, t)$ can be written as

$$G(\mathbf{r}, t) = \frac{1}{(2\pi)^3} \frac{1}{N} \int \sum_{j,j'} \langle e^{-i\mathbf{Q}\cdot\mathbf{R}_{j'}(0)} e^{i\mathbf{Q}\cdot\mathbf{R}_j(t)} \rangle e^{-i\mathbf{Q}\cdot\mathbf{r}} d\mathbf{Q}. \quad (5.12)$$

$G(\mathbf{r}, t)$ can be considered as the most general description of the structure and dynamics of condensed matter on an atomic scale, since it describes the correlation between the atom j' at the time $t = 0$ at the position \mathbf{r}' and the atom j at a later time t at the position $\mathbf{r}' + \mathbf{r}$. Applying the property of the δ -function it is possible to rewrite $G(\mathbf{r}, t)$ as

$$G(\mathbf{r}, t) = \frac{1}{N} \sum_{j,j'} \int \langle \delta(\mathbf{r}' - \mathbf{R}_{j'}(0)) \delta(\mathbf{r}' + \mathbf{r} - \mathbf{R}_j(t)) \rangle d\mathbf{r}'. \quad (5.13)$$

Separating the terms with $j = j'$ and $j \neq j'$, it is convenient to define respectively the self and distinct pair correlation functions, as

$$G_s(\mathbf{r}, t) = \frac{1}{N} \sum_j \int \langle \delta(\mathbf{r}' - \mathbf{R}_j(0)) \delta(\mathbf{r}' + \mathbf{r} - \mathbf{R}_j(t)) \rangle d\mathbf{r}', \quad (5.14)$$

$$G_d(\mathbf{r}, t) = \frac{1}{N} \sum_{j \neq j'} \int \langle \delta(\mathbf{r}' - \mathbf{R}_{j'}(0)) \delta(\mathbf{r}' + \mathbf{r} - \mathbf{R}_j(t)) \rangle d\mathbf{r}', \quad (5.15)$$

with $G(\mathbf{r}, t) = G_s(\mathbf{r}, t) + G_d(\mathbf{r}, t)$. Moreover, in the hypothesis of no correlation between the scattering lengths b_j and $b_{j'}$ and the position of the nuclei j and j' the corresponding sum in Eq. 5.10 has to be averaged over the sample volume

$$\text{for } j \neq j' : \langle b_j b_{j'} \rangle = \langle b_j \rangle \langle b_{j'} \rangle = \langle b \rangle^2, \quad (5.16)$$

$$\text{for } j = j' : \langle b_j b_{j'} \rangle = \langle b_j^2 \rangle = \langle b^2 \rangle. \quad (5.17)$$

Defining the coherent and incoherent scattering cross section with, respectively

$$\sigma_{coh} = 4\pi \langle b \rangle^2 \quad (5.18)$$

$$\sigma_{inc} = 4\pi (\langle b^2 \rangle - \langle b \rangle^2) \quad (5.19)$$

and inserting the definition of G_s and G_d into Eq. 5.10, yields finally

$$\frac{d^2 \sigma}{d\Omega d\omega} = \frac{k'}{k} \int \left(\int (\langle b \rangle^2 G(\mathbf{r}, t) + (\langle b^2 \rangle - \langle b \rangle^2) G_s(\mathbf{r}, t)) e^{i\mathbf{Q} \cdot \mathbf{r}} d\mathbf{r} \right) e^{-i\omega t} dt = \quad (5.20)$$

$$= \frac{k'}{k} \left(\frac{\sigma_{coh}}{4\pi} S(\mathbf{Q}, \omega) + \frac{\sigma_{inc}}{4\pi} S_s(\mathbf{Q}, \omega) \right). \quad (5.21)$$

The last expression is the sum of two contributions. The first term, described by the total dynamical structure factor $S(\mathbf{Q}, \omega)$ and weighted by the coherent cross section, is due to coherent scattering and gives information on spatial correlation and collective motions of the particles. While the second term, described by the self dynamical structure factor $S_s(\mathbf{Q}, \omega)$ and weighted by the incoherent cross section, is due to incoherent scattering and gives information on single-particle motions (e.g. vibrational or diffusive motion). It is important to mention the case of hydrogen, that is a strong incoherent scatterer ($\sigma_{inc} = 80.3 \text{ barn} \gg \sigma_{coh} = 1.8 \text{ barn}$), while for deuterium the coherent contribution is higher respect to the incoherent one ($\sigma_{coh} = 5.6 \text{ barn} > \sigma_{inc} = 2.1 \text{ barn}$). Therefore with a suitable process of deuteration of the investigated sample, it is possible to distinguish between coherent and incoherent scattering.

The theory just exposed above is useful for monoatomic scattering systems. Its extension to the molecular case can be readily made [84], taking into account, in some cases, also quantum effects that come from exchange interaction of the nuclei of the same species within the molecule. A rigorous calculation of the scattering cross section requires some hypotheses about the state of the molecular system and the dynamics of the internal and translational motions

of the molecule, and a complete discussion of all possible molecular systems is beyond the scope of this work. However in the following (Section 5.3) we have reported the case of inelastic scattering by a homonuclear diatomic molecule (H_2), which is the subject of our experimental work. In this work neutrons has been used also to measure diffraction from a solid sample. The principles of neutrons diffraction from a crystal will be summarized in the next Section 5.2.

5.2 Neutron diffraction

Neutron diffraction is a very useful technique for static structure determination of a material system. It is complementary to X-rays diffraction, which has a low sensitivity to light elements. Diffraction of neutron occurs as a consequence of the wave nature of matter particles, in analogy with the diffraction of electromagnetic waves, e.g. X-rays in a crystal or light waves from a diffraction grating.

The diffraction conditions of waves in a crystal were explained in 1912 by W. Bragg. The diffraction can be considered as the consequence of the reflections of the incident beam by various crystal lattice planes belonging to the same family, that is characterized by a certain set of Miller indexes (h, k, l) , i.e. it is the consequence of the constructive interference of the scattering from nuclei lying on lattice planes of the same family. A schematic picture of this effect is reported in Figure 5.3. Let consider a wave having wavelength λ , incident at a scattering angle θ on two planes with interplanar spacing d_{hkl} . The path difference between the two scattered waves is given by $2d_{hkl} \sin(\theta)$. The condition of constructive interference is obtained if the path difference is an integer multiple n of the wavelength, i.e.

$$n\lambda = 2d_{hkl} \sin(\theta). \quad (5.22)$$

This equation is called Bragg condition and indicates at which angle, usually

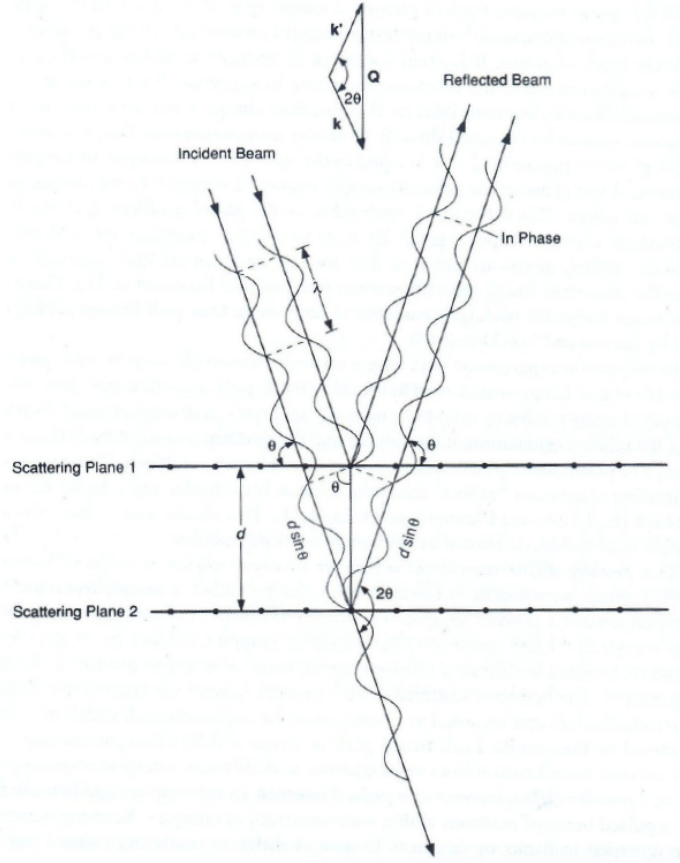


Figure 5.3: *Schematic view of Bragg reflections from two lattice planes belonging to the same family characterized by Miller indexes (h, k, l) and interplanar spacing d .*

called Bragg angle, a reflection relative to the same family of lattice plane (h, k, l) occurs. The number n is named the order of the diffraction. This law applies both to X-rays and neutrons. For the latter, the wavelength is derived from their velocity v by de Broglie relation

$$\lambda = \frac{h}{mv} \quad (5.23)$$

where h is the Plank constant and m is the neutron mass.

From a quantitative point of view, the single-differential neutron cross sec-

tion can be obtained by integrating the Eq. 5.10 over all the possible exchanged energies $\hbar\omega$

$$\frac{d\sigma}{d\Omega} = \int_{-\infty}^{\infty} \left(\frac{d^2\sigma}{d\Omega d\omega} \right) d\omega = \quad (5.24)$$

$$\int_{-\infty}^{\infty} \frac{k'}{k} \left(\frac{1}{2\pi} \right) \sum_{j,j'} b_j b_{j'} \int_{-\infty}^{\infty} \langle e^{-i\mathbf{Q}\cdot\mathbf{R}_{j'}(0)} e^{i\mathbf{Q}\cdot\mathbf{R}_j(t)} \rangle e^{-i\omega t} dt d\omega. \quad (5.25)$$

We introduce the simplification of considering the position of nuclei as fixed in space, since we are interested to determine the positions of all the atoms in a Bravais crystal at thermal equilibrium, characterized by N_0 unit cells, each one with volume v_0 . Considering a specific condition, in which the energy of the incident neutrons is much larger than any energy exchange which can take place between neutrons and sample during the scattering event, we can use the so-called static approximation, i.e. $\hbar\omega \simeq 0$, from which it follows $k' \simeq k$. Separating the coherent and incoherent contributions, two elastic cross section can be defined

$$\left(\frac{d\sigma}{d\Omega} \right)_{inc} = (\langle b^2 \rangle - \langle b \rangle^2) \sum_{j=j'} e^{-i\mathbf{Q}\cdot(\mathbf{R}_{j'} - \mathbf{R}_j)} = N(\langle b^2 \rangle - \langle b \rangle^2), \quad (5.26)$$

$$\left(\frac{d\sigma}{d\Omega} \right)_{coh} = \langle b \rangle^2 \sum_{j,j'} e^{-i\mathbf{Q}\cdot(\mathbf{R}_{j'} - \mathbf{R}_j)}. \quad (5.27)$$

The incoherent part is isotropic and yields a constant background, while the structural informations are contained in the coherent part, that can be written applying the substitution $\mathbf{r} = \mathbf{R}_j - \mathbf{R}_{j'}$:

$$\left(\frac{d\sigma}{d\Omega} \right)_{coh} = N_0 \langle b \rangle^2 \sum_{\mathbf{r}} e^{i\mathbf{Q}\cdot\mathbf{r}} = N_0 \frac{(2\pi)^3}{v_0} \langle b \rangle^2 \sum_{\boldsymbol{\tau}} \delta(\mathbf{Q} - \boldsymbol{\tau}), \quad (5.28)$$

where $\boldsymbol{\tau}$ denotes a reciprocal lattice vector. The last expression indicates that the coherent elastic cross section is not-zero only when the momentum transfer vector \mathbf{Q} coincides with a vector of the reciprocal lattice $\boldsymbol{\tau}$. In the case of a non-Bravais crystal, i.e. a crystal with more than one atom per unit cell, the

position vector of the atoms is

$$\mathbf{R}_{j,\alpha} = \mathbf{l}_j + \mathbf{d}_\alpha, \quad (5.29)$$

with \mathbf{l}_j is the position vector of the origin of the j -th unit cell and \mathbf{d}_α is the position vector of the α -th atom in the unit cell. In this case, introducing $\mathbf{d} = \mathbf{d}_\alpha - \mathbf{d}_{\alpha'}$, the cross section is given by

$$\begin{aligned} \left(\frac{d\sigma}{d\Omega} \right)_{coh} &= \sum_{j,j'} e^{i\mathbf{Q} \cdot (\mathbf{l}_j - \mathbf{l}_{j'})} \sum_{\alpha,\alpha'} b_\alpha b_{\alpha'} e^{i\mathbf{Q} \cdot (\mathbf{d}_\alpha - \mathbf{d}_{\alpha'})} = \\ &= \sum_{j,j'} e^{i\mathbf{Q} \cdot (\mathbf{l}_j - \mathbf{l}_{j'})} \left| \sum_{\mathbf{d}} b_{\mathbf{d}} e^{i\mathbf{Q} \cdot \mathbf{d}} \right|^2. \end{aligned} \quad (5.30)$$

Furthermore, considering a not rigid lattice, the complete expression for the elastic coherent cross section is [85]

$$\left(\frac{d\sigma}{d\Omega} \right)_{coh} = N_0 \frac{(2\pi)^3}{v_0} e^{-2W(\mathbf{Q})} \sum_{\boldsymbol{\tau}} |S_{\boldsymbol{\tau}}|^2 \delta(\mathbf{Q} - \boldsymbol{\tau}), \quad (5.31)$$

where the informations on the unit cell symmetry, i.e. size and form, are contained in the δ -function. Indeed the scattering process gives rise to a peak in the diffraction pattern only when the momentum transfer \mathbf{Q} of the neutron coincides with a reciprocal lattice vector $\boldsymbol{\tau}$ of the crystal, i.e. $\mathbf{Q} = \boldsymbol{\tau}$. Each reciprocal lattice vector $\boldsymbol{\tau}$ is perpendicular to the corresponding reflection plane denoted by the Miller indexes (h, k, l) , whose interdistance is

$$d_{hkl} = \frac{2\pi}{|\boldsymbol{\tau}_{hkl}|}. \quad (5.32)$$

From this the Bragg law (Eq. 5.22) easily follows. Anyway, mostly due to instrumental resolution, the peaks in the diffraction pattern do not have the shape of δ -function and peak-shape functions are introduced in the data analysis for reproducing the experimental peak profiles. The intensity of the Bragg reflections in the diffraction pattern is determined by the so-called structure factor $S_{\boldsymbol{\tau}}$, defined as

$$S_{\boldsymbol{\tau}} = \sum_{\mathbf{d}} b_{\mathbf{d}} e^{i\boldsymbol{\tau} \cdot \mathbf{d}}, \quad (5.33)$$

which contains the informations on the atom location within the unit cell. The further intensity factor $e^{-2W(\mathbf{Q})}$, known as Debye-Waller, takes into account the mean-square displacements of the nuclei from their equilibrium position and strongly depend on the symmetry of the considered crystal [83].

5.3 Inelastic neutron scattering from the hydrogen molecule

Inelastic neutron scattering (INS) is an extremely useful tool for investigating at a microscopic level the dynamic properties of a material system. The typical wide spectral range of an INS spectrometer allows to cover the whole molecular vibrational range of both lattice modes and intramolecular modes, without involving any selection rules typical of the optical spectroscopy. In this paragraph we want to derive some relations that will be useful in the following when dealing with inelastic neutron scattering from a system containing hydrogen molecules. INS spectra are quite sensitive to hydrogen molecule dynamics, due to the large incoherent neutron scattering cross section of the proton, nearly two orders of magnitude greater than that of any other nucleus. Moreover a selective sample deuteration allows to put in evidence the incoherent dynamics of just some molecules or functional groups.

The hydrogen molecule represents the simplest example of diatomic homonuclear mono-isotopic molecule. Considering its dynamics, all the degrees of freedom of the molecule have to be taken into account. In the Born-Oppenheimer approximation and considering that the energies of the translational, rotational and vibrational motions are quite different, i.e. $E_{trans} \ll E_{rot} \ll E_{vib}$, the total wave function of the molecule can be written as a product of single wave functions

$$\Psi = \Psi_{trans} \Psi_{rot} \Psi_{vib} \Psi_{el} \Psi_{spin}, \quad (5.34)$$

where the spin state depends on the configurational state of the molecule. Considering the case of thermal neutron scattering, the molecule remains in the electronic fundamental state. Since the nuclei are fermions (nuclear spin $I = 1/2$), the total wave function of the molecule must be antisymmetric for the exchange of two nuclei. Hence the hydrogen molecule, having two possible spin states and taking into account the symmetry of each single wave functions, can belong to one of the two possible species:

- *para* hydrogen, if the molecule is in the antisymmetric total spin state $S = 0$ (anti-parallel spins) and its rotational state is characterised by an even quantum rotational number J ;
- *ortho* hydrogen, if the molecule is in the symmetric total spin state $S = 1$ (parallel spins) and its rotational state is characterised by an odd quantum rotational number J .

If we consider a system of N H_2 molecules (for example in the liquid phase) interacting by means of an isotropic intermolecular potential, it is possible to decouple the internal motions from the center of mass (c.m.) motion of the molecule. Thus, using the formalism of the Van Hove intermediate scattering functions for the c.m. of the molecules, the double differential neutron scattering cross section can be written as [86]

$$\frac{d^2\sigma}{d\Omega d\omega} = \frac{k'}{k} \frac{1}{2\pi} \int (F_d(Q, t)u(Q) + F_s(Q, t)v(Q, t)) e^{-i\omega t} dt \quad (5.35)$$

where the distinct and self part of intermediate scattering function are expressed respectively, by

$$F_d(Q, t) = \frac{1}{N} \sum_{j \neq j'} \langle e^{-i\mathbf{Q} \cdot \mathbf{R}_j(0)} e^{i\mathbf{Q} \cdot \mathbf{R}_{j'}(t)} \rangle, \quad (5.36)$$

$$F_s(Q, t) = \frac{1}{N} \sum_j \langle e^{-i\mathbf{Q} \cdot \mathbf{R}_j(0)} e^{i\mathbf{Q} \cdot \mathbf{R}_j(t)} \rangle. \quad (5.37)$$

The functions $u(Q)$ and $v(Q, t)$ depend on the intramolecular motions and it is possible to explicit them using the decoupled quantum models for the free rotator and harmonic oscillator [87]. The distinct part of the cross section can be immediately integrated, thus obtaining

$$\left(\frac{d^2\sigma}{d\Omega d\omega} \right)_d = \frac{k'}{k} S_d(Q, \omega) u(Q), \quad (5.38)$$

where the distinct structure factor $S_d(Q, \omega)$ describes the collective properties of the system, and $u(Q)$ is not zero only for rotational transitions with $\Delta J = 0$ and vibrational transitions with $\Delta\nu = 0$, that is the intramolecular transitions appear only in the inelastic self spectrum. Furthermore, in the hydrogen case, the distinct part is largely less intense compared to the self one, since it is proportional only to σ_{coh} . For what concern the self part, $v(Q, t)$ can be written as the sum of different terms depending on parity of rotational states [86]. The integration of the self contribution of Eq. 5.35 yields

$$\left(\frac{d^2\sigma}{d\Omega d\omega} \right)_s = \frac{k'}{k} \sum_{rot, vib} S_s(Q, \omega) \otimes \delta(\omega - \omega_{\Delta J} - \omega_{\Delta\nu}) s_{xx}^2(I) f(J_i, J_f, \nu_f, Q) \quad (5.39)$$

where $S_s(Q, \omega)$ is the self dynamic structure factor of c.m. of the molecule, s_{xx} and f are intensity factors, and the subscript xx indicates the parity (e for even case, o for odd case) of the initial and final rotational states, i.e. s_{ee} , s_{oo} , s_{eo} and s_{oe} . Hence the spectrum consists of some lines, placed at the roto-vibrational frequencies, whose intensities depend on the s_{xx} and f factors, convoluted with the self spectrum of the c.m. motion $S_s(Q, \omega)$. For example the spectrum of liquid para- H_2 , measured at temperature of 17.2 K, is reported in Figure 5.4. In the case of para- H_2 at this low temperature, only the rotational state with $J = 0$ is populated, and only the bands corresponding to even \rightarrow odd transitions are visible, since they are the only ones being weighted by σ_{inc} . Each rotational line is broadened and shifted by the c.m. motion [88].

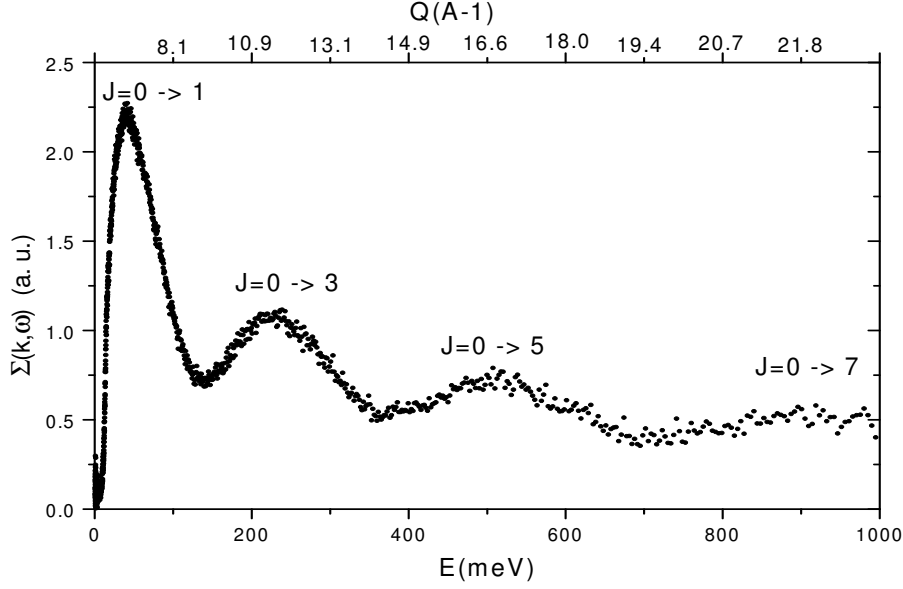


Figure 5.4: *Spectrum of liquid para-hydrogen measured at temperature of 17.2 K with TOSCA spectrometer (ISIS-RAL, U.K.) [89].*

5.4 Neutron spectrometer: TOSCA

In this work the vibrational dynamics of the hydrogen molecules contained in our samples has been studied by means of the TOSCA instrument, that is an inverse geometry time-of-flight INS spectrometer located at ISIS (RAL, U.K.) [90]. This instrument is optimised for vibrational spectroscopy, thanks to its almost constant high resolution $\Delta\omega/\omega \sim 2\%$ in the energy range 5 - 1000 meV. A schematic drawing of its layout is reported in Figure 5.5. The incident neutron beam comes from the 300 K water moderator, to which the instrument is connected. The final energy of the neutrons E_f , i.e. their energy after the scattering on the sample, is selected by means of graphite crystal analysers placed at the angles 45° (forward scattering) and 135° (backward scattering)

respect to the incident beam. The outgoing neutrons from the crystal have a wavelength λ determined by the Bragg's law $m\lambda = 2d\sin(\theta)$ (see Eq. 5.22), where m is the diffraction order, d is the interplanar distance in the crystal and θ is the incidence angle on the crystal. Along the neutron path, after each crystal analyser, a beryllium filter is placed and kept at low temperature by means of a closed cycle refrigerator. This act as a high-pass filter and allow to cut the higher diffraction order ($\lambda/2, \lambda/3, \dots$) coming from the analyzers. The transmitted neutrons are then detected by the ^3He detectors.

The time-of-flight technique is used for the energy analysis of the scattered neutrons. The neutron energy E exchanged with the sample is simply given by

$$E = E_i - E_f \quad (5.40)$$

where E_i is the incident energy of the neutron. The total time-of-flight t of a single neutron is the sum of two contributions, that are the time t_i needed to cover the path L from the moderator to the sample and the time t_f needed to cover the path l from the sample to the detector,

$$t = t_i + t_f = \frac{L}{\sqrt{\frac{2(E+E_f)}{m_n}}} + \frac{l}{\sqrt{\frac{2E_f}{m_n}}}. \quad (5.41)$$

Since both path length are known ($L = 17$ m, $l \sim 0.6$ m), measuring the total time-of-flight t , it is possible to calculate the exchanged energy E by inverting the previous equation. On TOSCA, due to its configuration, is not possible to perform measurements at a constant value of momentum transfer Q . However, this spectrometer is used mainly to study undispersed modes in solids or phonon densities of states, where the Q -dependence is not usually crucial.

The intensity of the fundamental i -th molecular vibrational transition is proportional to

$$I_i \propto \sigma Q^2 U_i^2 e^{-2W(Q)} \quad (5.42)$$

where σ is the neutron cross section of atoms involved in the mode and U_i is the amplitude of their vibration. The exponential is the so called Debye-Waller factor and is related to the mean square displacement of the scatterer atoms. $W(Q)$ can be reduced to the zero-point value, by cooling the sample. For any practical purpose a temperature of about 20 K is considered low enough for most of the crystal samples analysed with TOSCA.

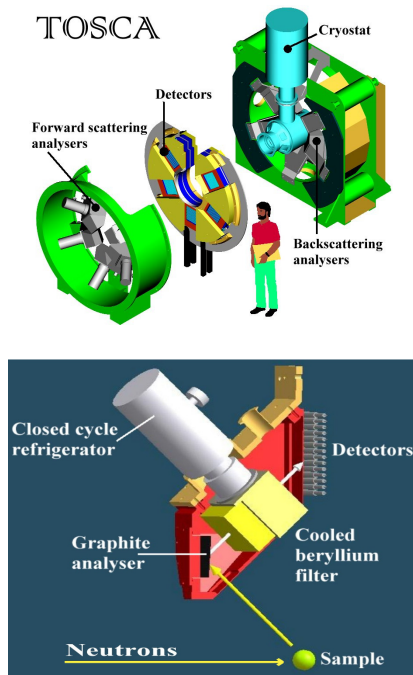


Figure 5.5: A schematic view of TOSCA spectrometer [90] (upper panel) and its section through one of the analyzer modules (lower panel).



Figure 5.6: The typical TOSCA center-stick.

In our experiment the sample cell, attached at the bottom of an aluminium center-stick (Figure 5.6), is placed in a Closed Cycle Refrigerator (CCR), which attains temperatures of about 5 K as minimum on sample region. The CCR

is not in direct thermal contact with the sample and helium gas is used as exchange gas to cool the sample. The aluminium neutron cell, shown in Figure

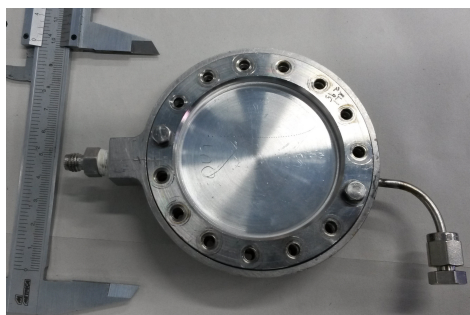


Figure 5.7: *The aluminium TOSCA neutron cell suitable for pressure of a few bar.*

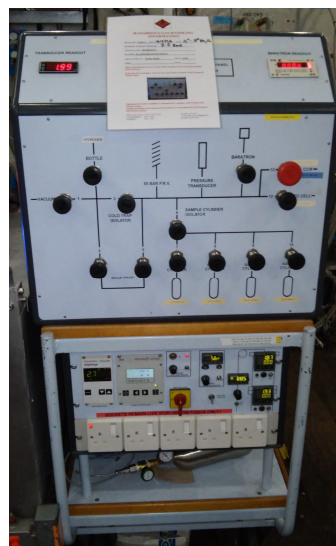


Figure 5.8: *The gas handling panel available on TOSCA.*

5.7, has a planar geometry and the thickness can be varied depending on the type of sample analysed or experiment performed. In this case its aluminium covers have a thickness of 1.5 mm, that allows to sustain internal pressure of 5 bar. The cell is equipped with one temperature sensors and one heater, fixed by a screw on the external edge of the cell. The cell has a gas inlet that is connected through a steel capillary to a vacuum and gas control system (Figure 5.8), provided with a turbo-molecular vacuum pump, a H_2 gas bottle, two pressure transducers with, respectively, 2.5 bar and 1 bar full scale range and

4 empty bottles, each one with volume of about 1 l, used as exchange volumes. The gas circuit is also connected to a catalyst system for the production of para-hydrogen. Moreover an additional heater has been used in order to prevent the formation of solid plugs, positioned along the portion of capillary that enters within the CCR vessel, due to the low working temperature.

5.4.1 Scientific case: the clathrate-hydrates on TOSCA

In the past a lot of efforts have been done for studying the incoherent dynamic of hydrogen molecules nanoconfined in different host materials. In order to give an example of a scientific case similar to that treated in this work, we will discuss here the case of clathrate-hydrates [56, 91, 92]. In a deuterated water framework, the relevant hydrogen content, typical of clathrate, allows to obtain quite intense bands in the spectra, while the host vibrational modes are typically quite small. Neglecting the coherent part of the scattering, the incoherent spectrum can be written as [91]

$$\left(\frac{d^2\sigma}{d\Omega d\omega} \right)_s = \frac{k'}{k} S_s(Q, \omega) \otimes \sum_{J_i, J_f} \delta(\omega - \omega_{J_i, J_f}) \nu(J_i, J_f, Q) \quad (5.43)$$

where the internal motions of the H₂ molecule, modelled as rigid rotator by the δ -functions with intensity factor $\nu(J_i, J_f, Q)$, are decoupled from the H₂ c.m. motion inside the clathrate cages. In the spectra, reported for a binary (THF + H₂) clathrate in Figure 5.9, the bands at lower energy transfer were assigned to different motions of encaged hydrogen molecules. The first, located at about 10 meV, is assigned to the rattling mode, i.e. the translation motion of H₂ center-of-mass, that is Raman inactive. The second, located at 14 meV, is assigned to the rotational motion. It is important to underline that, for H₂, INS spectra display the rotational $\Delta J = 1$ transitions, e.g., $J = 0 \rightarrow 1$ of para-H₂ (p-H₂) and $J = 1 \rightarrow 2$ of ortho-H₂ (o-H₂), which are forbidden in optical spectroscopy (IR and Raman) for H₂. Moreover, the fine structure

of both translational and rotational bands denotes a substantial anisotropic interaction with the water environment [91].

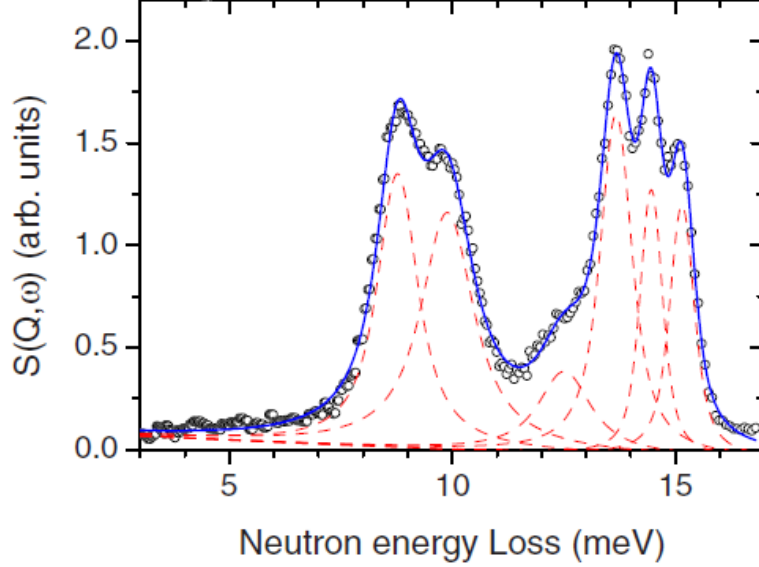


Figure 5.9: *Inelastic incoherent neutron spectrum of rattling and rotational transition of hydrogen molecules within a binary D_2O clathrate ($TDF + H_2$). The measurement, performed on TOSCA spectrometer (ISIS facility, RAL, UK) at temperature of about 20 K, is taken from ref. [91].*

Besides the guest motion, the clathrate lattice dynamics has a large interest, due to the analogies with ice, and to the existence of various structures. Incoherent inelastic neutron scattering can be used to study their phonon density of states projected to hydrogen atom (H-PDoS), $G_H(E)$, since this quantity is directly related on the single-phonon incoherent spectrum $S_{s,+1}(Q, E)$ by the relation [92]

$$G_H(E) \cong \frac{4m_H E}{\hbar^2 Q^2} \left(\coth \left(\frac{E}{2k_B T} \right) + 1 \right)^{-1} e^{\frac{Q^2 \langle u_H^2 \rangle}{3}} S_{s,+1}(Q, E) \quad (5.44)$$

where $\langle u_H^2 \rangle$ is the proton mean square displacement. An example of this is reported in Figure 5.10, where the samples studied are three clathrates made of light water, having different structures (i.e. simple sI structure with Xe,

simple sII structure with fully deuterated tetrahydrofuran (TDF), and binary sH structure with methyl tert-butyl ether (MTBE) and D_2). Because guest molecules are fully deuterated, their spectral contribution is negligible compared to the host scattering intensity, and only lattice vibrational bands appear in the spectrum. Thus, it is possible to assign the first band ($E < 40$ meV) to acoustic and optical modes, while the quite wide and intense one, located in the region $60 \text{ meV} < E < 130 \text{ meV}$, is attributed to the librational motion of water molecule in the crystalline lattice.

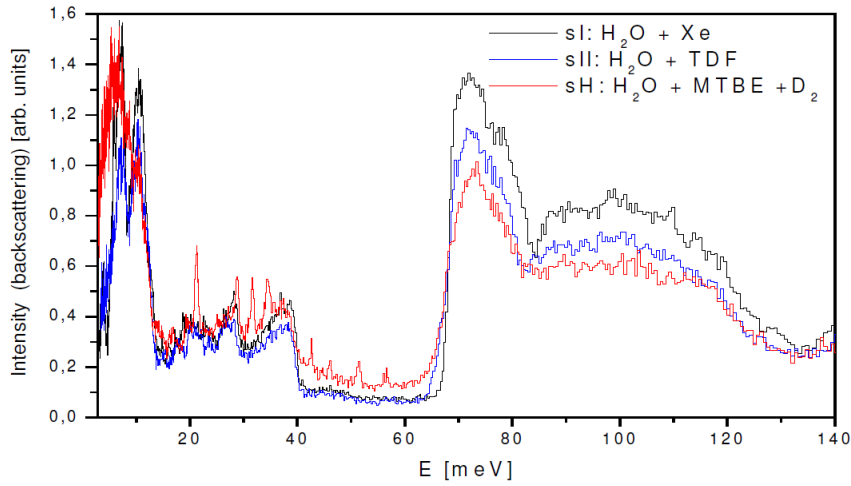


Figure 5.10: *Neutron scattering spectra of different type of H_2O clathrate measured at temperature of about 20 K on TOSCA spectrometer (ISIS facility, RAL, UK) [92]. Their composition is indicated in the legend.*

5.5 Neutron diffractometers: OSIRIS and WISH

The static structure of our hydrate samples has been studied with two different neutron diffractometers, namely OSIRIS and WISH. The first instrument is able to measure at the same time both elastic and quasi-elastic scattering. In our experiment we have performed both the analyses, but, in this work, we will

present only the neutron diffraction results. Therefore only the characteristics of the instrument concerning diffraction measurements are described in this section. The second instrument, WISH, is only a diffractometer.

OSIRIS diffractometer The OSIRIS diffractometer is placed at ISIS facility (RAL, U.K.), in the first target station (TS1) [93]. The schematic layout of the diffractometer and an experimental scheme are presented in Figure 5.11 and Figure 5.12, respectively. The instrument uses neutrons deriving from

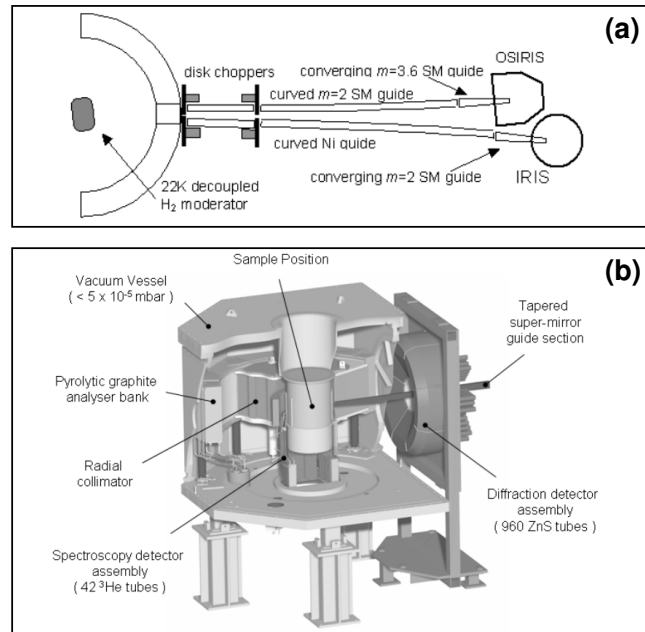


Figure 5.11: *Schematic layout of OSIRIS instrument [94]. In the panels (a) and (b) are reported the primary (moderator-sample) and secondary (sample-detector) paths, respectively.*

the liquid H₂ moderator cooled at 25 K that produces a large flux of long wavelength (cold) neutrons. The neutrons are transported from the moderator to the sample position by a curved neutron guide. The incident energy range, i.e. the lower and upper limits of the wavelength band incident onto the sample, is selected by phasing properly two disk chopper placed after 6.3 m and

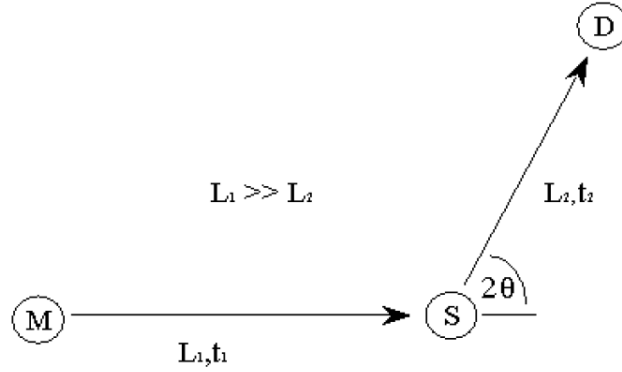


Figure 5.12: *Schematic view of a diffraction experiment [94].*

10.0 m from the moderator. Once neutrons are scattered by the sample, they reach directly the diffraction detectors, constituted of 962 ZnS tubes placed at large scattering angles 2θ ($150^\circ < 2\theta < 171^\circ$). The d -spacing of the observed Bragg reflection is determined by time-of-flight (tof) analysis. Defining with $L = L_1 + L_2 = 35.005$ m the total flight path, and with $t = t_1 + t_2$ the total flight time, by means of the de Broglie relation, it is possible to write the wavelength of the scattered neutrons λ in term of the measured total tof t

$$m \left(\frac{L}{t} \right) = \frac{h}{\lambda} \Rightarrow \lambda = \frac{ht}{mL}. \quad (5.45)$$

By means of Bragg condition (Eq. 5.22), the measured d -spacing is given by

$$d = \frac{ht}{2mL \sin \theta}. \quad (5.46)$$

with a good resolution, namely $\Delta d/d = (2.5 \div 6.0) \cdot 10^{-3}$. It is necessary to adjust the phase of two choppers to obtain a series of overlapping d -spacing ranges, namely d -range, to cover the complete interval of interest (at maximum from 0.8 Å to 20 Å) necessary for a complete structural characterization of the sample. The acquired data of each d -range interval are merged automatically by a dedicated software to create a single diffraction pattern that covers the d -spacing region of interest in a continuous manner.

In our experiment the sample cell, attached at the bottom of an aluminium center-stick, is placed in a vessel, which can be maintained at low temperature by a cryogenic system similar to that described for TOSCA spectrometer. The aluminium neutron cell, shown in Figure 5.13, has an annular geometry with working internal thickness of 2 mm. The cell is equipped with two temperature sensors, placed on the top and on the bottom side in order to take into account possible thermal gradient along the cell, and with a heater. Moreover the cell has a gas inlet that is connected through a steel capillary to the vacuum and gas control system.



Figure 5.13: *The OSIRIS annular aluminium cell, equipped with gas valve on the top. The copper clips on the upper and lower side host temperature sensors and/or heaters.*

The raw output data of an acquisition performed with OSIRIS diffractometer are the sum, for each time channel, of counts recorded by each back-scattering detector in a time-of-flight window, i.e. d -range, selected by a specific chopper setting. By means of the MANTID software [95] the data con-

tained in different files, corresponding to different tof windows, are normalized by monitor counts, measured during each spectrum acquisition, and by a vanadium dataset, available on the instrument database. In neutron diffraction the normalization of the measured data is carried out by comparing the sample diffraction intensity with the measured intensity of a sample of known scattering cross-section. Generally vanadium is used as a normalization standard, indeed its cross section is known rather accurately and it is an elastic scatterer almost completely incoherent, so that its scattering is almost isotropic. After the normalization, the data are then merged into a single file containing the whole tof range.

WISH diffractometer The WISH diffractometer is placed at the second target station (TS2) at the ISIS facility (RAL, U.K.) [96]. Its schematic layout is presented in Figure 5.14. The neutrons, coming from the solid methane moderator operating at 40 K, are driven to the sample region by an elliptical guide. Along the 40 m moderator-sample path (primary), two counter-rotating double-disk choppers and one single-disk chopper are located, and they are properly phased for bandwidth selection and for preventing frame overlap. The neutrons scattered from the sample are collected by a ^3He gas tube array positioned at 2.2 m from the sample point and arranged on a cylindrical locus from 10° to 170° scattering angles (2θ). As well as in the OSIRIS case, the d -spacing of the observed Bragg reflections is determined by time-of-flight (tof) analysis.

In our experiment, as common for ISIS instrumental configuration, the sample can is attached at the bottom of an aluminium center-stick, and they are placed in a vessel, which can be maintained at low temperature by a cryogenic system similar to that described for TOSCA spectrometer. The vanadium can used in this experiment (Figure 5.15) has an annular geometry with working internal diameter of 6 mm. The cans have the advantage of

giving an almost negligible coherent contribution to the scattering, but they cannot contain free hydrogen gas, due to hydrogen embrittlement of vanadium. Since the little dimensions of the can, it goes quite quickly at equilibrium with cryostat temperature, that is assumed as the nominal temperature of the sample. The cell is not provided of a gas-insertion system.

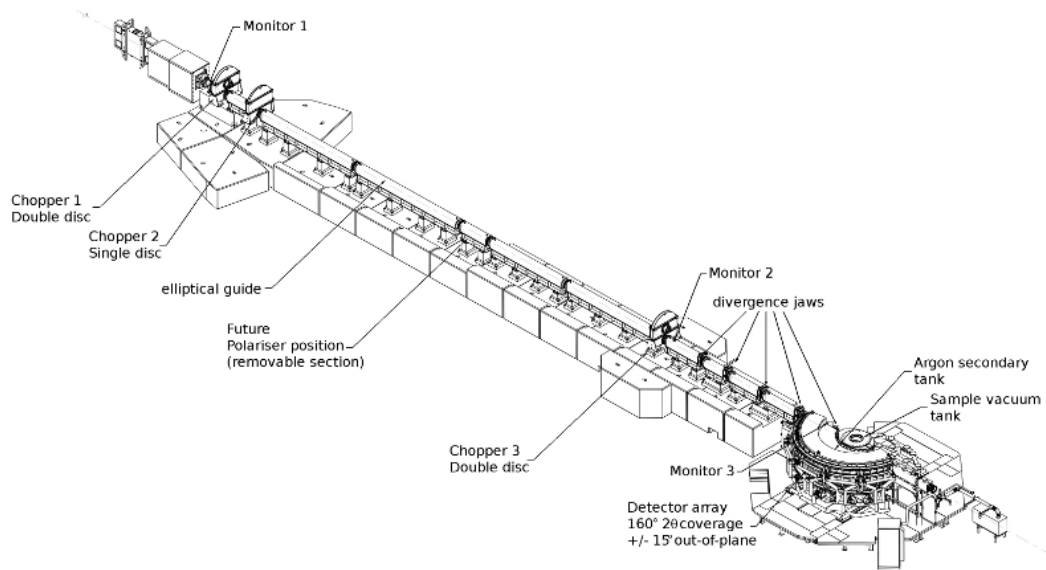


Figure 5.14: *Schematic picture of WISH diffractometer [96].*

The raw output data of an acquisition performed with WISH diffractometer are the sum, for each time channel, of counts recorded by each detector in a time-of-flight window selected by the choppers setting. As in the OSIRIS measurements, also in this case the raw data are processed by a MANTID routine for their normalization.



Figure 5.15: *The typical vanadium cans available at ISIS facility and used for diffractometers.*

Part III

Experimental results and discussion



Chapter 6

Raman data of the C₀-phase and ice XVII

In this chapter we focus our attention on the dynamics results obtained by using Raman spectroscopy. The Raman characterization of the C₀-phase has been the first experiment performed on this type of sample during this work, while the discovery of a new form of metastable ice has occurred subsequently. Only after this moment the determination of the structure has become crucial to confirm the discovery a new form of ice.

The results presented in this chapter (about Raman spectroscopy) and in the following chapters (about neutron spectroscopy and diffraction) reflect, almost totally, the chronological order in which the experiments have been performed.

6.1 The Raman characterization of the C₀-phase

For a complete characterization of the dynamics of the pristine sample we have measured the Raman bands originated by both the vibrational motions of the host molecules, i.e. lattice phonon and O–H stretching mode, and of the guest

molecules, i.e. rotational e (intra-molecular) vibrational mode.

Lattice band The Raman spectrum of the lattice phonon mode, measured in the region $150\text{-}320\text{ cm}^{-1}$, appears as a broad smooth band, showing similarities with the same band in ice Ih and in sII clathrate (Figure 6.1). The main peak, located at $\simeq 215\text{ cm}^{-1}$, is broader than in clathrates or ice Ih , while the region around 315 cm^{-1} is almost flat, thus testifying the absence of ice Ih contamination in the sample, possibly due to water vapour condensation. These broad features, originated by various lattice vibrations, result from the

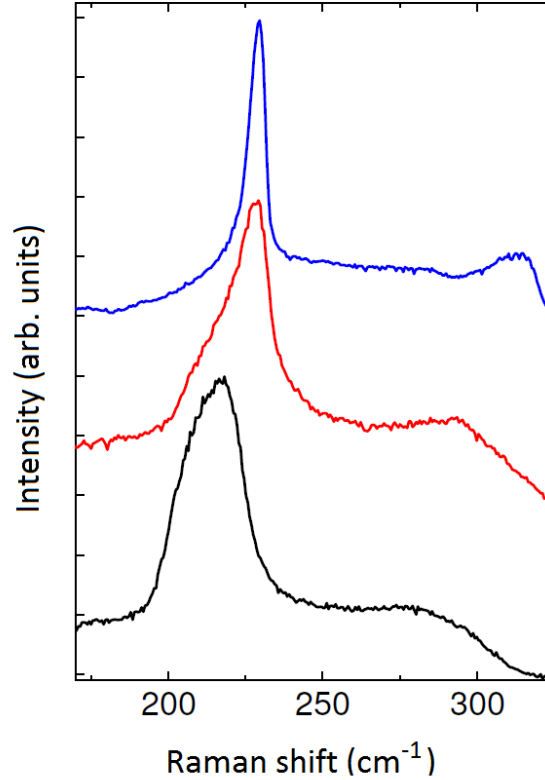


Figure 6.1: *Lattice phonon band in the Raman spectrum, measured at 30 K in the range $150\text{-}320\text{ cm}^{-1}$, of the C_0 -phase in the filled ice sample as synthesized (black line), sII clathrate (red line) and ice Ih (blue line).*

orientational disorder of water molecule located in the unit cell, leading to a

relaxation of selection rules [78]. In fact, it is experimentally demonstrated that sharp phonon zero-wave-vector modes characterize proton-ordered ice phases, as in the case of ice II [97], ice XI (the ordered form of ice Ih [80]), or filled ice having the C₁-structure [2]. From a comparison of the spectra in Figure 6.1, it can be deduced that the crystal structure of the C₀-phase is proton disordered.

O–H stretching band The Raman O–H stretching band of the water molecules in the C₀-phase has been measured in the range 3000-3400 cm⁻¹. The main peak is located at 3123 cm⁻¹, while the other peaks are at higher frequency. It is well known that Raman frequencies of O–H oscillators in H₂O depend strongly on the O–H···O hydrogen bond length. In the past it was demonstrated that the O–H vibrational frequency increases with increasing hydrogen-bond length, i.e. O–O distance d_{OO} , both by considering different hydrogen bonding compounds [98] or, for the same crystalline ice structure, as a function of pressure [99, 100]. From the comparison of the band position in the different ice phases (Figure 6.2), it is possible to deduce that for the C₀-phase the O–O distance is slightly higher than for the sII clathrate ($d_{OO} \simeq 2.77 - 2.79$ Å) and Ih ice ($d_{OO} \simeq 2.75$ Å) case. This is quantitatively verified if the C₀-phase is assumed to have $P3_112$ space group crystal symmetry [3], with parameters given in ref. [5], in which case $d_{OO} \simeq 2.83 - 2.85$ Å.

Rotational bands The rotational dynamics of the hydrogen molecule inside the host environment is investigated measuring the Raman active pure rotational transitions $S_0(J)$, where J denotes the initial rotational quantum number for the allowed Raman transitions $\Delta J = \pm 2$. The $S_0(0)$ para-H₂ and $S_0(1)$ ortho-H₂ bands have been measured in the frequency regions 325-380 cm⁻¹ and 525-650 cm⁻¹ respectively. At the temperatures of the experiment (30 K) it is possible to neglect the frequency region higher than 650 cm⁻¹ because only the states with $J = 0$ and $J = 1$ are populated. As it is shown in

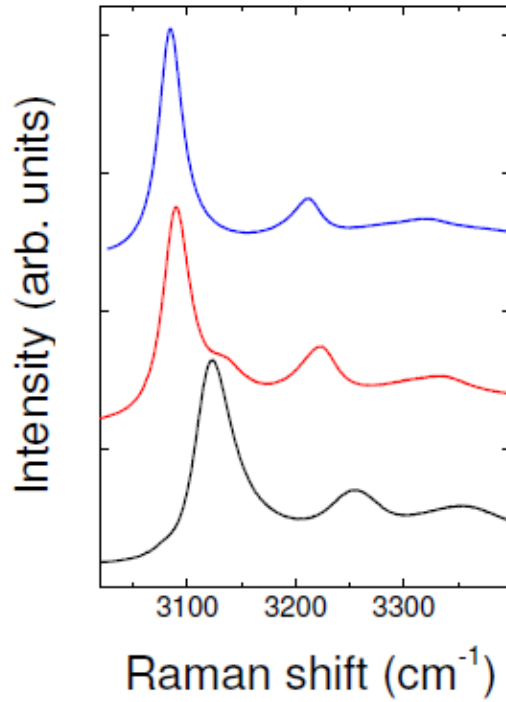


Figure 6.2: *OH-stretching band in the Raman spectrum, measured at 30 K in the range 3000-3400 cm⁻¹, of the C₀-phase in the filled ice sample as synthesized (black line), sII clathrate (red line) and ice Ih (blue line).*

Figure 6.3, the rotational spectrum presents two well distinct bands, proving that the H₂ molecules rotate almost freely, as it happens for H₂ in the clathrate cages [55, 68]. In the S₀(0) rotational band it is also possible to resolve a fine structure, probably due to partial removal of the fivefold degeneracy of the $J = 2$ level induced by the anisotropic crystal potential energy of the water environment. In particular, this effect is attributed to the electrostatic interaction of the H₂ quadrupole with the H₂O dipolar field. It is interesting to note that these bands appear wider than in clathrates, thus proving a stronger interaction of the H₂ molecule with the host skeleton. An indirect confirmation of this last deduction can be obtained considering the crystal structure proposed in Ref. [3]. According to this, the hydrogen molecules are

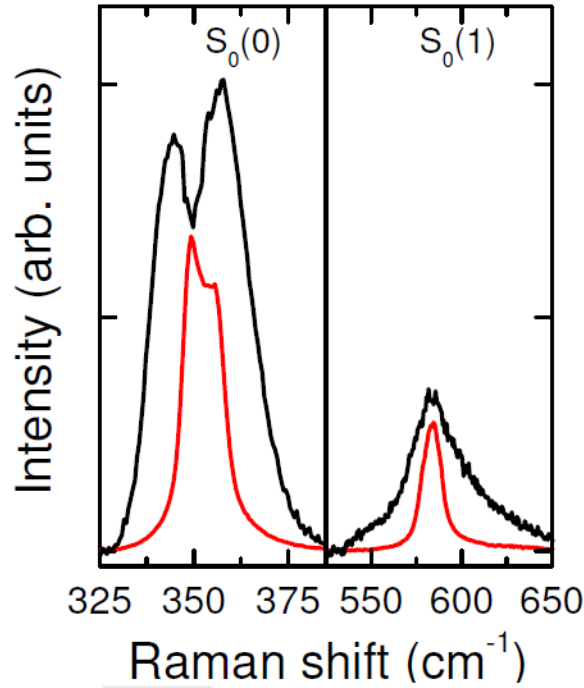


Figure 6.3: $S_0(0)$ and $S_0(1)$ rotational bands, originated by hydrogen molecules, in the Raman spectrum of the C_0 -phase in the filled ice sample (black line) compared to that observed in sII clathrate (red line). The spectra, measured at 30 K, are renormalized for easier comparison.

arranged in a channel frameworks, probably in a spiralling configuration, at a distance from water oxygen atoms of about 3.1 Å, which is shorter compared to guest-host distance in clathrate cages (e.g. about 4 Å for 5¹² small cage). In addition the H₂ molecules are arranged at about 2.95 Å between each other. Hence, at such a short distance, the H₂-H₂ anisotropic interaction may in principle sustain collective rotational excitations, as it happens in solid H₂ [101] and Ar(H₂)₂ high pressure compound [102, 103], which may contribute to the width of the rotational lines.

Vibrational band The vibrational dynamics of hydrogen molecules inside the C_0 -structure is analysed measuring the Raman spectrum of the vibrational transitions $Q_1(J)$ in the region $4100\text{--}4160\text{ cm}^{-1}$, where J denotes the rotational quantum number for the allowed Raman transitions $\Delta J = 0$ (Figure 6.4). The

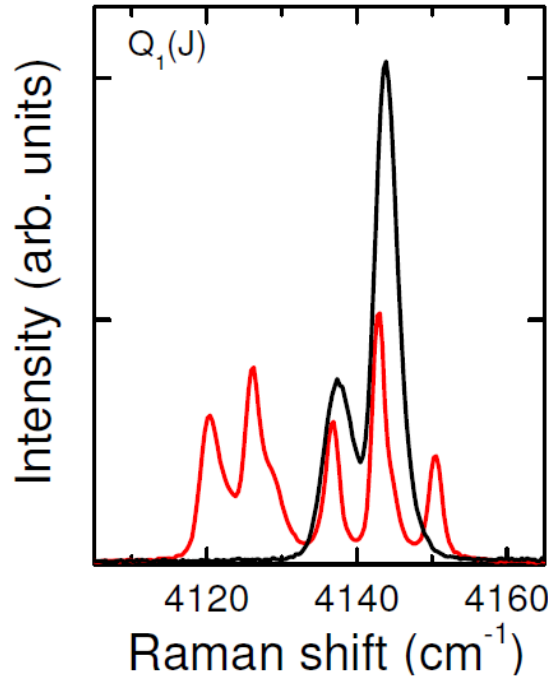


Figure 6.4: $Q_1(J)$ vibrational band, originated by hydrogen molecules, in the Raman spectrum of the C_0 -phase in the filled ice sample (black line) compared to that observed in sII clathrate (red line). The spectra, measured at 30 K, are renormalized for easier comparison.

Raman spectrum shows two well distinct peaks centered at about 4138 cm^{-1} and 4144 cm^{-1} . Their frequency separation of about $\simeq 6\text{ cm}^{-1}$ allows us to easily assign these peaks to the $Q_1(1)$ and $Q_1(0)$ modes of the H_2 molecule, respectively. As it happens in the clathrate [63, 64], the vibrational frequencies are downshifted in comparison to the hydrogen gas phase. This is probably due to the attractive component of the site-site interaction potential between

the molecules of the water skeleton and the H_2 molecule, since the diameter of sII clathrate cages (7.8 - 9.4 Å) are comparable with the channel diameter in the proposed C_0 -structure (6.1 Å) [3, 5]. In any case, it appears evident that there is only one doublet in the spectrum, hence every hydrogen molecule experiences the same potential or, from a structural point of view, the hydrogen molecule occupies only one crystallographic site. This fact corroborates the idea that the guest molecules are arranged in channel framework, probably in spiral configuration.

6.2 The annealing treatment and the discovery of ice XVII

An important point in the study of hydrate systems is the comprehension of what forces are predominant for the overall stability of the hydrate structure, and also to understand the role played by the guest gas molecules [7]. In this perspective it is of fundamental importance to study a possible mechanical stability of a water structure identical to the empty C_0 -phase, i.e. without the hydrogen guest. We have realized this study by subjecting the pristine sample to an annealing treatment, which is performed by keeping the sample under dynamic vacuum at a quite high temperature. The whole treatment is done in the Raman optical cell, thus measuring at any moment the Raman spectrum of the sample. We had previously verified that the C_0 -structure transform in ice, probably I_h , at about 130 K with a fast kinetics, hence the annealing temperature is set prudentially at 110 K and the sample is kept under dynamic vacuum for about one hour. As it is shown in Figure 6.5, the spectrum of the pristine sample in the region $150\text{-}650\text{ cm}^{-1}$ contains both the H_2O lattice band and the two H_2 rotational bands, demonstrating the presence of hydrogen gas inside the host framework. During the annealing treatment the lattice band

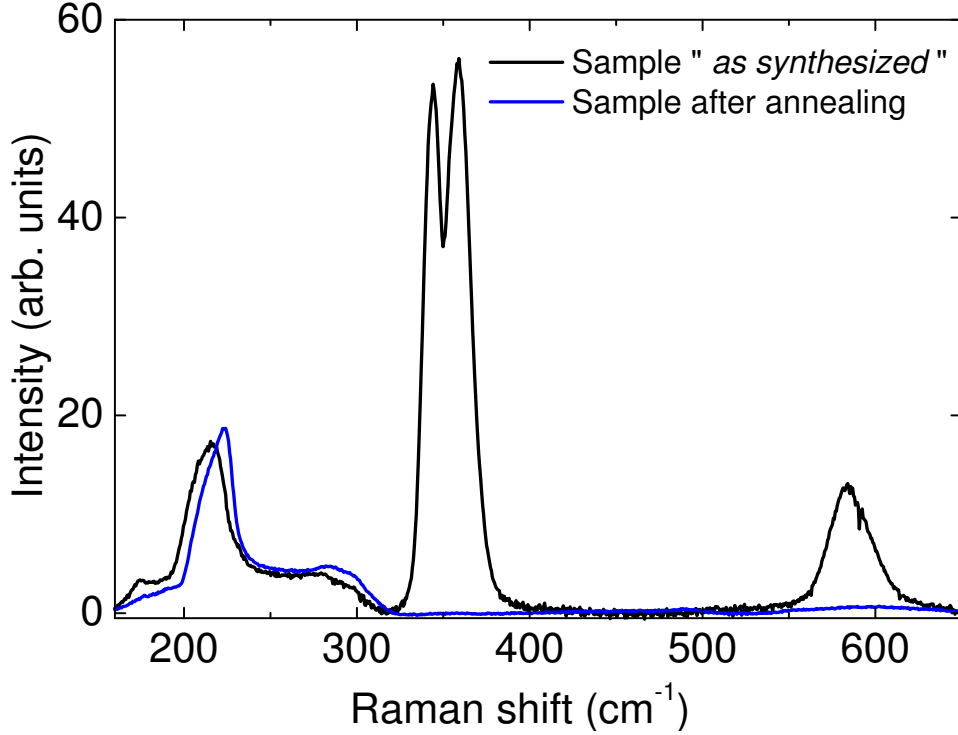


Figure 6.5: *Lattice H_2O and H_2 rotational bands in the Raman spectrum of the C_0 -structure, measured at 30 K before (black line) and after (blue line) the annealing treatment. Considering the sensitivity and the signal to noise ratio of our detection system, we can ascertain that the H_2/H_2O molar fraction in the emptied sample is less than 0.5%.*

remains practically similar to the one measured before the treatment, but a gradual decrease of the rotational band intensities is observed, up to their complete undetectability. From these data, it is possible to ascertain that there is a complete release of the hydrogen from the sample, while no evident structural phase transition occurs.

In these filled ice samples, it has been demonstrated that nitrogen molecules can be trapped as a spurious guest [5]. Probably this is due to the use of liquid nitrogen during the transfer process of the samples from the autoclave (or dewar) to the sample holder cell and for the cryo-conservation of the sample. As

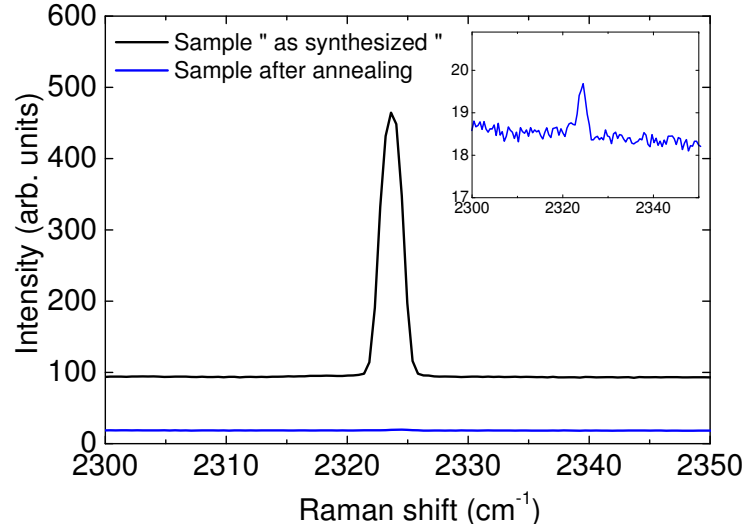


Figure 6.6: N_2 vibrational band in the Raman spectrum of the C_0 -structure, measured at 30 K before (black line) and after (blue line) the annealing treatment.

a matter of fact, the Raman spectra in the region of the N_2 vibrational mode, reported in Figure 6.6, show an evident sharp line at the frequency $2323.7 \pm 0.3 \text{ cm}^{-1}$, definitively due to nitrogen molecules. By virtue of their vibration frequency, sensibly lower than both that of N_2 gas (2329.917 cm^{-1}) [104] and that of solid N_2 in the α -phase (a doublet at 2327.5 and 2328.5 cm^{-1}) [105], it can be established that the N_2 molecules are trapped inside the structure. After the annealing process, the N_2 Raman line essentially disappears (it becomes 1000 times weaker), demonstrating a complete evacuation of the sample also by the N_2 guest impurity. These results demonstrate the metastability of the C_0 -structure even when emptied. This structure must be ascribed as a new form of ice and called *Ice XVII*, accordingly to the current nomenclature of ice polymorphisms.

Measuring at the same low temperature the host vibrational mode of the sample before and after the annealing treatment (Figure 6.7), it is possible to note an increase in the frequency of about 7 cm^{-1} for the lattice phonon band

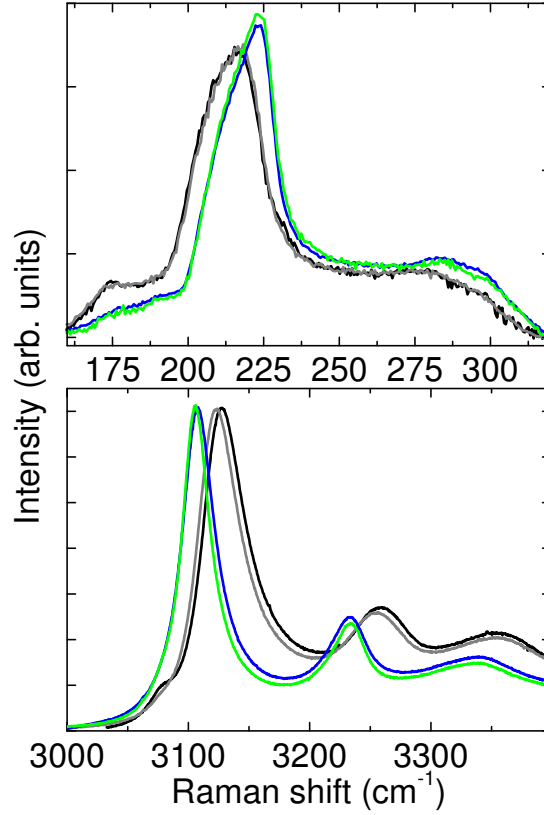


Figure 6.7: *Host vibrational modes (lattice phonon band in the upper panel and O-H stretching band in the lower panel) in the Raman spectra measured at 30 K before and after the annealing treatment on a sample in the C_0 -phase. The black and grey lines represent two different pristine samples while the blue and green lines represent empty and hydrogen refilled ice XVII, respectively.*

and a decrease of about 20 cm^{-1} for the O-H mode. The overall similarity of the band shape before and after the annealing leads us to believe that the structure of the C_0 -phase and that of ice XVII are essentially the same, while the two frequency shifts could be explained with a stronger binding and a decrease of the average O-O distance due to the absence of the guest-host interaction [106]. However, the precise nature of the effect of the annealing on the structure of the samples in the C_0 -phase will be clearer after the discussion of the neutron

diffraction data (Chapter 8). Furthermore, the increased sharpness of the spectral features measured after the annealing suggests the decrease of defects in the structure. In any case the evident spectroscopic signatures of structural modification described above are a combined effect of the removal of both H_2 and N_2 from the sample.

6.3 The porosity of ice XVII

An interesting property of ice XVII is its capability of adsorption of hydrogen molecules when exposed to this gas even at a very low pressure. The amount of hydrogen that is trapped can be deduced measuring the intensity of the rotational Raman bands (see Section 6.3.1), that is proportional to the number of adsorbed molecules. The rotational Raman spectra measured at 40 K after subsequent partial refilling steps are shown in Figure 6.8. In this case maximum gas pressure is only 250 mbar, but the rotational intensity grows higher than that in the pristine sample, which might have an unintentional heating during the transfer process from the autoclave, used for the synthesis, to the storing dewar or to the sample cell, and thus a partial release of its hydrogen content. The shape of the rotational lines does not change significantly, demonstrating that H_2 is penetrating again in the same positions in the channels as those initially occupied at the time of synthesis. Furthermore, in the case of hydrogen refilling there are no evident changes in the host vibrational bands respect to the case of empty ice XVII (green and blue lines in Figure 6.7 respectively). The difference in the spectra we have observed are large between the pristine sample and the empty ice XVII than between the empty and H_2 -refilled ice XVII. Hence we hypothesize that the substantial structural change in the sample is caused by the release of N_2 molecules during the annealing treatment, since the adsorption of H_2 guest does not seem to induce

any remarkable effect on structure.

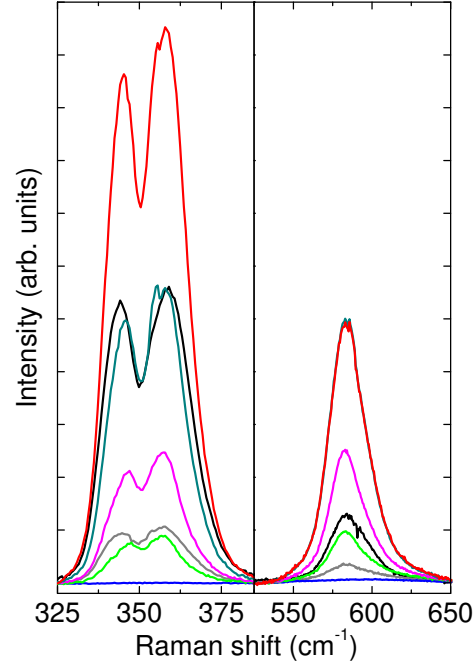


Figure 6.8: *Rotational Raman bands, measured at 40 K, in C₀-phase filled ice as synthesized (black and grey lines), ice XVII (blue lines) and H₂ refilled ice XVII (green, magenta, cyan and red lines). The intensity of the rotational bands is normalized to the intensity of the lattice phonon bands. The different hydrogen content in the two pristine samples is probably due to unintentional heating during handling.*

6.3.1 Quantitative study on hydrogen adsorption

Hydrogen molar ratio From the intensity of the Raman bands it is possible to obtain a quantitative measurement of the hydrogen content in the hydrate sample, that we express in terms of hydrogen molar fraction X , i.e. number of H₂ moles per H₂O mole. We can obtain X from the intensity ratio of the

hydrogen rotational lines I_{rot} and the lattice phonon band I_{phon}

$$X = f \frac{I_{rot}}{I_{phon}} = f \frac{\frac{I_0}{\sigma_0} + \frac{I_1}{\sigma_1}}{I_{phon}} \quad (6.1)$$

where f is a calibration factor, σ_0 and σ_1 are the Raman cross sections for the $S_0(0)$ and $S_0(1)$ rotational lines having measured intensities I_0 and I_1 , respectively. In this way, I_{rot} is proportional to the number of H_2 molecules in the lowest two $J = 0$ and $J = 1$ rotational states, that are, at low temperature, the sole rotational states with a non-negligible population. Dividing I_{rot} by the intensity of the water lattice phonon band I_{phon} , we obtain a quantity which is independent from the laser intensity and the detector efficiency, and proportional to the H_2/H_2O molar ratio in the sample. This analysis is based on the assumption that the intensities of the bands are proportional to the number of molecule giving rise to them. This is an approximation, since internal field effect and difference of the polarisability of the same molecule in different environment could produce differences in Raman line intensities. However the former introduces a correction factor that applies identically to the radiation scattered by any molecule in the hydrate, while the latter is a completely negligible contribution [64]. These will be neglected in the follow analysis.

The calibration factor f , that allows to convert the intensity ratio into hydrogen molar fraction, is calculated by fitting data arising from two independent experimental methods, that are described below. A first set of data, represented with black points in Figure 6.9, is obtained by using spectra of sII clathrates, measured in a previous work [64] in the frequency region 200-900 cm^{-1} , containing both H_2O lattice band and H_2 rotational band. For each clathrate spectrum, it is possible to calculate immediately the intensity ratio I_{rot}/I_{phon} and to estimate the hydrogen molar ratio from the intensity analysis of the Q_1 vibrational band, as described in detail in Ref. [64]. A second set of data is derived by our volumetric measurements, performed with the appa-

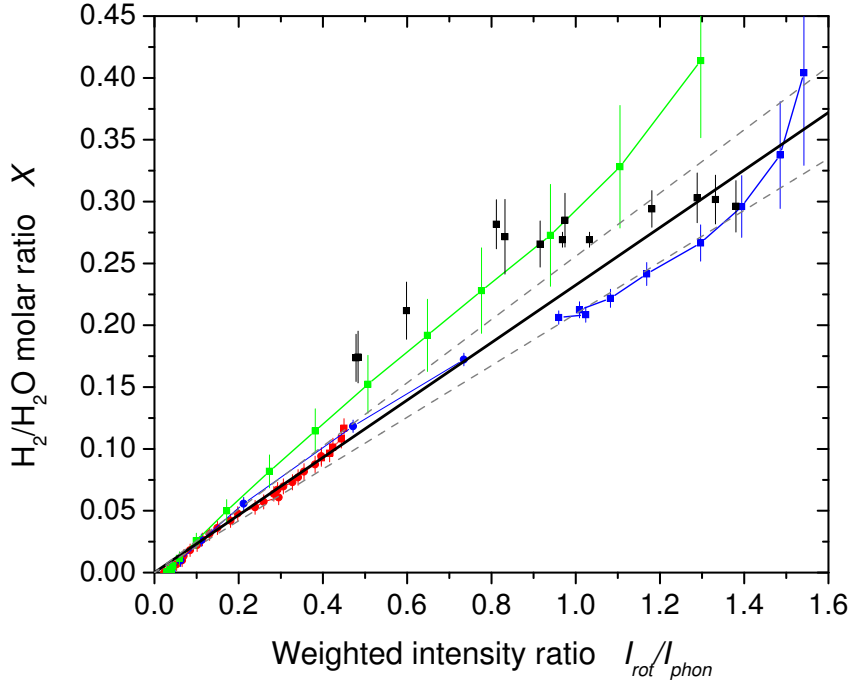


Figure 6.9: Summary of the determinations of the H_2/H_2O molar ratio plotted as a function of the concomitant measurements of the I_{rot}/I_{phon} ratio, used to determine the calibration factor f . The solid black squares represent measures of several instances of sII pure H_2 clathrate hydrates, synthesized at different pressures and/or undergone to different thermal cycles [64], while the other points are volumetric measurements performed in this work during the measurements of the 20, 50 and 80 K isotherms (red, green and blue respectively). Different symbols (solid dots or squares) indicate the use of a different standard volume and/or a different transducer. The solid and dashed black line is the linear fit through zero and the confidence interval respectively. The estimated uncertainty on these experimental points depends critically on the precision of the different calibrated volumes and pressure transducers used and on the pressure of the measurement.

tus connected to the Raman optical cell, of the amount of gas adsorbed during refilling of the sample at three different temperatures, namely 20, 50 and 80 K (red, green and blue points of Figure 6.9). For each H₂-refilled ice XVII spectrum in the frequency region 150-650 cm⁻¹, the intensity ratio I_{rot}/I_{phon} is calculated as described above, while the corresponding amount of hydrogen after a given gas insertion is estimated as follows. Denoting with N_{H_2} the number of moles of hydrogen adsorbed by the sample and with N_{H_2O} the number of water moles of the sample, the H₂/H₂O molar ratio of the sample after an insertion of gas in the cell is given by

$$X = \frac{N_{H_2}}{N_{H_2O}} = N_{H_2} \frac{m}{M} \quad (6.2)$$

where m is molar mass of water and M is the measured mass of the empty sample. The value of N_{H_2} is obtained by means of the equation of state for an ideal gas, measuring the pressure in the cell before and after the insertion of a given number of hydrogen moles contained in the gauge volume (see Section 4.2), since all volumes of the gas insertion circuit are known. The cumulative linear fit of the two independent set of data just described above gives a calibration factor $f = 0.233 \pm 0.023$, that is the value used in this work.

The C₀-phase filled ice samples examined just after the synthesis, whose typical rotational spectrum is reported with the black line in Figure 6.8, are characterized by $X \simeq 25\%$, while for the refilled ice XVII in some instances, as for the most intense spectrum shown with the red line in Figure 6.8, the measured X value exceeds 40 %, reaching higher values than the established theoretical maximum for sII clathrates $48/136 \simeq 35\%$. The lower hydrogen content in the pristine samples compared to the refilled ones can be ascribed to the initial presence of nitrogen molecules in the sample that partially fill the channel structure, as well as to unwanted heating of the sample during the loading of Raman optical cell.

Adsorption isotherms Deriving the amount of adsorbed H₂ as a function of pressure, we have measured several adsorption isotherms at six different temperatures between 15 to 80 K. The results are reported in Figure 6.10. Pressure is increased gradually and, when possible, each measurement is taken after the same delay Δt , indicated in each panel, from each pressure increase step. The pressure at which saturation is reached is strongly dependent on temperature and ranges between a few millibar at 15 K to several bar at 80 K. Also the maximum value of the measured adsorption is strongly temperature-dependent because it depends on the kinetics of hydrogen diffusion. By using the same method, we examined the gas desorption while releasing pressure (red points in Figure 6.10). A large hysteresis and other kinetic effects are evident at the lower temperatures. As it is shown in the upper panels of Figure 6.10, at 15 K and 20 K, after decreasing pressure down to zero, the sample does not sensibly release hydrogen in $\Delta t = 10$ min. The same effect is observed at 40 K, the filling remaining almost constant for about 1 h. At this temperature, the increase in the adsorbed gas observed at about 240 mbar, after a 16.5 hour long exposure to hydrogen, indicates that at least two time scales dominate the phenomenon: one fast adsorption in the outermost sites of the channels and a slower one, limited by molecular diffusion inside the channels. At higher temperatures, 50, 65 and 80 K, a very small hysteresis it is observed, indicating that the time needed to hydrogen to diffuse for distance of the order of the linear dimension of the sample grains is quite shorter than the time interval between measurements. At temperature above 50 K, the desorption process is faster, even if it is compared to sII clathrates [7]. This is not surprising at all, since the channels in ice XVII are much wider than the free space inside both the 6-membered and 5-membered rings that constitute the polyhedral cavity faces of clathrates.

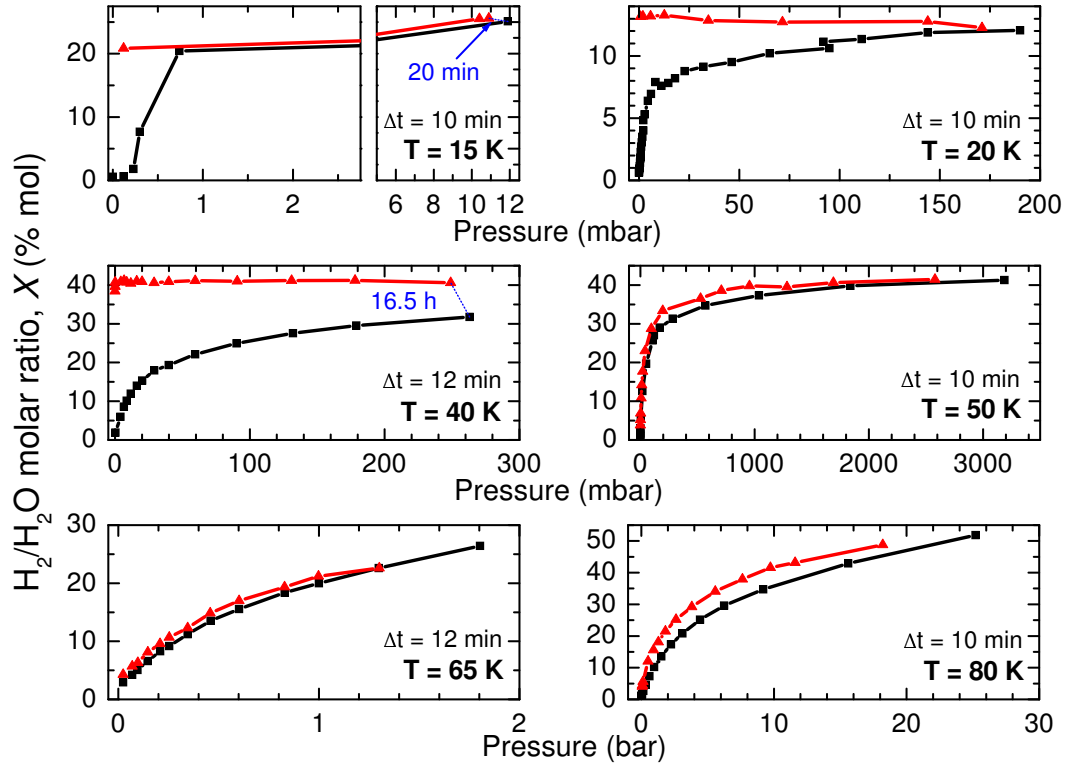


Figure 6.10: *Hydrogen molar fraction X measured while increasing (black square symbols) and decreasing (red triangular symbols) hydrogen pressure in ice XVII. Due to calibration, X has a systematic uncertainty of $\pm 10\%$. The time lag between pressure increase in the cell and Raman measurement in the same series (same symbol) is indicated as Δt in each panel, while a thin dotted blue line joins measurements performed with larger delays.*

Enthalpy of adsorption In order to study the mechanism of adsorption in a porous material, it can be useful to estimate its enthalpy of adsorption. For a given hydrogen uptake X the enthalpy of adsorption Δh is obtained by means of Van't Hoff equation

$$\frac{\Delta h}{R} = \left[\frac{d \ln \left(\frac{p}{p_0} \right)}{d \frac{1}{T}} \right]_X \quad (6.3)$$

where R is the gas constant. For the calculation of the temperature derivative, adsorption isotherms at different temperatures are necessary. We have used those measured at 50, 65 and 80 K, estimating the temperature derivative with a straight line fit. As shown in Figure 6.11, the resulting value of $-\Delta h$

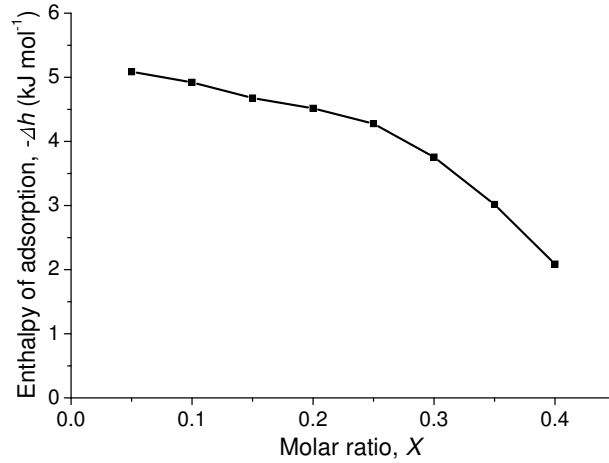


Figure 6.11: *Enthalpy of adsorption in function of H_2/H_2O molar ratio X . The values are calculated using data collected at 50, 65 and 80 K.*

decrease with increasing molar ratio X starting from about 5 kJ/mol at $X \simeq 10\%$ down to about 2 kJ/mol at $X \simeq 40\%$. Values in these range are typical for molecular physisorption in porous material like MOF [107], whose mechanism of hydrogen adsorption is similar to that in ice XVII and, being driven by van der Waals interactions, does not involve any chemical bound. The decreasing behaviour of the enthalpy with increasing hydrogen content could suggest the presence of different adsorption sites, for example with different binding energy to molecules placed deep into the channels with respect to those at the entrance of the channels, or even a cooperative effect of the already adsorbed hydrogen molecules on extra adsorbed ones. Moreover possible structural changes during the entire filling process could induce the enthalpy behaviour observed above.

6.3.2 Ortho-para conversion

It is well known that, for a H_2 molecule, the correlation between nuclear spin state and rotational state implies the existence of two species of hydrogen molecule, as already described in Section 5.3. The molecule can be found either in the state of ortho-hydrogen (o-H_2), characterized by parallel nuclear spins and odd rotational quantum number J , or in the state of para-hydrogen (p-H_2), characterized by antiparallel nuclear spins and even rotational quantum number J . The concentration of the ortho and para species at thermodynamic equilibrium is obtained by means of the partition functions according to the relation:

$$X_{o,p} = \frac{Z_{o,p}}{Z} = \frac{\sum_{J=\text{odd,even}}^{\infty} g_J (2J+1) e^{-\frac{E_J}{k_B T}}}{\sum_{J=0}^{\infty} g_J (2J+1) e^{-\frac{E_J}{k_B T}}} , \quad (6.4)$$

where g_J is the degeneracy of the rotational level, with quantum number J and energy E_J , relative to the total nuclear spin projection; this coefficient is 3 in the case of odd J (ortho-hydrogen), while is 1 in the case of even J (para-hydrogen). At room temperature the equilibrium concentration of o-H_2 is about three times the concentration of p-H_2 , using in this case the wording of hydrogen normal mixture (n-H_2).

It is well known that the ortho-para conversion of one H_2 molecule is induced by a non-zero magnetic moment of a nearby molecule. In pure H_2 , either gas, solid or liquid, there is a mechanism of ortho-para conversion, called intrinsic, but it has a very slow kinetics, and the H_2 molecular system may be considered a mixture of the two species for long time. The conversion is due to the interaction of one ortho- H_2 with other hydrogen molecules having non-zero magnetic moment. Only the ortho specie, however, has a non-zero magnetic moment. The conversion rate in this case would be proportional to the square

of the ortho fraction, namely

$$\frac{d}{dt}x(t) = -K \frac{x(t)(x(t) - x_e)}{1 - x_e}, \quad (6.5)$$

where x_e is the equilibrium value of $x(t)$ at T , K is the ortho-para intrinsic conversion constant. In the hypothesis that the temperature is low enough to neglect x_e , the solution of Eq. 6.5 is given by

$$x(t) = \frac{x(0)}{1 + x(0)Kt}. \quad (6.6)$$

If foreign molecules, with appropriate magnetic properties, are present, these may act as catalyst and can speed up the conversion, which is called extrinsic in this case. The rate of conversion of an o-H₂ at constant temperature T will be proportional to the number of o-H₂ molecules $x(t)$ and it can be described by

$$\frac{d}{dt}x(t) = -H \frac{x(t) - x_e}{1 - x_e}, \quad (6.7)$$

where H is the ortho-para extrinsic conversion constant. In the hypothesis that the temperature is low enough to neglect x_e , the solution for $x(t)$ is an exponential law, namely

$$x(t) = x(0)e^{-Ht}. \quad (6.8)$$

In the past the ortho-para conversion was efficiently studied in hydrogen clathrate systems with Raman spectroscopy, monitoring the intensity ratio between ortho and para vibrational components [64], and both type of conversion were taken into account to explain the observed conversion rate. The solution of a kinetic equation, containing both intrinsic and extrinsic terms, i.e.

$$\frac{d}{dt}x(t) = -K \frac{x(t)(x(t) - x_e)}{1 - x_e} - H \frac{x(t) - x_e}{1 - x_e}, \quad (6.9)$$

in the hypothesis of neglecting x_e , is provided by

$$x(t) = \frac{x(0)H}{x(0)K(e^{Ht} - 1) + He^{Ht}}. \quad (6.10)$$

In order to study the ortho-para conversion in filled ice, an ice XVII sample at 11 K is refilled with normal hydrogen. Its conversion kinetics is obtained measuring the Raman intensity of the $S_0(0)$ and $S_0(1)$ rotational lines as function of time and at constant temperature for almost 200 hours. From the integrated intensity I_0 and I_1 of the rotational lines, the o-H₂ fraction is calculated from the relation

$$x(t) = \frac{\frac{I_1(t)}{\sigma_1}}{\frac{I_0(t)}{\sigma_0} + \frac{I_1(t)}{\sigma_1}}, \quad (6.11)$$

where time $t = 0$ is arbitrary and correspond to the time of complete adsorption of hydrogen gas by the sample. This experimental data are fitted with different conversion models, i.e. intrinsic or extrinsic, where x_e is neglected due to low temperature of the experiment. The best fit is obtained considering both intrinsic and extrinsic conversion, and using Eq. 6.10, with $x(0)$, H and K as fit parameters. The results are reported in Figure 6.12. The value of the extrinsic conversion constant, $H = 0.0047 \pm 0.0002 \text{ h}^{-1}$, is quite similar to that measured for sII hydrogen clathrate (0.00474 h^{-1} [64]), demonstrating in both case a similar interaction of the guest H₂ molecule with the host H₂O environment. The value of the intrinsic constant ($K = 0.0135 \pm 0.0005 \text{ h}^{-1}$) is much higher than that obtained for H₂ molecules in the large cage of clathrate system (about 0.0025 h^{-1} [64]). This faster conversion rate demonstrate a stronger interaction between hydrogen molecules inside the filled ice. Considering the Ref. [108], this K value, once it is normalized to the number of nearest neighbour molecules, corresponds to an intermolecular distance ranging between 2.4 and 2.5 Å, that is quite similar with what expected from potential energy calculation for the proposed P3₁12 space group for C₀-structure (see Section 8.4).

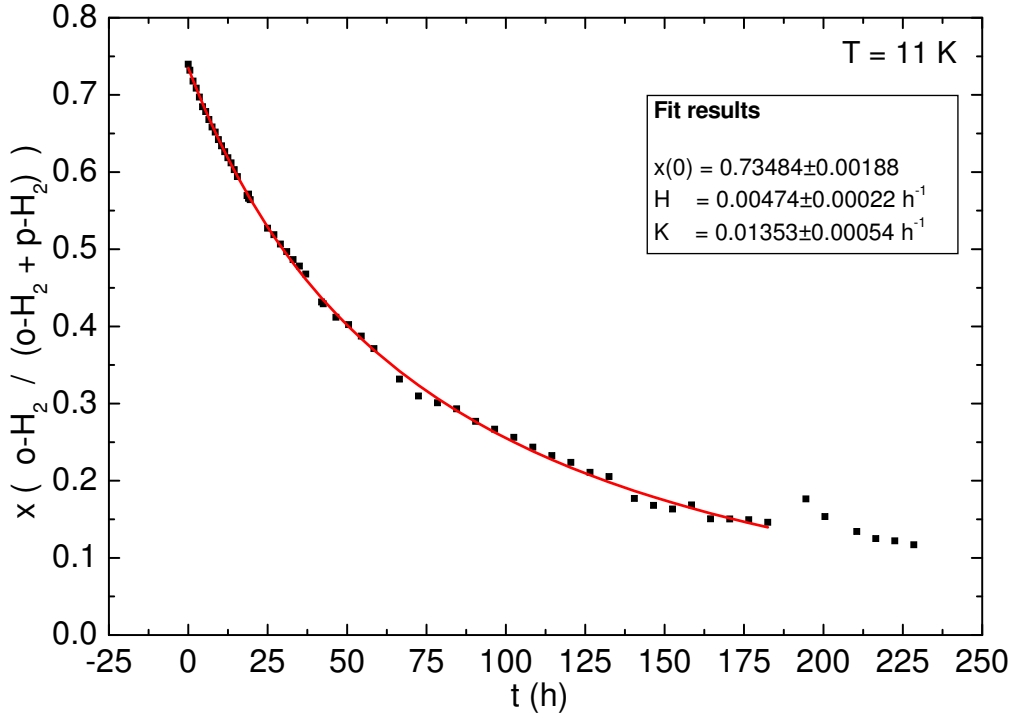


Figure 6.12: *Measurement of the ortho- H_2 fraction as a function of time, represented with black squares. The fit curve, obtained by using equation 6.10, is represented with red line. The data after 182.5 h are excluded from the fitting interval because the sample has undergone an unwanted heating. The value of $x(0)$ is obtained from the fit and is about what it is expected for normal hydrogen.*

6.3.3 Metastability of ice XVII

For describing the limits of the metastability region for the C₀-structure filled ice and H₂-refilled ice XVII, it can be useful to study the amount of hydrogen trapped in the samples as a function of increasing temperature. We have performed this analysis on one pristine sample and for two samples of the refilled ice XVII. As it is shown in Figure 6.13, the C₀-structure filled ice seems to have a wider stability region, considering that it starts to loose hydrogen at a temperature higher than 75 K and reaches an almost complete evacuation at

120 K. The annealed samples, even with different initial filling, show a narrower stability region. In this case, the release of hydrogen gas starts at about 40 K and the complete emptying is reached at about 100 K. Even if this study of the stability region is non quantitative, it is clear that the filled ice directly quenched in liquid nitrogen after synthesis has a higher capacity of keeping the hydrogen guest trapped. This is probably due to impurities of nitrogen molecules present in the pristine crystal, or to structural defects that hinder the diffusive motion of the hydrogen molecules along the channels present in the structure.

A further increase of the temperature has lead the complete decomposition of ice XVII at 130 K with a relatively fast kinetics (about one hour). The resulting phase is probably ice *Ih*, according to the H₂O molecule Raman lattice and O–H stretching bands, even if only diffraction data on this resulting structure would allow a clear determination of its crystal symmetry.

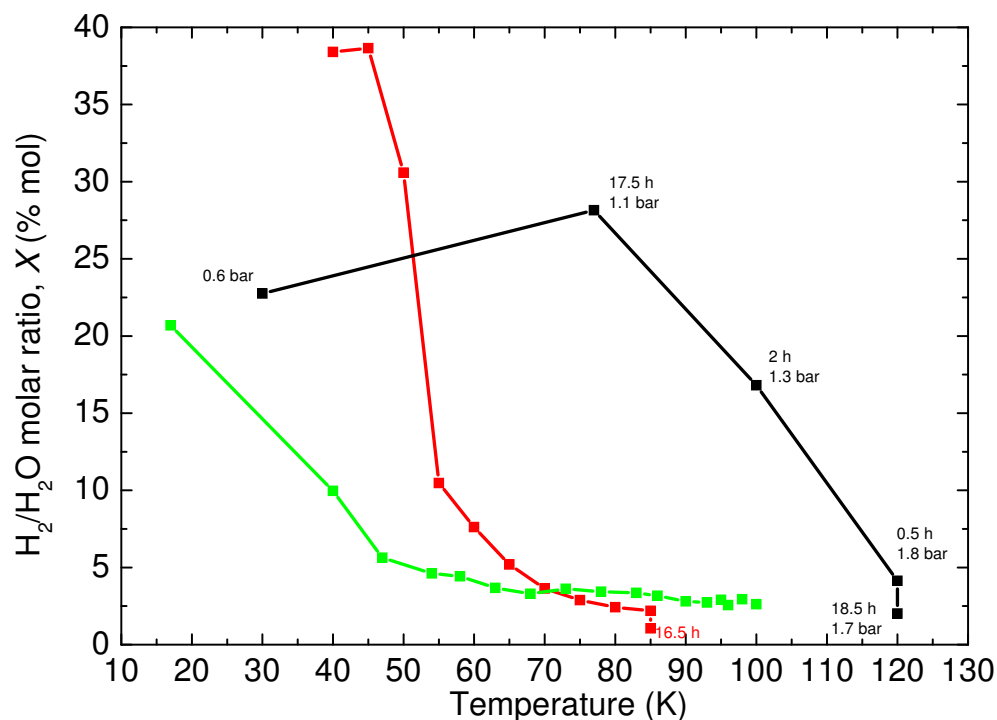


Figure 6.13: *Hydrogen molar fraction as a function of increasing temperature in a C_0 -structure filled ice as synthesized (black line), and hydrogen refilled ice XVII with different initial hydrogen content (red and green lines). The pristine sample is kept at standard pressure, while the others are under vacuum. The delay between two consecutive measurements are indicated in the figure for the black series, while it is 5 and 2 minutes for the red and green series respectively.*

Chapter 7

Neutron spectroscopy on ice XVII

In order to study the vibrational dynamics of the hydrogen molecule in the C_0 -structure, we have performed a series of neutron scattering measurements on a $D_2O - H_2$ sample by means of the high-resolution TOSCA spectrometer (ISIS-RAL, U.K.). The sample has been produced at ISC-CNR laboratories, using the standardized procedure described in the previous Section 4.2, and inserted in several vials stored in a cryogenic dewar suitable for air shipping. The sample, having the form of a fine powder, is transferred at liquid nitrogen temperature from the vials to the sample cell. Once the cell has been attached to the center-stick, it is placed inside the TOSCA cryostat, having care to avoid any heating of the cell during this transfer. All the spectra have been measured at a temperature of 15 K to minimize the contribution of the Debye-Waller factor to the neutron scattering cross-section, and each acquisition has been 6-8 h long, corresponding to an integrated current of about $10^3 \mu Ah$, in order to accumulate a good amount of counts and obtain a high signal to noise ratio. Due to the neutron scattering cross section value of the selected host molecules, in these spectra the scattering from the protons of the guest is predominant, as it will appear evident from the results presented below.

The experimental data, collected by each detector as a function of neu-

tron time-of-flight, are transformed into energy-transfer (E) spectra, making use of the standard routines available on the spectrometer control computer. This routine takes into account also the kinematic factor k'/k and normalizes the data to the incoming neutron flux. Data belonging to different detectors are added together producing two distinct data blocks: one contains the data recorded by the backscattering detectors and the other contains the data recorded by the forward-scattering ones. This procedure is justified by the narrow angular-range spanned by each set of detectors.

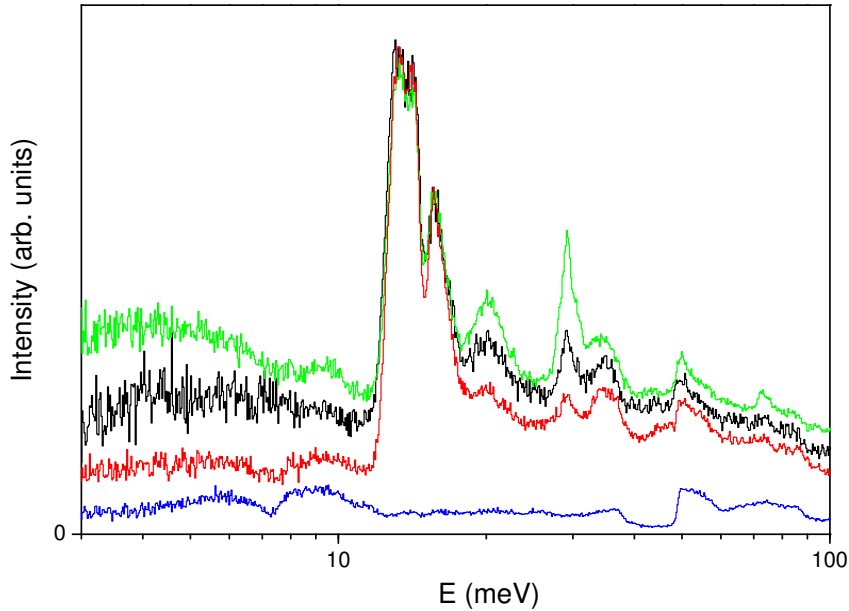


Figure 7.1: *Neutron scattering spectra of C_0 -structure filled ice ($D_2O + H_2$), measured at 15 K on the TOSCA spectrometer, after summation of the data from backward and forward detector banks. The spectrum of the pristine sample is reported with a black line, the spectrum of the empty C_0 -phase (ice XVII) is reported with a blue line, while the spectra of the refilled sample with ortho-rich and para-rich hydrogen gas are reported with a green and a red line, respectively.*

First of all, the spectrum of the pristine sample (i.e. before any thermal treatment) is measured. This is reported with the black line in Figure 7.1.

The spectrum shows the presence of several narrow and intense bands due to molecular hydrogen dynamics, that is the dominant contribution, if compared to the spectrum of the deuterated ice skeleton (see later). In view of the subsequent measurements, the pristine sample is submitted to the annealing treatment (as already described in detail in Section 6.2), by keeping it under vacuum at temperature of 110 K for 1.5 h. During this treatment we have monitored the gas released from the sample by measuring the pressure in a buffer volume, consisting of four bottles, connected to the sample cell. In this way the complete evacuation of the pristine sample is achieved, hence obtaining D₂O ice XVII. The spectrum of heavy ice XVII is recorded at 15 K and it is reported with the blue line in Figure 7.1. Due to the much lower neutron cross section of deuterium compared to that of hydrogen, this spectrum is much less intense than the previous one. It presents a lower number of sharp bands, since it represents only the vibrational dynamics of the host lattice. Subsequently, the spectrum of the ice XVII sample, refilled with an ortho-rich mixture of hydrogen gas, is measured (green line in Figure 7.1). After a further annealing treatment, similar to that described above, and a refill with a para-rich hydrogen mixture, produced by means of a catalyst connected to the gas circuit, the fourth spectrum of this series is collected (red line in Figure 7.1). The two latest spectra seem to have an overall similar shape, even if it is evident that the low energy band below 10 meV has a different intensity in the case of the ortho-rich and para-rich guest, and the features at energies of 20 meV or higher are more intense in the ortho-rich case. The intermediate position of the spectrum of the pristine sample (black line of Figure 7.1) compared to the refilled ones reported in the same plot is consistent with about 50 % concentration of ortho and para hydrogen species in the pristine sample, due to the long time of storing of the sample at liquid nitrogen temperature (77 K).

7.1 Lattice vibrational modes in ice XVII

Incoherent inelastic neutron scattering (IINS) can be used to study the phonon spectrum of the ice XVII itself since it has been shown that the incoherent neutron scattering cross section is related directly to phonon density of states (PDoS) [92]. The spectrum of D_2O ice XVII is reported again in Figure 7.2 with a different scale for a better visualization. It is useful remembering that in

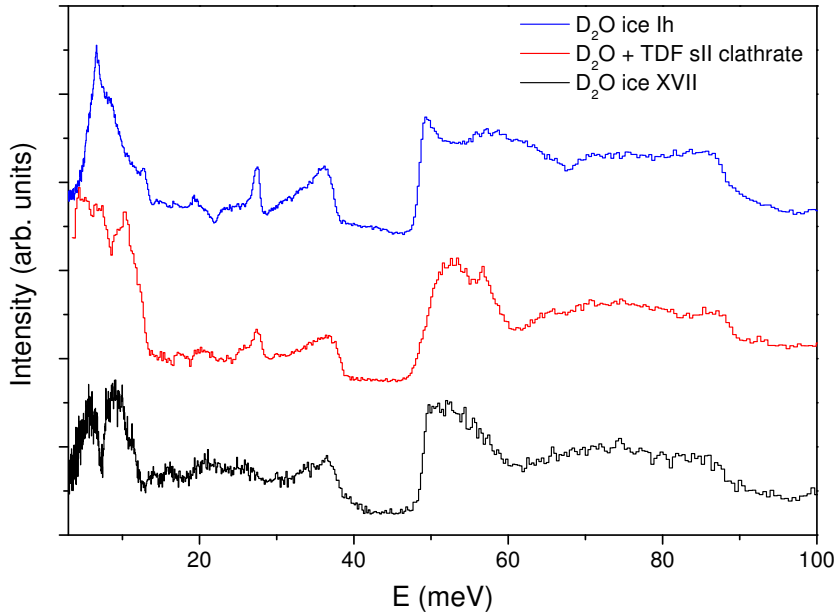


Figure 7.2: *Neutron scattering spectrum of D_2O ice XVII (black line), D_2O+TDF sII clathrate [109] (red line) and D_2O ice Ih [110] (blue line) measured at 15 K on TOSCA spectrometer. In the figure are reported only the data collected with backward detector bank.*

hydrogen containing samples, the coherent scattering contributions are much less important than the incoherent ones, and the incoherent approximation is valid. On the contrary, the resulting spectra for deuterated samples, like in this case of study, are less accurate than hydrogenated one for reproducing the incoherent dynamics, even if a qualitative analysis is still possible [111].

Anyway, by comparing this spectrum with the experimental ones of the three clathrate structures, reported in ref. [109], a strong overall similarity can be noted, maybe more pronounced than that found with ice *Ih* [110]. The acoustic and optical phonon bands are characterized by a quite intense double peak at about 7 meV and by weaker features between 10 and 40 meV. It is evident that their shapes are quite similar to the same band in D₂O sII clathrate. In the librational region ($50 \text{ meV} < E < 100 \text{ meV}$), we can note stronger differences compared to clathrate and ice *Ih* case. In particular, the first steep rise, located at about 50 meV, appears very sharp in ice XVII, while the dip around 60 meV is less pronounced in the ice XVII than in the sII clathrate case.

Anyway, the intensity of the librational band is comparable to that of the lattice band, in similar way to what happens in ice *Ih*, but in contrast to what happens in clathrates. Probably this effect may be attributed to the presence of the guest molecules in the structure. Indeed it is necessary to remember that in the clathrate case the guest, even if deuterated, gives a small, but not null, contribution in the incoherent spectrum and it could also introduce some modification in ice vibrational spectra due to guest-host interaction. A better comparison between emptied inclusion compounds should be done with a completely emptied clathrate structure, i.e. ice XVI [7], but INS spectra of this ice phase have never been measured.

A quantitative interpretation of the features observed in these spectra would require a comparison with reliable lattice dynamic computation. Commonly used intermolecular potential models do not allow a quantitative reproduction of these features.

7.2 The hydrogen dynamics in refilled ice XVII

The spectra due only to the hydrogen molecules in the sample refilled with para-rich and ortho-rich mixture of hydrogen species are reported in Figure 7.3 with red and green lines, respectively. The hydrogen contribution is obtained by subtraction of the reference spectrum (empty D₂O ice XVII) described above. These spectra show the presence of several narrow and intense bands due to molecular hydrogen dynamics. In analogy with the spectra of sII hydrogen clathrate [91], it is possible to interpret the observed bands (in order of increasing energy transfer) as being due to the translational motion of the c.m. of the hydrogen molecule inside the channel-like arranged water skeleton ($E < 10$ meV), to the molecular rotation ($E \cong 15$ meV for p-H₂ and $E \cong 30$ meV for o-H₂), and to their combinations. In the hypothesis of neglecting the coherent part of the scattering and decoupling the internal motions of the molecule from the molecule c.m. translation, the observed spectrum could be described by the self part of the double differential neutron scattering cross section as written in Eq. 5.43. At these low temperatures, only the lowest rotational states ($J = 0, 1$) are populated, and only few transitions contribute to the spectrum in the low energy region, that are the rotationally elastic $J = 1 \rightarrow 1$ and the inelastic $J = 1 \rightarrow 2$ transitions of ortho-H₂, and the inelastic $J = 0 \rightarrow 1$ of para-H₂, while the $J = 0 \rightarrow 0$ transition of the para-H₂ molecule does not contribute appreciably to the spectrum, since the intensity of the *even* \rightarrow *even* rotational transitions are weighted by the coherent cross section. This expected scenario seems to be fully confirmed by the measured spectra, in which the observed broad band at energies $E < 10$ meV, present in the ortho-rich hydrogen sample, is almost absent in the para-rich one. Furthermore comparing the spectra of the ortho-rich and para-rich samples, it is evident that the intensity ratio of the two bands at $E < 10$ meV and $E \cong 15$ meV is lower in the para-rich sample. This confirms that the first band

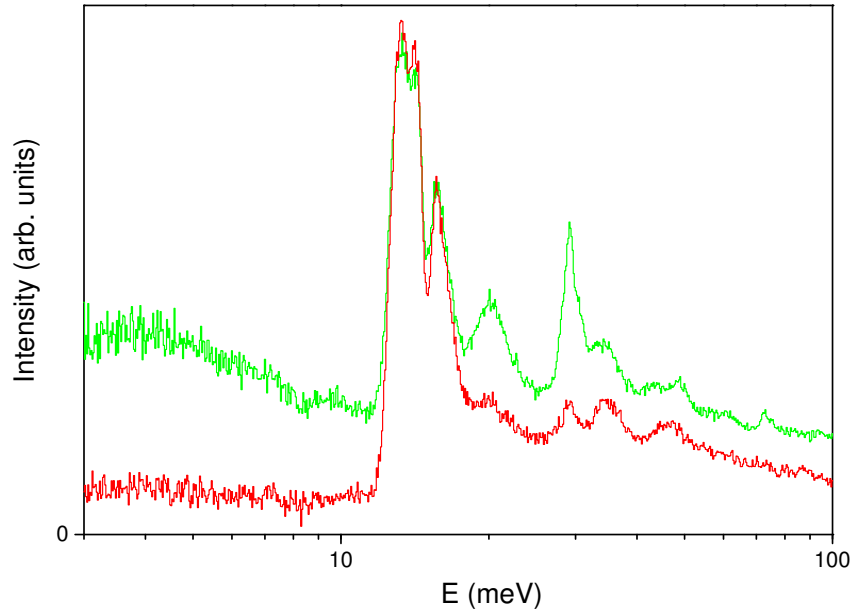


Figure 7.3: Neutron scattering spectra of C_0 -structure filled ice (D_2O ice XVII refilled with H_2) after the subtraction of the reference sample (empty D_2O ice XVII and aluminium sample container). The spectra of the sample refilled with para-rich and ortho-rich hydrogen are reported with red and green lines, respectively.

($E < 10$ meV) is due to ortho- H_2 and it is the result of the combination of the elastic $J = 1 \rightarrow 1$ rotational transition with that related to the c.m. translational motion, the second band ($E \cong 15$ meV) to para- H_2 , being the inelastic $J = 0 \rightarrow 1$ rotational transition, while the narrow band placed at about 30 meV is due to inelastic $J = 1 \rightarrow 2$ rotational transition in ortho- H_2 . These last two bands are split in more than one component, testifying the anisotropy of the potential energy with respect to the orientation of the hydrogen molecule. For what concern the first band, in the filled ice sample, it seems to have a smooth shape and is quite broad, compared to the narrow and well distinct line of the fundamental quantum rattling mode, originated by the translational motion of the hydrogen molecule c.m., present in the sII clathrate. This fact

could be explained taking into account the shallow potential barrier between two equilibrium positions for the H_2 molecule inside the channel (see Section 8.4).

Therefore, for more accurate interpretation of these spectra, it could be useful to extract the pure ortho and para hydrogen spectrum for a direct comparison. The extraction procedure is straightforward if we assume, as we have largely justified before, that two well distinct spectral features, located in two different spectral regions, arise only from molecules of one single specie, either para- H_2 or ortho- H_2 . This is the case for the $J = 0 \rightarrow 1$ band, at $E \simeq 15$ meV (para- H_2), and for the c.m. translational band combined with the $J = 1 \rightarrow 1$ elastic transition (ortho- H_2). The pure para- H_2 spectrum is then obtained subtracting, from the spectrum obtained for the para-rich sample, the spectrum of the ortho-rich sample, weighted by a factor such as to obtain almost null intensity in the region $E \simeq 10$ meV. An analogous linear combination of the ortho-rich and para-rich spectra, adjusted to minimize the rotational line at $E \simeq 15$ meV with respect to a smooth background, gives as results the spectrum of pure ortho- H_2 .

The resulting pure para- and ortho- H_2 spectra, obtained by the subtraction described above, are reported in Figure 7.4. It is interesting to note that two features present in the pure ortho- H_2 spectrum, namely the peak placed at about 20 meV and the shoulders of the rotational $J = 1 \rightarrow 2$ peak at about 30 meV, are also present in the para- H_2 spectrum, but shifted of about 15 meV, that is, combined with the $J = 0 \rightarrow 1$ transition. In particular, comparing the pure ortho- H_2 spectrum with the downshifted para- H_2 one (see the inset in Figure 7.4), their resemblance is quite evident. Thus the two bands around $E \simeq 20$ meV and $E \simeq 30$ meV, together with the broader one at lower energies, have to be assigned to the translational motion of the H_2 c.m.. Their spectral characteristics can be explained taking into account the peculiar interaction

potential that hydrogen guests experience in the water channel framework of the C_0 -structure.

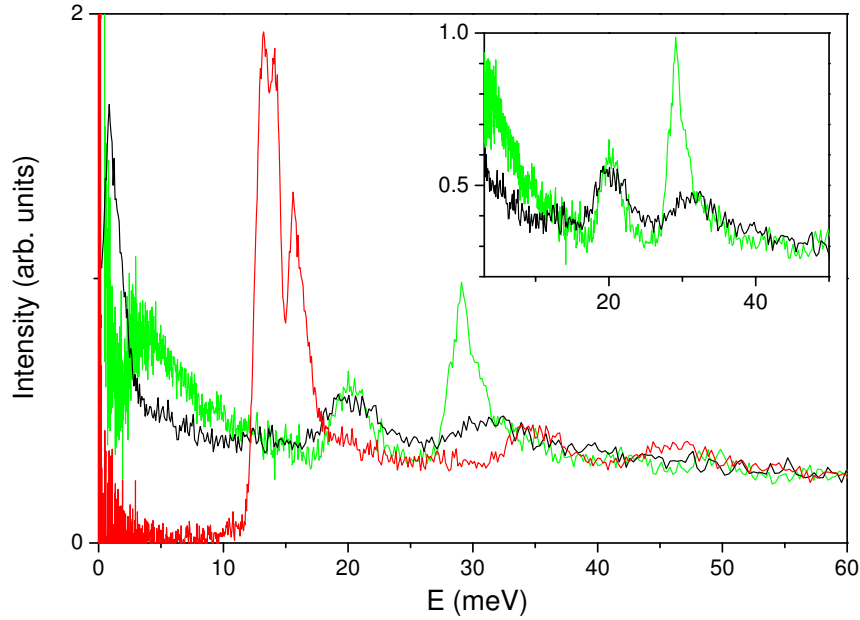


Figure 7.4: *Neutron scattering spectra of C_0 -structure filled ice (D_2O ice XVII refilled with H_2) after the subtraction of the reference sample (empty D_2O ice XVII and aluminium sample container). The pure para- H_2 and pure orto- H_2 spectra are reported with the red and green line. For facilitate the comparison, in the figure we have also reported with the black line the pure para- H_2 spectrum normalized with an arbitrary factor and shifted of 14.75 meV toward lower energy. In the inset the green and black spectra are reported with different scale.*

It would be interesting to reproduce these bands by a calculation of the c.m. motion of H_2 in ice XVII (analogously with what has been done for sII clathrate), but this would require to consider a realistic quantum dynamics of the c.m. motion, harder to compute than in sII clathrate, because of the breakdown of the single molecule model. This analysis is beyond the scope of the present work.

Chapter 8

Experimental results on structure

Just after the synthesis of the samples, we have performed a rapid structural check by means of X-rays diffraction, which has confirmed that the solid mixture produced by us is effectively hydrogen filled ice in the C_0 -phase. Anyway, since we have also claimed a new form of water crystalline structure, it has been necessary to perform a complete set of neutron diffraction measurements, not only on the ice XVII sample, but also on the pristine one, namely C_0 -phase. In both case a study of the dependence of the lattice cell parameters by the hydrogen content has been addressed and it will be illustrated in the next sections.

8.1 Preliminary X-rays structural check of pristine sample

The structure of some samples in the C_0 -phase (H_2 - H_2O) is examined by the X-rays diffractometer (four circle Oxford Diffraction XcaliburPX) present at the CRIST laboratory of the University of Florence. The recorded data show that the analysed samples present a considerable texture, which prevents a Rietveld analysis, but the measured diffraction pattern can be used to

discriminate among several proposed structures by fitting them with Le Bail method. The best fit is obtained assuming the C_0 -II structure (space group $P3_112$) [3, 5] and is reported in Figure 8.1. The other structures actually proposed in the literature, namely sT' ($P4_2/mnm$) [5], ice II ($R\bar{3}$) [51], Ih - C_0 (Cc) [112] and ice Ic ($Fd\bar{3}m$) [113], would give diffraction patterns in evident disagreement with the experimental one. This preliminary structural check allows us to assert with reasonable certainty that the sample produced by the procedure described in Section 3.2 is actually a filled ice in the C_0 -phase. Anyway, these data do not allow the determination of filled ice structure unambiguously due to the very small X-rays cross section of hydrogen atom respect to oxygen one (see Figure 5.1). Indeed, as for whatever ice structure, neutron diffraction, together with isotopic substitution ($H \leftrightarrow D$), is a more reliable method for a complete refinement of ice structures.

8.2 Structure refinement of ice XVII

A neutron diffraction experiment on OSIRIS at ISIS (RAL, UK) has been performed in order to determine and refine the structure of this new form of ice (XVII), whose existence was unknown before the Raman measurements described in the previous section. We have chosen OSIRIS instrument because it is also a spectrometer for study the diffusive motion of hydrogen molecule inside the C_0 -structure. Anyway, the description of the last quasi-elastic measurements is beyond the aim of this work.

A small amount of powdered H_2 - D_2O filled ice in the C_0 -phase, synthesized following the procedure described in Section 3.2 and recovered at liquid nitrogen temperature, is inserted in an aluminium annular cell. A fast check of a portion of the same recovered sample, performed by means of Raman spectroscopy, allows to rule out the contamination by sII hydrogen clathrate

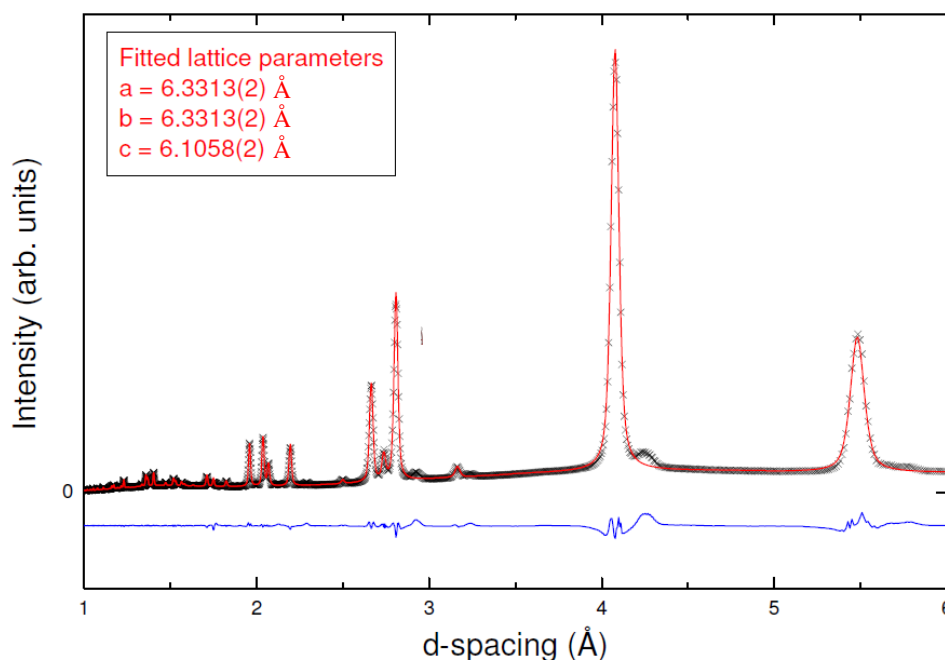


Figure 8.1: *Experimental x-ray diffraction pattern measured at ambient pressure (black crosses). The capillary is maintained at low temperature (about 90-100 K) by a Oxford Cryostream system. Diffractograms are collected using a copper X-rays source (Cu- $K\alpha$ radiation), and recorded by a 165 mm diameter CCD detector. Total collection time is of the order of 7 minutes. The red line represents the fit, performed by using Le Bail method, to the experimental data assuming the C_0 -II structure (space group $P3_112$) [3]. The value of the lattice parameters obtained from the fit procedure are reported in the figure. The blue curve is the difference between the experimental pattern and the fit.*

or other spurious ice phases. Due to the large coherent scattering cross section of deuterium atoms, the heavy water serves perfectly for the refinement of the ice XVII structure, while the use of hydrogenated guest prevents the position refinement of the guest molecule inside the filled ice structure. After a few measurements on the pristine sample in the C_0 -phase at increasing temper-

ature, the sample is subjected to an annealing treatment, heating to 100 K under vacuum for a few hours, in order to obtain ice XVII. This process assures the removal of the guest H_2 molecules as well as nitrogen molecules that are often present in the sample when prepared with the procedure described in Section 3.2. Since for this structure no Bragg reflection is present at d -spacing higher than 5.5 \AA , the collection of a complete experimental diffraction pattern requires the acquisition of five different diffractograms, obtained by using subsequently five different chopper settings, conventionally named d1-d5 on OSIRIS. Due to the high counting rate, a whole collection is completed in less than 1 h. The complete experimental pattern of ice XVII is measured at three temperatures, namely 100, 75 and 25 K. The data are reported in Figure 8.2. Full range diffraction patterns, expressed as a function of d -spacing, are analysed by Rietveld refinement using the software GSAS [114]. Preliminarily, in order to obtain a reliable profile fit function and other instrumental parameters, a Rietveld refinement is performed on a NaCaAlF diffraction pattern, measured a shortly before this experiment and available in the instrument data base, obtaining the best fit with a time-of-flight profile function of type 4 (in GSAS library), that is a convolution between a pair of back-to-back exponentials and a pseudo-Voigt [114]. For the Rietveld refinement of the experimental data, the range $d > 5 \text{ \AA}$ is excluded because of the unreliability of the peak intensity and peak shape model in this long wavelength region, and none of the peak profile functions available in GSAS is able to model them correctly. Moreover, also the peak profile shape extracted by mean of the NaCaAlF refinement is somewhat inadequate for large λ . This sample is a common one as a calibration standard for its wide d -range span, but it is not ideal because of its variable synthesis conditions, bringing to the presence of several micro-structural features affecting the diffraction peak shape, such that defect density, domain size, and compositional discrepancies. Anyhow, in the

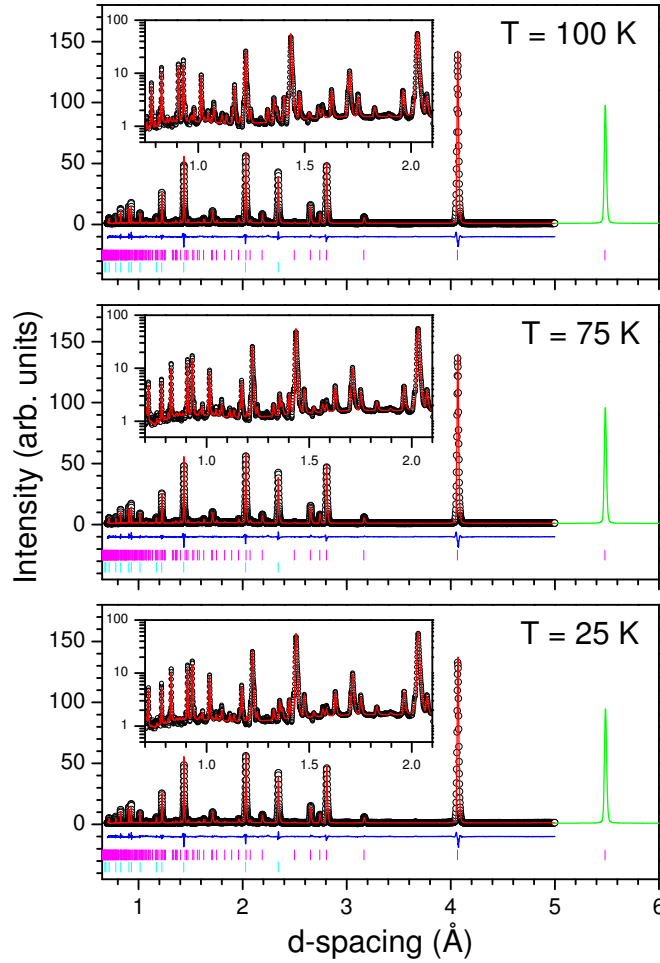


Figure 8.2: *Diffraction patterns used for the refinement of the structure with the Rietveld method, while aluminium peaks are treated with Le Bail method. Space group used is $P6_122$. The refined parameters are listed in Table 8.1. In the inset an enlargement of the low d zone is presented on a semi-log plot. Circles are experimental points, fitted by the red line, while residuals are in blue. Magenta and cyan vertical bars mark the reflection positions of the XVII and aluminium peaks, respectively. For $d > 5$ Å experimental data are not fitted, and the calculated diffraction peak, using the peak profile parameters obtained with the fit, is presented in the figure with green line.*

excluded range only one peak $((h, k, l) = (100))$ of the diffraction pattern of our sample is present and in the whole remaining region the pulse shape can be modelled with adequate accuracy so that peak profiles in NaCaAlF are well reproduced by profile of type 4 [114]. The aluminium Bragg peaks present in the diffraction data have been treated with Le Bail method, thus modelling our sample as composed by two phases.

The space groups assumed for the Rietveld refinement of the ice XVII diffraction pattern are those proposed for describing the filled C_0 -structure, namely $P3_112$ [3], with oxygen atoms in fully-occupied Wyckoff $3a$ and $3b$ sites and deuterium atoms in half-occupied $6c$ sites, and $P6_122$ [6], with oxygen atoms in fully-occupied $6b$ sites and deuterium atoms in half-occupied $12c$ sites. Both groups have a hexagonal unit cell and the first one is a subgroup of the second one. The deuterium sites are always half-occupied to take into account the time-averaged structure, that Raman measurements have demonstrated being disordered. For comparing the quality of the fit using different structural models, we have used the value of the weighted-profile R_{wp} factor [115]

$$R_{wp} = \sqrt{\frac{\sum_i w_i (y_{c,i} - y_{o,i})^2}{\sum_i w_i (y_{o,i})^2}} \quad (8.1)$$

where $y_{o,i}$ is the observed data in the i -th d -spacing channel, $y_{c,i}$ is the computed one from the model and $w_i = \sigma^{-2}(y_{o,i})$ is the statistical weight. For the two structural models proposed above, the value of R_{wp} turns out to be the same (about 11 %). Moreover the values of the refined oxygen coordinates x for sites $3a$ and $3b$ of the group $P3_112$ result related by $x_{3a} = 1 - x_{3b}$, so that these positions coincide with the refined one of the site $6b$ of the $P6_122$ group. The fits, performed for each space group, give similar results, so the $P6_122$ group is preferred for the description of the ice XVII structure, since this space group has a higher symmetry and a lower number of free parameters compared to the $P3_112$ group. The refined structural parameters are reported in Table 8.1 and Table 8.2, while a pictogram of the resulting structure of ice

XVII is shown in Figure 8.3.

T (K)	Atom	Site	x	y	z	B_{iso}	Occ.
25	O1	6b	0.23578(37)	$2x$	$1/4$	2.37(10)	1.0
25	D1	12c	0.6573(10)	0.42197(95)	0.8769(13)	4.05(16)	0.5
25	D2	12c	0.93633(99)	0.62954(72)	0.80539(92)	3.34(14)	0.5
75	O1	6b	0.23602(42)	$2x$	$1/4$	2.96(15)	1.0
75	D1	12c	0.6575(11)	0.4219(11)	0.8772(15)	4.68(27)	0.5
75	D2	12c	0.9359(13)	0.62946(88)	0.8048(10)	3.75(27)	0.5
100	O1	6b	0.23608(46)	$2x$	$1/4$	3.36(16)	1.0
100	D1	12c	0.6567(12)	0.4213(12)	0.8774(16)	5.09(30)	0.5
100	D2	12c	0.9361(14)	0.62962(94)	0.8049(11)	4.14(30)	0.5

Table 8.1: *Atomic fractional coordinates obtained by means of Rietveld refinement (space group $P6_122$) of the diffraction pattern of ice XVII measured at three different temperatures.*

T (K)	a (Å)	c (Å)
25	6.32849(14)	6.05472(22)
75	6.32867(14)	6.05560(22)
100	6.33051(14)	6.05797(22)

Table 8.2: *Lattice constants obtained by means of Rietveld refinement (space group $P6_122$) of the diffraction pattern of ice XVII measured at three different temperature.*

Water molecules form spiralling channels along the z axis with a free bore hole of about 5.26 Å and with a diameter of about 6.10 Å, which can accommodate H₂ molecules. The refined positions of the deuterium atoms, obtained from the fit without applying any constraint, are perfectly consistent with the water molecule structure. Oxygen atoms are tetrahedrally coordinated, with

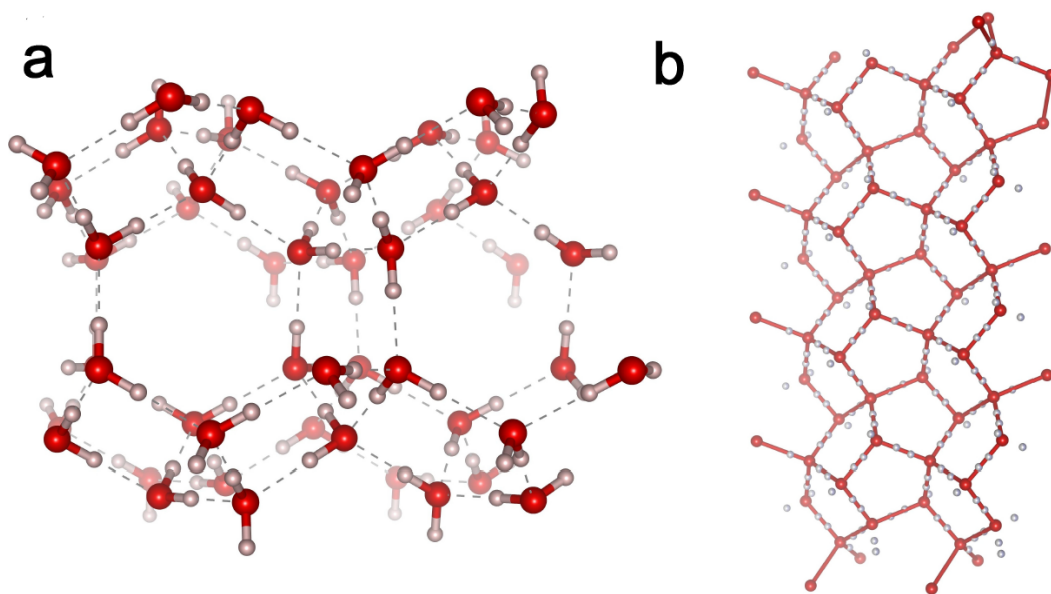


Figure 8.3: *Prospective drawings of the structure of ice XVII. (a) View along the z axis. For graphical reasons water molecules are drawn in one out of the many configurations satisfying Bernal and Fowler ice rules. This orientation brings into view the hexagonal channels along the z axis, which have a free bore hole of about 5.26 \AA and a diameter of about 6.10 \AA . (b) View along the y axis. In this case each hydrogen site is half occupied, according to the half-hydrogen model [11]. Here the pentagonal tessellation is evident. These drawings are produced with the software VESTA [15].*

nearest neighbours that sit at two possible distances, namely $d_1 = 2.7395(4) \text{ \AA}$ and $d_2 = 2.774(2) \text{ \AA}$. Deuterium atoms occupy two sites having the same symmetry, indicated in the following as D1 and D2. The deuterium atoms are used also to identify the O-O bond, since the two positions on the same bond are of the same type. Moreover, given the two possible distances between oxygen atoms, d_1 and d_2 , O-D distances are $1.023(7) \text{ \AA}$ and $1.006(4) \text{ \AA}$ respectively. Three possible values are obtained for the O-O-O and D-O-D angles, listed in Table 8.3, which are correlated with the type of deuterium atom, D1

or D2, of each O-O bond. There is a large correlation between O'-O-O'' and D-O-D' angles, but the water molecule tends to possess an angle whose average is 110.0°, while the O'-O-O'' angle is in some instances as large as 124.5°. To appreciate the misalignment of the deuterium atoms with respect to the O-O' bond, in Table 8.3 we have reported also the angle O-D-O' for the two types of deuterium. This is very close to 180° for D1 and somewhat smaller for D2.

	Deuterium atom on the bond		
	D1	D2	
d_{OD} (Å)	1.023(7)	1.006(4)	
d_{OO} (Å)	2.739(4)	2.774(2)	
O-D-O' (deg)	178.0(4)	171.1(5)	
	Deuterium atoms on the bonds		
	D1-D1	D2-D2	D1-D2
D-O-D' (deg)	110.4(4)	113.1(4)	108.6(4)
O'-O-O'' (deg)	108.32(5)	124.48(7)	106.11(8)

Table 8.3: Atomic distances and angles obtained by Rietveld refinement (space group $P6_122$) of the diffraction pattern of ice XVII measured at 25 K. Deuterium atoms of different sites, indicated as D1 and D2, identify also the O-D-O' bond. Distances are in Å and angles are in degrees.

The behaviour with temperature of the lattice constants and unit cell volume is reported in Figure 8.4, where it is compared with that of ice *Ih* [116]. The density of the D₂O ice XVII at 100 K is 0.95018(5) g/cm³, that is 11% lower than that of D₂O ice *Ih* at the same temperature, but slightly larger than that of the empty sII clathrate (ice XVI), which is about 0.90 g/cm³ [7]. The low number of investigated temperatures does not allow to determine with

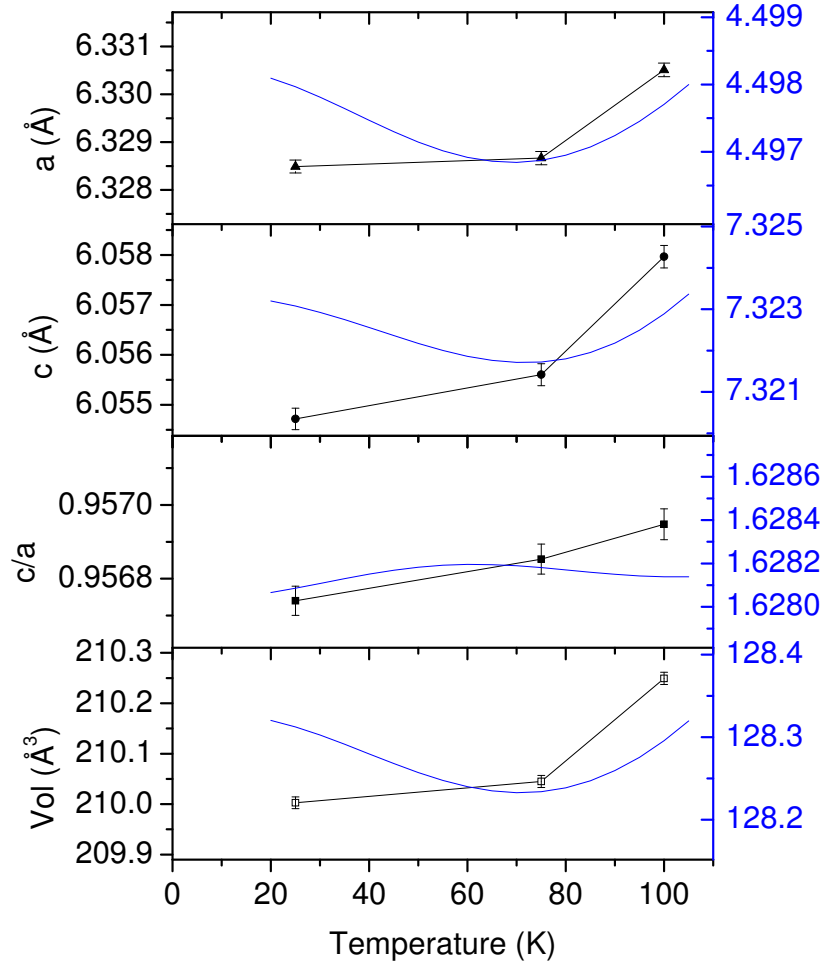


Figure 8.4: *Temperature dependence of the lattice constants of D_2O ice XVII (black symbols and black line, left vertical scale) and of D_2O ice Ih [116] (blue line, right vertical scale). For an easier comparison, the relative vertical scale range of the right and left axis is the same, and corresponds to the same relative change of the parameter.*

precision the thermal expansivity, which may be possibly negative between 25

and 75 K, similarly to what obtained by Falenty et al. in the case of emptied sII clathrate, i.e. ice XVI [7]. The c/a ratio reported in Figure 8.4 demonstrates that thermal expansion is not isotropic in ice XVII, in contrast to what happens for ice Ih.

8.3 Structural studies on filled ice

In this section we will describe the measured effect of different degree of filling by guest molecules (H_2 or D_2) on the structure of the pristine sample in the C_0 -phase and of the ice XVII.

8.3.1 The C_0 -phase filled ice as synthesized

The first structural measurements on C_0 -structure by neutron diffraction have been performed on WISH diffractometer, at ISIS (RAL, U.K.). The experiment has been focused on the characterization of three samples originating from three different synthesis batches, two completely deuterated ($D_2O + D_2$) and named *Sample 1* ($S1$) and *Sample 2* ($S2$), and one with protonated guest ($D_2O + H_2$) and named *Sample 3* ($S3$). As said in the previous section, the choice of using heavy water, that is characterized by a higher coherent scattering cross section than protonated water, is done for maximizing the intensity of the Bragg reflections of the host structure, while the use of different guests may be useful to obtain informations about relative changes in ice structure due to different guest-host interactions. Since the sample cell is not provided with a connection to a gas handling system, all three samples undergo only one thermal cycle of heating, typically from 10 K to 110 K. Due to the absence of an evacuating system connected to the cell, it has been possible to study samples undergoing only to a partial evacuation by the guest.

Full range diffraction patterns, expressed in function of d -spacing, are anal-

used by Le Bail method using the software GSAS [114]. As in the OSIRIS experiment previously described, we perform a Rietveld refinement on a reference sample (silicon powder in this case), obtaining the best fit with a time-of-flight profile function of type 4 [114]. For the Le Bail analysis of experimental data the range $d > 5 \text{ \AA}$ is excluded because of a known issue with solid methane moderator, which gives rise to a resulting relative resolution $\Delta d/d$ not constant with d [117].

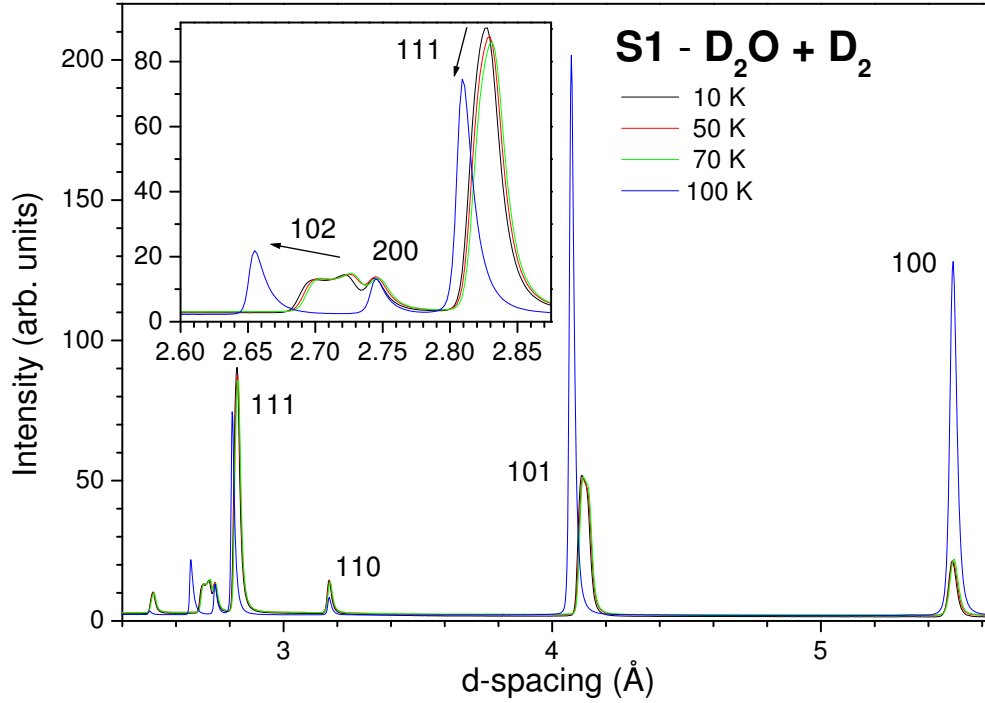


Figure 8.5: *WISH* experimental raw diffraction patterns of pristine filled ice sample *S1* measured at increasing temperature (solid lines). The plotted range is limited to 2.40 - 5.65 Å to improve the visualization of high- d range. Black arrows indicate the shift of some Bragg peaks during the heating cycle.

The measured diffractograms during a heating cycle and, in some cases, a subsequent cooling, are reported in the Figure 8.5, 8.6 and 8.7. Since the positions of the Bragg peaks are almost the same in the low-temperature patterns,

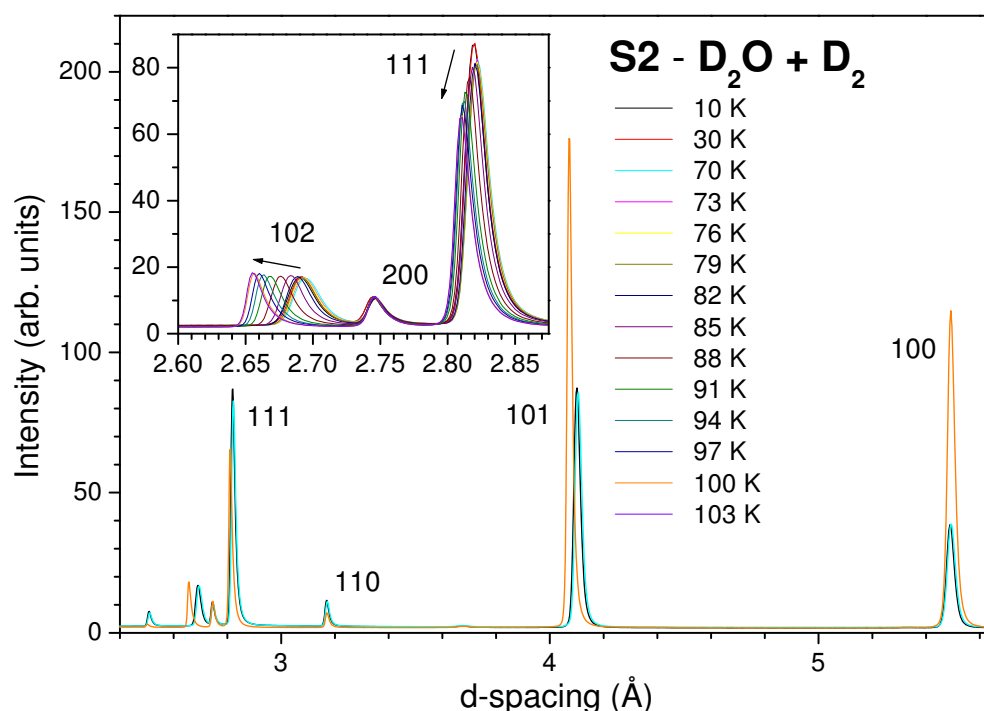


Figure 8.6: *WISH* experimental raw diffraction patterns of pristine filled ice sample *S2* measured at increasing temperature (solid lines). The plotted range is limited to 2.40 - 5.65 Å to improve the visualization of high- d range. Black arrows indicate the shift of some Bragg peaks during the heating cycle.

these data demonstrate the reproducibility of the structure of the sample coming from different synthesis batches. In all the three samples (*S1*, *S2* and *S3*) the effects of increasing temperature are quite evident. Firstly, it is possible to note the increase of the intensity of the reflection at the higher d values, secondly, there is a down-shift of only some peaks (the shift is indicated by black arrows in the relative figures). These effects are probably due to the progressive evacuation of the channels by the guest molecules and the consequent shrinkage of the host lattice. Moreover, the absence of peak shifts of the same magnitude recorded during re-cooling of the sample *S3* down to 60 K (dotted lines of Figure 8.7) allows definitively to exclude that this effect could

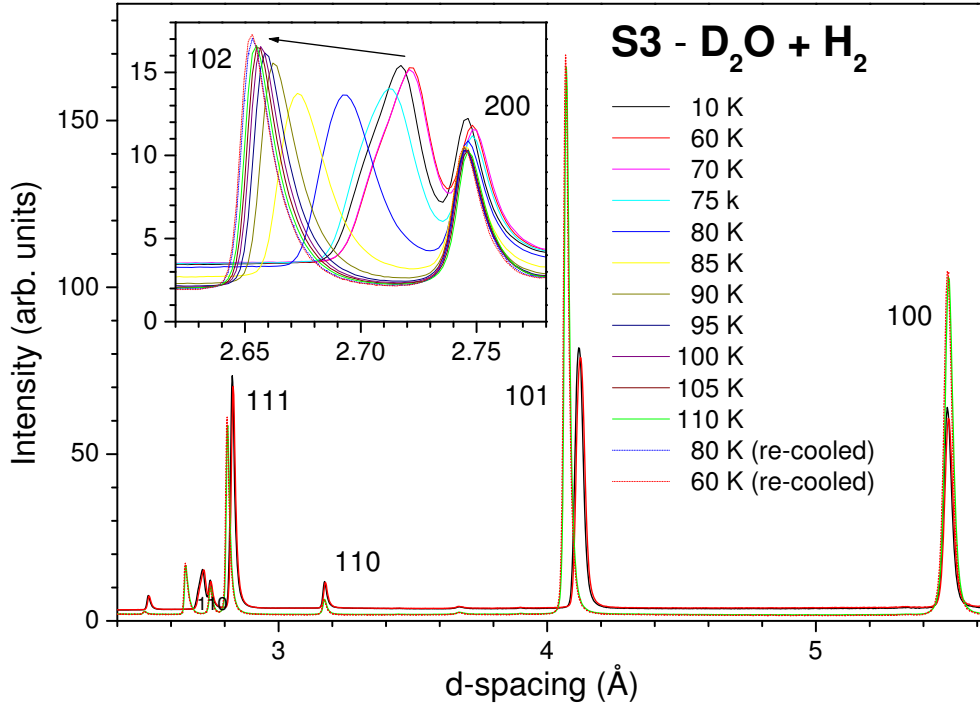


Figure 8.7: *WISH* experimental raw diffraction patterns of pristine filled ice sample *S3* measured at increasing temperature (solid lines) and during a re-cooling cycle (dotted lines). The plotted range is limited to 2.40 - 5.65 Å to improve the visualization of high-*d* range. Black arrows indicate the shift of some Bragg peaks during the heating cycle.

be related to a reversible phenomenon like thermal expansion. In particular, assuming the same hexagonal symmetry used for ice XVII ($P6_122$) and indexing the peaks as reported in Figure 8.5, 8.6 and 8.7, it is interesting to note that only peaks having Miller index $l \neq 0$ are moving when sample is emptying. In real space this corresponds to a variation of distance between symmetry planes that intercept the z axis, i.e. to an elongation of the channels along its symmetry axis. Anyway, in this nicely consistent picture, only the (102) reflection, located at $d \simeq 2.71$ Å, seems to have a strange behaviour (see Figure 8.8). Comparing the different samples before the heating cycle, the position of

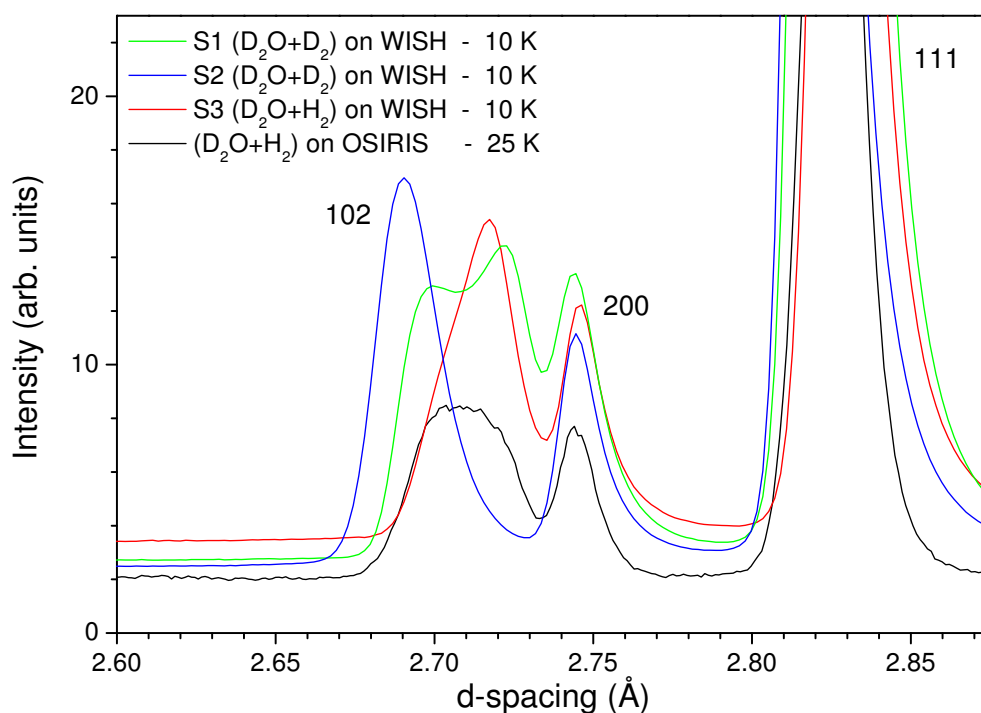


Figure 8.8: Comparison between diffractograms of different samples measured on WISH and OSIRIS instruments at low temperature in the range 2.60 - 2.87 Å. The details of the samples are indicated in the legend. Peak indexing is done assuming the hexagonal space group $P6_122$.

this peak is not always the same in each sample, and, in some cases, the peak appear quite large, as if it were composed by more than one component. This fact is also observed in analogous measurement performed on OSIRIS (black line in the same figure). However the peculiarity of this reflection disappear irreversibly when the sample undergoes a heating cycle over 80 K. Maybe this reflection could be a fingerprint for the presence of another spurious guest species in the pristine sample, e.g. nitrogen, as it has been demonstrated by Raman measurements showed in previous Section 6.2. Probably samples as synthesized are a solid mixture of hydrogen filled ice and nitrogen filled ice, both in the C_0 -phase (i.e. the same space group symmetry), but characterized

by a different set of lattice parameters. Moreover, actually the crystallographic sites of the guest molecules are not known. These two facts prevents a Rietveld refinement of the C_0 -structure. Anyhow, the lattice parameters can be quantitatively estimated by Le Bail method and the results for $S1$, $S2$ and $S3$ samples as a function of the temperature are reported in Figure 8.9. The initial values

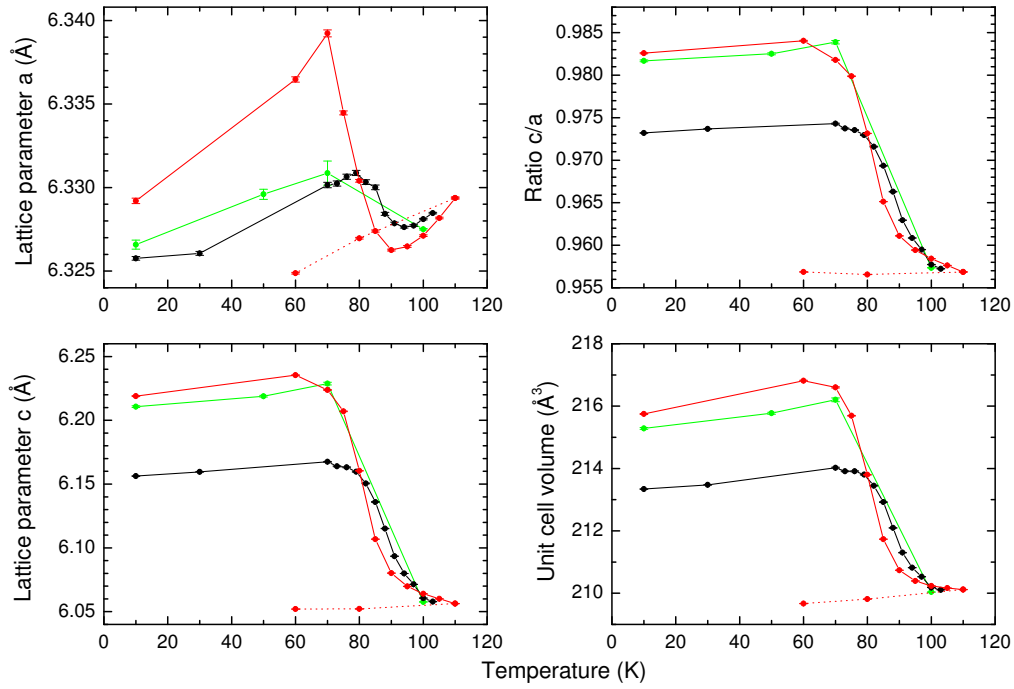


Figure 8.9: *Temperature dependence of lattice constants a , c , the ratio c/a and the unit cell volume V (given by $\frac{\sqrt{3}a^2c}{2}$ for hexagonal unit cell) of different samples of C_0 -phase filled ice measured on WISH. In the graphs the sample $S1$ and sample $S2$ ($D_2O + D_2$) are represented with green and black points respectively while sample $S3$ ($D_2O + H_2$) is represented with red points. The solid and dotted lines connecting data points indicate that measurements are performed during, respectively, heating and cooling of the samples. Error bars are derived from Le Bail analysis with GSAS software.*

(at 10 K) of a and c are slightly different among the three samples, probably

due to different initial hydrogen or nitrogen content. The lattice parameter a shows a quite similar behaviour with temperature for all samples. Between 10 and 70 K an almost linear increase is measured and it can be explained by considering thermal expansion. Above 70 K, two ranges of temperature with different behaviour are evident, one with negative slope up to 90 K and a second one with positive slope over 90 K. These different behaviours could be due to the remove from the ice structure of two different guests, namely nitrogen and hydrogen. At about 100 K, a tends to reach the same value in all three cases, which is consistent with an almost complete evacuation of the sample. During a subsequent cooling, performed only on $S3$, a has a linear dependence with temperature, and this behaviour is consistent with usual thermal expansion of some forms of pure ice. There are similar evidences also for the lattice parameter c , except for the behaviour above 60 K. In this case the parameter decreases probably with two different rates due to the removing of the two guest species. Since the absolute variations of this parameter are one order of magnitude larger than a , the temperature-dependence of c/a ratio and unit cell volume closely follows the behaviour of c . Hence the thermal expansion, that is measured for the annealed ice, is superimposed on an initial irreversible decrease of total volume caused by the evacuation of the structure. The removal of the guest molecules involves a significant contraction of the unit cell in the z direction, while along x or y axes there is a smaller expansion or contraction, depending on the nature of guest, that is on the different interaction potential experienced by guest molecule.

Also the measurements performed on OSIRIS diffractometer can give structural informations about the pristine sample. In this case the cell containing the sample is connected to gas handling system, that allows to complete evacuation of a C_0 sample ($D_2O + H_2$), thus obtaining D_2O ice XVII. After that, the sample can be refilled with hydrogen, even at low temperature. The diffraction

patterns are measured for each of these states of the sample at the same temperature for pointing out only the structural changes caused by the guest-host interaction. The experimental raw diffractograms are reported in Figure 8.10.

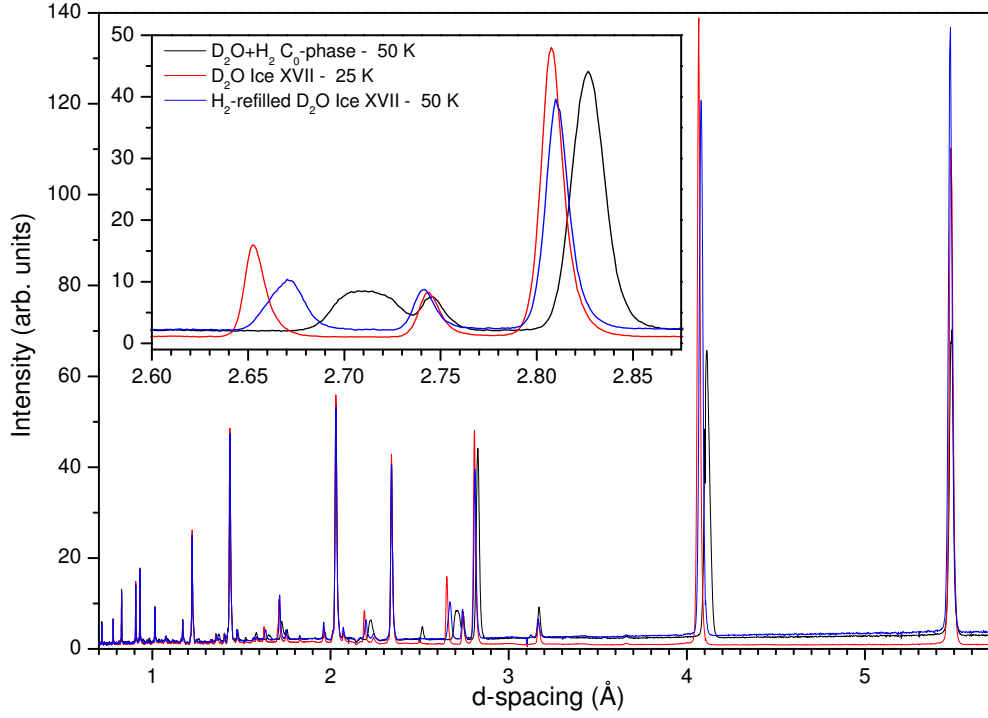


Figure 8.10: *OSIRIS experimental raw diffraction patterns of C_0 -phase ($D_2O + H_2$) as synthesized, measured at 50 K (black line), emptied C_0 -phase (D_2O Ice XVII) after annealing treatment, measured at 25 K (red line) and H_2 -refilled Ice XVII, measured at 50 K (blue line).*

The effects obtained by the annealing treatment of the pristine sample, i.e. by production of ice XVII, are quite similar to those recorded during heating in WISH experiment described just above, with an evident down-shift of the peaks characterized by $l \neq 0$ and a strong increase of the intensity of high- d reflections. Also in this experiment, the (102) peak ($d \simeq 2.71$ Å) in the diffraction pattern of the pristine sample is quite larger, hence giving an indication of a possible contamination of the hydrogen-filled ice by nitrogen molecules.

Refilling ice XVII with hydrogen involve a small shift of the same peaks, i.e. those with $l \neq 0$, towards higher d -spacing. A detailed structural study of refilled ice XVII is presented in the next paragraph, however from Figure 8.10 it is possible to assert that the refilled structure is distinct from the filled ice as synthesized, at least as it regards the unit cell dimensions, or maybe even for space group symmetry. A set of measurements on ice XVII performed at different temperatures, whose experimental patterns are reported in Figure 8.11, demonstrate that the thermal effect has a lighter impact on position of all Bragg reflections, compared to the effect of guest removal or insertion.

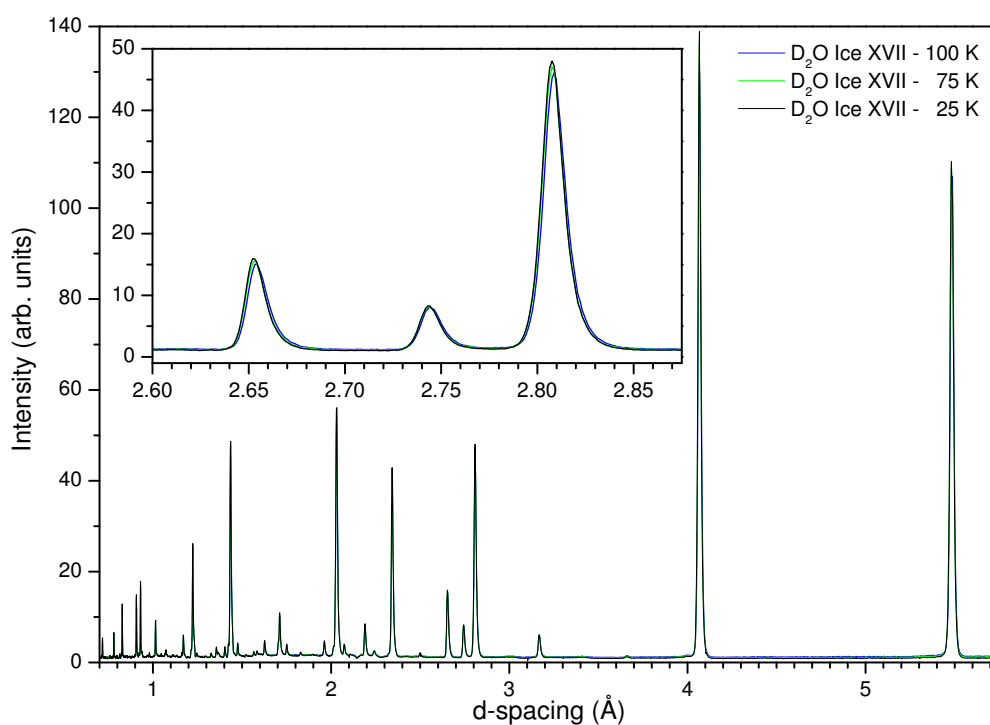


Figure 8.11: *OSIRIS* experimental raw diffraction patterns of emptied C_0 -phase (i.e. ice XVII) measured at 100 K (blue line), 75 K (green line) and 25 K (black line).

8.3.2 Refilled ice XVII

After the structural measurements of the empty sample with OSIRIS diffractometer, we have studied the ability of the sample to re-adsorb hydrogen. Since in the experiment on OSIRIS the D₂O ice XVII sample has been refilled with H₂ as guest for optimizing the signal due to hydrogen diffusion measured by QENS spectrometer (see Section 5.5), it is not possible to draw any conclusion on the water structural symmetry and on the crystallographic sites occupied by guest molecules. This is due both to small coherent cross section of the protonated-guest and to the limited $d3$ range, that is the interval 3.0 - 4.3 Å obtained with $d3$ chopper settings, in which the diffraction pattern is measured, i.e. the only range acquirable when the instrument is set for spectra acquisition, as in our case. Hence, these data do not allow a Rietveld refinement, but assuming the same spatial group $P6_122$ for water structure, it is possible to measure the behaviour of lattice constants a and c in function of increasing hydrogen content in the sample. For estimating this last quantity, we have exploited the large incoherent scattering cross section of H₂ molecules, which give rise to a significant background, in the diffraction pattern, almost independent on d . The level of the background is easily measurable and can be considered proportional to the increasing hydrogen content during the refilling of the ice XVII sample, as clearly shown in Figure 8.12. Even if this method do not give an estimation of the absolute hydrogen content, this relative calibration allows to plot lattice parameter behaviour in function of hydrogen content. As shown in the graphs in Figure 8.13, the adsorption of hydrogen induces a decrease of a , i.e. a contraction of the channels in the xy plane, and an increase of c , i.e. an elongation of the unit cell along the z axis, both implying a 0.6 % volume increase. This overall effect cannot be naively attributed to a swelling of the ice due to the guest, since H₂ - D₂O interaction is mainly attractive for the range of distance pertinent to the hosting of H₂ in the channels, as it is

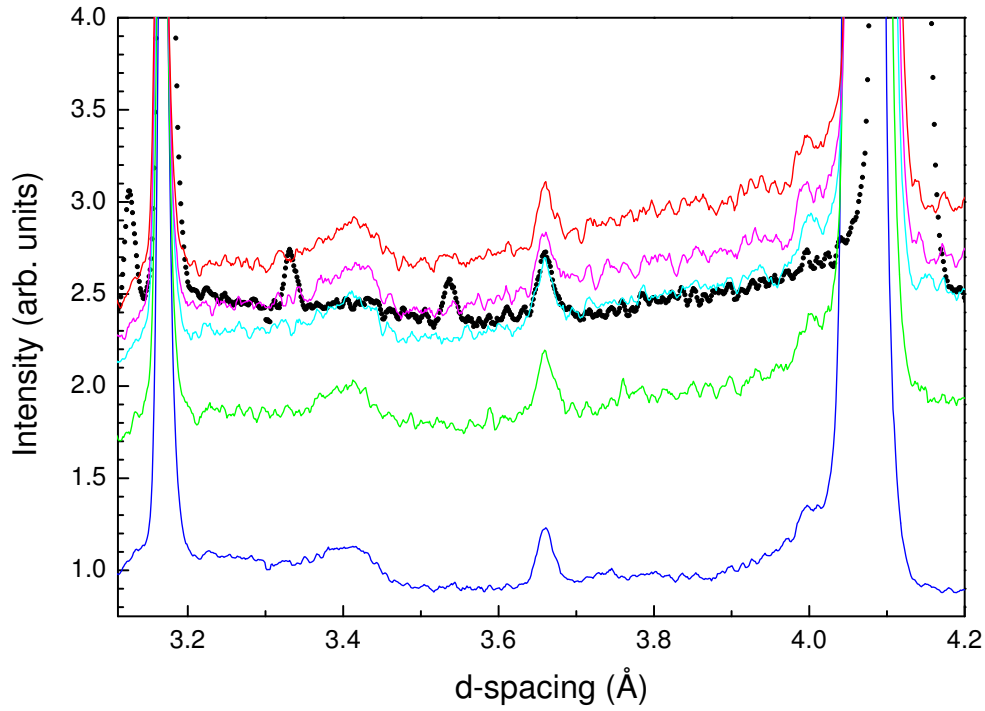


Figure 8.12: *Some examples of OSIRIS experimental raw diffractograms measured at 50 K in the limited range 3.0 - 4.2 Å (d3 range). The pattern of the pristine sample as synthesized ($D_2O + H_2$) and the annealed empty one (ice XVII) are reported with black points and blue line respectively. The green, cyan, magenta and red lines represent patterns acquired after subsequent refilling steps of H_2 .*

attractive for Ne in the sII clathrate [7]. In any case these changes are from six to ten times larger than those due to temperature change in the range 25-100 K, so they represent a considerable physical effects that need to be studied in more detail with further diffraction experiment.

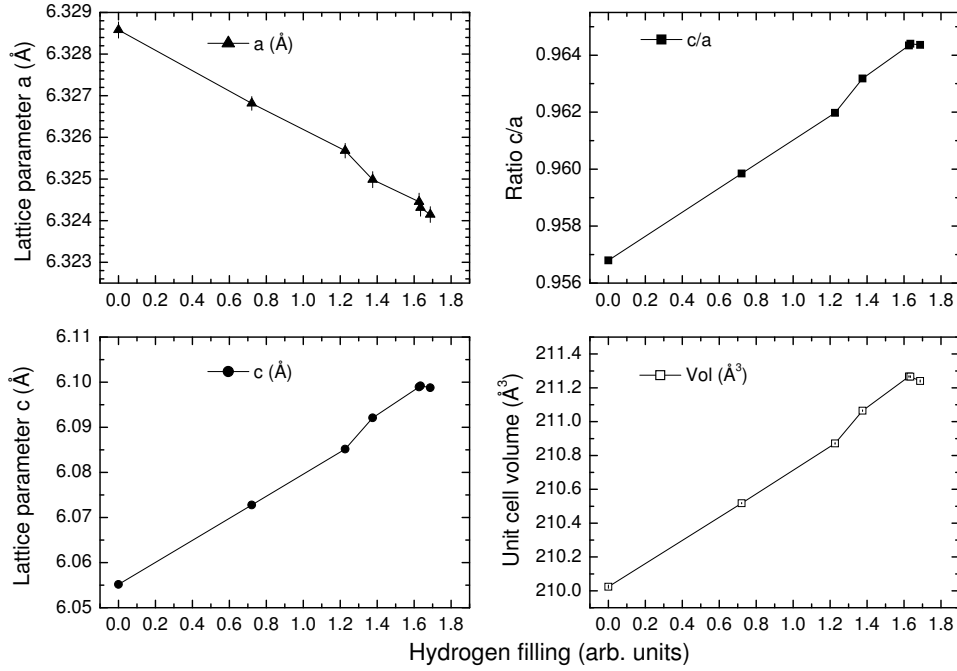


Figure 8.13: *Dependence of the lattice constants of the C_0 -phase filled ice upon filling with hydrogen, with temperature of the sample set at 50 K. The amount of hydrogen adsorbed in the sample is given in arbitrary units and is estimated from the incoherent background present in the OSIRIS diffraction data, which in these cases span a limited range in d , namely between 3.0 and 4.3 Å.*

8.4 Single molecule potential in filled ice

For the description of the filled ice structure, in the case of both pristine sample in the C_0 -phase or refilled ice XVII, two structures, namely $P6_122$ and $P3_112$, have been proposed in previous sections. From a theoretical point of view it is also possible to speculate on what could be the effect of the guest on the structure of this type of ice. It is useful to remember that space group $P3_112$ is a subgroup of $P6_122$ and one structure can change into the other by means of a displacive transition. For particular values of the coordinates of the atoms in sites $3a$ and $3b$ the symmetry of the structure increases and the

crystal can be described by the group $P6_122$. We have calculated the potential energy field probed by a H_2 molecule as a function of its position inside the channel for both structures considered as rigid. For each structure, we have located in the xy plane the minimum of the energy for about 60 fixed values of the vertical coordinate z . These minima are located along a helix, winding around a cylinder with a radius of about 2.0 \AA , having the same period as the lattice along z . However the potential energy along the helices has a quite different behaviour for the two structures. While for $P6_122$ a hypothetical H_2 molecule moving along the helix would feel an almost constant potential energy, for $P3_112$ the same molecule should cross three potential maxima (and three minima) per unit cell length. The situation is depicted in Figure 8.14. The potential barriers between the minima ($\simeq 10 \text{ meV}$) are not so high to prevent diffusion of H_2 , since zero-point energy is probably higher. Given the low energy difference between the two structure, it is also possible that H_2 guests, entering the channels, modify the symmetry of the structure of ice XVII, and accommodate themselves at the bottom of the potential well that themselves induce. In this picture the H_2 molecules would occupy sites with a spacing commensurate with the period of the host lattice. Two observations are in agreement with this speculation. The first one is the large hysteresis in the gas absorption-release process, described in detail in Section 6.3 and the maximum amount of adsorbed H_2 that gets close to 50 % molar. The second one is the elongation of the unit cell along the z axis, that might be favoured by the repulsive potential energy between nearest-neighbour guests, which would influence the structure. In any case at this level these are only speculations and more measurements are needed to confirm them.

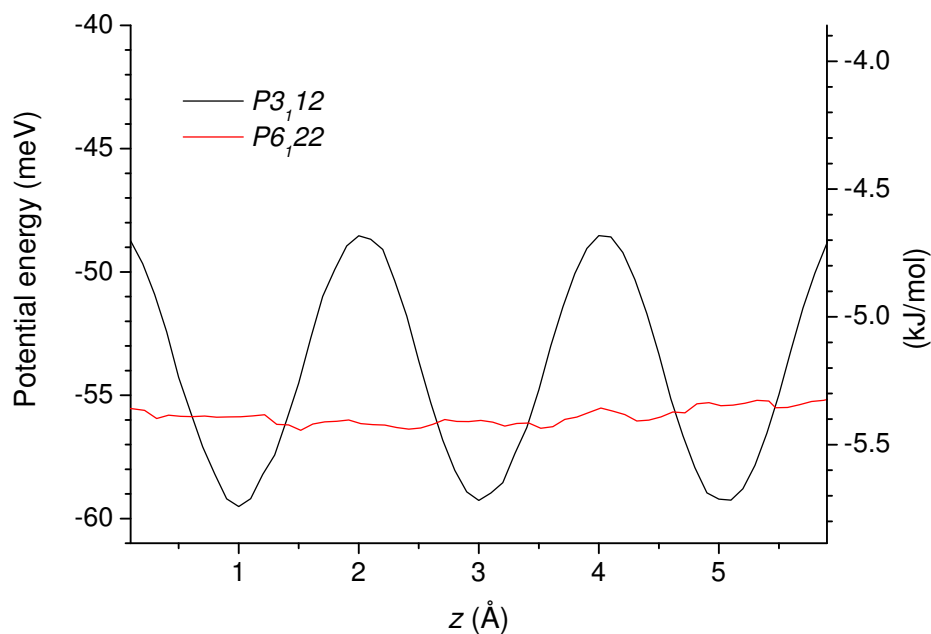


Figure 8.14: Potential energy barriers for the motion of one H_2 molecule along the helix of relative minima inside the channels, for the two structures considered. The right vertical scale reports the potential energy in kJ/mol. Lattice constants assumed for this calculation are $a = 6.331396$ Å and $c = 6.055204$ Å, and site coordinates $x_{3a} = 0.23$ and $x_{3b} = 0.75$ for group $P3_{12}$ and $x_{6b} = 0.24$ for group $P6_{22}$. Potential energy model for H_2 - D_2O interaction is based on the SPC/e model for water, interacting with a Lennard-Jones site on the H_2 center of mass and on point charges on D, H, O and center of mass of H_2 , as in ref. [118].

Chapter 9

Conclusions

In this work we have performed the first characterization of the dynamics of the filled ice sample in the C_0 -phase, synthesised at about 400 MPa and 255 K, and recovered at room pressure and liquid nitrogen temperature, still containing a large fraction of molecular hydrogen. The Raman spectra of this sample point out some differences compared to similar solid inclusion compounds as the sII clathrates. Moreover they show some features in the host and guest vibrational modes that seem to confirm the actually proposed spatial group symmetry $P3_112$ for the C_0 -structure, that results to have a proton-disordered crystal lattice, with water molecule arranged in a channel-like configuration.

Raman measurements have also demonstrated without any doubt that the sample recovered in a liquid nitrogen bath after the synthesis is very often contaminated by spurious guest molecules such as nitrogen. This prevents the refinement of its crystal structure and the pristine sample cannot be taken as a reference for a pure hydrogen C_0 -structure. The analysis of the Raman bands, together with the temperature-dependence of the unit cell parameters, estimated by neutron diffraction data (WISH), allow us to affirm that, during an heating cycle, the sample starts to release nitrogen at about 80 K, up to an almost complete evacuation of the host structure reached at about 110

K. This evacuation process is facilitated by performing the heating treatment under dynamic vacuum (i.e. annealing), allowing to obtain a complete empty C_0 -structure in about 1 h. As a matter of fact in this way we have obtained a new form of metastable ice, named by us *Ice XVII*, which results mechanically stable up to 130 K. The little differences present in the Raman host vibrational bands between the pristine sample and the ice XVII suggest only a slight rearrangement of the water molecules due to a complete removing of the guests. This hypothesis has also been confirmed by OSIRIS diffraction data. The diffraction pattern of ice XVII has been indexed with a hexagonal cell and refined with space group $P6_122$, obtaining accurate values of the oxygen and deuterium positions. The temperature-dependence of the lattice parameters shows a thermal expansion by increasing the temperature in the range from 25 to 100 K. Considering the water molecule disposition in the real space, it is still present a channel-like configuration peculiar of the C_0 -phase, even if in this case the guest-host interaction does not contribute any more to the stability of the entire structure. This fact, already observed in the case of ice XVI, opens the debate about the role played by the guest molecule in gas hydrates compound and more computational works should be done in this field for a better comprehension of this phenomenon. Furthermore it is interesting to note that this structure is composed of pentagonal rings only and this represents an unique case in the overview of the network topologies of the ice polymorphisms.

A surprising aspect of the ice XVII, never observed for other forms of ice, is its porosity, i.e. the ability to readsorb molecular hydrogen, even at relatively low pressure (less than 0.1 MPa), reaching a maximum filling of about 50 % hydrogen molar fraction. By means of Raman spectroscopy and an apparatus for volumetric measurements connected to the Raman cell, we have measured various adsorption and desorption isotherms at different temperatures between 15 K and 80 K, observing a temperature-dependent hysteresis.

Applying a heating treatment, the pristine sample starts to release hydrogen at temperature higher than the refilled one, demonstrating that in the sample just after the synthesis some possible structural defects and the spurious nitrogen molecules hinder the diffusive motion of the hydrogen molecules inside the channels. Anyway for the comprehension of the diffusion processes in this sample, it is necessary to take into account also quasi-elastic neutron data, that, however, are not part of this work.

The measurement of the rate of ortho-para conversion for the H_2 guest populations reveals that both conversion mechanisms, intrinsic and extrinsic, must be considered. In particular the higher value of the intrinsic conversion constant in the filled ice compared to the clathrate case demonstrates a stronger interaction between guest molecules in the C_0 -phase, and this fact is also corroborate by the different widths of the H_2 Raman rotational lines in the two cases.

The structure of the pristine C_0 -phase and refilled ice XVII does not change significantly, and in this two cases the guest molecules occupy the same positions in the channels, probably in a spiralling configuration. These considerations are confirmed by both dynamic (Raman spectra and TOSCA neutron spectra) and structural (WISH and OSIRIS diffractograms) data. Moreover, in the hypothesis of considering the same group symmetry of the empty ice XVII for the crystal structure of the refilled one, we have been able to measure the variations of the cell parameters of ice XVII induced by adsorption of hydrogen. At a constant temperature of 50 K, we have observed that the two lattice parameters show opposite behaviour, a increases and c decreases, with the volume that shows a linear increase. Hence, the guest seems to induce an elongation of the channel along the z -axis, due to repulsive interaction between nearest-neighbour guests, and a decrease of the channel diameter, due to the attractive guest-host interaction. A similar phenomenon has been already ob-

served comparing the sII neon clathrate and its guest-free structure (ice XVI). In this case the attractive component of the guest-host interaction is dominant compared to the repulsion between guest molecules, and this produce an increase of volume when the clathrate is emptied. Another possibility is that the guest induces a structural transition of the host lattice, which passes from the $P6_122$ symmetry, proper of ice XVII, to the $P3_112$ symmetry, actually proposed for the filled ice in the C_0 -phase. This scenario would be corroborate by the large hysteresis observed in the gas adsorption-desorption process. Anyway these issues about the structure of the refilled ice XVII can be addressed by a measurement of an entire diffraction pattern of a completely deuterated filled ice sample. These data, however, are not available at the moment of this work.

In conclusion, the ice XVII seems to be a really interesting material, both from a fundamental point of view, since its discovery inserts new elements in the debate about the role of the guest molecules in giving stability to the host structure, and as regards to possible technological applications. Indeed this material, as long as kept at temperatures below 130 K, is able to adsorb and to release molecular hydrogen at relatively low pressures (below 0.1 MPa), reversibly, with a rather rapid kinetics and with a number of life cycles theoretically infinite, because only physisorption mechanisms are involved. These properties could make ice XVII really appealing not only in the field of hydrogen storage for automotive, but also for applications in the field of industrial gas separation, or the sequestration of greenhouse gases, due to its proven ability to absorb other types gas in addition to hydrogen.

Bibliography

- [1] Mao, W. L., Mao, H. K., Goncharov, A. F., Struzhkin, V. V., Guo, Q., Hu, J., Shu, J., Hemley, R. J., Somayazulu, M. & Zhao, Y. Hydrogen clusters in clathrate hydrate. *Science* **297**, 2247-2249 (2002).
- [2] Vos, W. L., Finger, L. W., Hemley, R. J. & Mao, H. K. Novel H₂-H₂O clathrates at high pressures. *Phys. Rev. Lett.* **71**, 3150-3153 (1993).
- [3] Efimchenko, V. S., Kuzovnikov, M. A., Fedotov, V. K., Sakharov, M. K., Simonov, S. V. & Tkacx, M. New phase in the water-hydrogen system. *J. Alloys Comp.* **509**, S860-S863 (2011).
- [4] Strobel, T. A., Somayazulu, M. & Hemley, R. J. Phase behavior of H₂+H₂O at high pressures and low temperatures. *J. Phys. Chem. C* **115**, 4898-4903 (2011).
- [5] Smirnov, G. S. & Stegailov, V. V. Toward determination of the new hydrogen hydrate clathrate structures. *J. Phys. Chem. Lett.* **4**, 3560-3564 (2013).
- [6] Strobel, T. A., Somayazulu, M. S., Sinogeikin, V. V., Dera, P. & Hemley, R. J. Hydrogen-Stuffed, Quartz-Like Water Ice. *J. Am. Chem. Soc.*, Just Accepted (2016). DOI: 10.1021/jacs.6b06986

- [7] Falenty, A., Hansen, T. C. & Kuhs, W. F. Formation and properties of ice XVI obtained by emptying a type sII clathrate hydrate. *Nature* **516**, 231-233 (2014).
- [8] Huang, Y., Zhu, C., Wang, L., Cao, X., Su, Y., Jiang, X., Meng, S., Zhao, J. & Zeng, X. C. A new phase diagram of water under negative pressure: The rise of the lowest-density clathrate s-III. *Sci. adv.* **2**, e1501010 (2016).
- [9] Prabhukhot, P. R., Wagh, M. M. & Gangal, A. C. A Review on Solid State Hydrogen Storage Material. *Adv. En. Pow.* **4**, 11-22 (2016).
- [10] Callini, E., Aguey-Zinsou, K. F., Ahuja, R., Ramon Ares, J., Bals, S., Biliskov, N., Chakraborty, S., Charalambopoulou, G., Chaudhary, A. L., Cuevas, F., Dam, B., de Jongh, P., Dornheim, M., Filinchuk, Y., Grbovic Novakovic, J., Hirscher, M., Jensen, T. R., Bjerre Jensen, P., Novakovic, N., Lai, Q., Leardini, F., Mirabile Gattia, D., Pasquini, L., Steriotis, T., Turner, S., Vegge, T., Zuttel, A. & Montone, A. Nanostructured materials for solid-state hydrogen storage: A review of the achievement of COST Action MP1103. *Proc. Nat. Ac. Sci.* **101**, 708-710 (2015).
- [11] Petrenko, V. F. & Whitworth, R. W. *Physics of ice* (Oxford University Press, Oxford, 2006).
- [12] Bartels-Rausch, T., Bergeron, V., Cartwright, J. H. E., Escribano, R., Finney, J. L., Grothe, H., Gutiérrez, P. J., Haapala, J., Kuhs, W. F., Pettersson, J. B. C., Price, S. D., Ignacio Sainz-Díaz, C., Stokes, D. J., Strazzulla, G., Thomson, E. S., Trinks, H. & Uras-Aytemiz, N. Ice structures, patterns, and processes: A view across the icefields. *Rev. Mod. Phys.* **84**, 885-944 (2012).
- [13] Tammann, G. Ueber die grenzen des festen zustandes IV. *Ann. Phys. Ser. 4* **2**, 1-31 (1900).

-
- [14] Pauling, L. The structure and entropy of ice and of other crystals with some randomness of atomic arrangement. *J. Am. Chem. Soc.* **57**, 2680-2684 (1935).
- [15] Momma, K. & Izumi, F. VESTA 3 for three-dimensional visualization of crystal, volumetric and morphology data. *J. Appl. Crystallogr.* **44**, 1272-1276 (2011).
- [16] Fowler, R. H. & Bernal, J. D. Note on the pseudo-crystalline structure of water. *Trans. Far. Soc.* **29**, 1049-1056 (1933).
- [17] Dunaeva, A. N., Antsyshkin, D. V. & Kuskov, O. L. Thermodynamic functions of the phase transitions of high-pressure ices. *Sol. Syst. Res.* **44**, 202-222 (2010).
- [18] Salzmann, C. G., Radaelli, P. G., Slater, B. & Finney, J. L. The polymorphism of ice: five unresolved questions. *Phys. Chem. Chem. Phys.* **44**, 202-222 (2011).
- [19] Kuhs, W. F., Bliss, D. V. & Finney, J. L. High-resolution neutron powder diffraction study of ice Ic. *J. Phys. Colloq.* **48**, 631-636 (1987).
- [20] Engelhardt, H. & Whalley, E. Ice IV. *J. Chem. Phys.* **56**, 2678-2684 (1972).
- [21] Londono, J. D., Kuhs, W. F. & Finney, J. L. Neutron diffraction studies of ices III and IX on under pressure and recovered samples. *J. Chem. Phys.* **98**, 4878-4888 (1993).
- [22] Lobban, C., Finney, J. L. & Kuhs, W. F. The structure of a new phase of ice. *Nature* **391**, 268-270 (1998).
- [23] Kawada, S. Dielectric dispersion and phase transition of KOH doped ice. *J. Phys. Soc. Jap.* **32**, 1442-1442 (1972).

- [24] Tajima, Y., Matsuo, T. & Suga, H. Calorimetric study of phase transition in hexagonal ice doped with alkali hydroxides. *J. Phys. Chem. Solids* **45**, 1135-1144 (1984).
- [25] Line, C. M. & Whitworth, R. W. A high resolution neutron powder diffraction study of D₂O ice XI. *J. Chem. Phys.* **104**, 10008-10013 (1996).
- [26] Salzmann, C. G., Radaelli, P. G., Hallbrucker, A., Mayer, E. & Finney, J. L. The preparation and structures of hydrogen ordered phases of ice. *Science* **311**, 1758-1761 (2006).
- [27] Salzmann, C. G., Radaelli, P. G., Mayer, E. & Finney, J. L. Ice XV: A new thermodynamically stable phase of ice. *Phys. Rev. Lett.* **103**, 105701 (2009).
- [28] Yamamuro, O., Oguni, M., Matsuo, T. & Suga, H. Calorimetric study of pure and KOH-doped tetrahydrofuran clathrate hydrate. *J. Phys. Chem. Solids* **49**, 425-434 (1988).
- [29] Nelson, H., Schildmann, S., Nowaczyk, A., Gainaru, C., Geil, B. & Bohmer, R. Small-angle water reorientations in KOH doped hexagonal ice and clathrate hydrates. *Phys. Chem. Chem. Phys.* **15**, 6355-6367 (2013).
- [30] Kamb, B. Ice II. A proton-ordered form of ice. *Acta Cryst.* **17**, 1437-1449 (1964).
- [31] Kuhs, W. F., Finney, J. L., Vettier, C. & Bliss, D. V. Structure and hydrogen ordering in ices VI, VII, and VIII by neutron powder diffraction. *J. Chem. Phys.* **81**, 3612-3623 (1984).
- [32] Hemley, R. J., Jephcoat, A. P., Mao, H. K., Zha, C. S., Finger, L. W. & Cox, D. E. Static compression of H₂O-ice to 128 GPa (1.28 Mbar). *Nature* **330**, 737-740 (1987).

-
- [33] Davy, H. The Bakerian Lecture: On some of the combinations of oxymuriatic gas and oxygene, and on the chemical relations of these principles, to inflammable bodies. *Phil. Trans. Roy. Soc. Lond* **101**, 1-35 (1811).
- [34] Hammerschmidt, E. G. Formation of gas hydrates in natural gas transmission lines. *Ind. Eng. Chem.* **26**, 851-855 (1934).
- [35] Makogon, Y. f. Hydrate formation in the gas-bearing beds under permafrost conditions. *Gazov. Promst.* **5**, 14-15 (1965).
- [36] Dillon, W. P., Grow, J. A. & Paull, C. K. Unconventional gas hydrate seals may trap gas off southeast US. *Oil Gas J.* **78**, 124-130 (1980).
- [37] Delsemme, A. H. & Wenger, A. Physico-chemical phenomena in comets—I: Experimental study of snows in a cometary environment. *Planet. Space Sci.* **18**, 709-715 (1970).
- [38] Sloan, E. D. & Koh, C. A. *Clathrate Hydrates of Natural Gases*, 3rd Edition (Taylor & Francis, New York, 2008).
- [39] Tulk, C. A., Klug, D. D. & Ripmeester, J. A. Raman spectroscopic studies of THF clathrate hydrate. *J. Phys. Chem. A* **102**, 8734-8739 (1998).
- [40] Kurnosov, A. V., Manakov, A. Y., Komarov, V. Y., Voronin, V. I., Teplykh, A. E. & Dyadin, Y. A. A new gas hydrate structure. *In Dok. Phys. Chem.* **381**, 303-305 (2001).
- [41] Yang, L., Tulk, C. A., Klug, D. D., Moudrakovski, I. L., Ratcliffe, C. I., Ripmeester, J. A., Chakoumakos, B. C., Ehm, L., Martin, C. D. & Parise, J. B. Synthesis and characterization of a new structure of gas hydrate. *PNAS* **106**, 6060-6064 (2009).

- [42] Vatamanu, J. & Kusalik, P. G. Unusual crystalline and polycrystalline structures in methane hydrates. *J. Am. Chem. Soc.* **128**, 15588-15589 (2006).
- [43] Claussen, W. F. A second water structure for inert gas hydrates. *J. Chem. Phys.* **19**, 1425–1426 (1951).
- [44] Ripmeester, J. A., John, S. T., Ratcliffe, C. I. & Powell, B. M. A new clathrate hydrate structure. *Nature* **325**, 135-136 (1987).
- [45] Hirai, H., Tanaka, T., Kawamura, T., Yamamoto, Y. & Yagi, T. Structural changes in gas hydrates and existence of a filled ice structure of methane hydrate above 40 GPa. *J. Phys. Chem. Solids* **65**, 1555-1559 (2004).
- [46] Sun, Q., Duan, T. Y., Zheng, H. F., Ji, J. Q. & Wu, X. Y. Phase transformation of methane hydrate under high pressure. *J. Chem. Phys.* **122**, 024714 (2005).
- [47] Shu, J., Chen, X., Chou, I. M., Yang, W., Hu, J., Hemley, R. J. & Mao, H. K. Structural stability of methane hydrate at high pressures. *Geosci. Front.* **2**, 93-100 (2011).
- [48] Loveday, J. S., Nelmes, R. J., Guthrie, M., Belmonte, S. A., Allan, D. R., Klug, D. D., Tse, J. S. & Handa, Y. P. Stable methane hydrate above 2 GPa and the source of Titan's atmospheric methane. *Nature* **410**, 661-663 (2001).
- [49] International Union of Crystallography. International Table for Crystallography, <http://it.iucr.org/> (2016).
- [50] Loveday, J. S., Nelmes, R. J., Guthrie, M., Klug, D. D. & Tse, J. S. Transition from cage clathrate to filled ice: the structure of methane hydrate III. *Phys. Rev. Lett.* **87**, 215501 (2001).

- [51] Londono, D., Finney, J. L. & Kuhs, W. F. Formation, stability, and structure of helium hydrate at high pressure. *J. Chem. Phys.* **97**, 547-552 (1992).
- [52] Dyadin, Y. A., Larionov, E. G., Manakov, A. Y., Zhurko, F. V., Aladko, E. Y., Mikina, T. V. & Komarov, V. Y. Clathrate hydrates of hydrogen and neon. *Mend. Commun.* **9**, 209-210 (1999).
- [53] Mao, W. L. & Mao, H. Hydrogen storage in molecular compounds. *Proc. Nat. Ac. Sci.* **101**, 708-710 (2004).
- [54] Struzhkin, V. V., Militzer, B., Mao, W. L., Mao, H. & Hemley, R. J. Hydrogen storage in molecular clathrates. *Chem. Rev.* **107**, 4133-4151 (2007).
- [55] Giannasi, A., Celli, M., Zoppi, M., Moraldi, M. & Ulivi, L. Experimental and theoretical analysis of the rotational Raman spectrum of hydrogen molecules in clathrate hydrates. *J. Chem. Phys.* **135**, 054506 (2011).
- [56] Xu, M., Ulivi, L., Celli, M., Colognesi, D. & Bačić, Z. Quantum calculation of inelastic neutron scattering spectra of a hydrogen molecule inside a nanoscale cavity based on rigorous treatment of the coupled translation-rotation dynamics. *Phys. Rev. B* **83**, 241403 (2011).
- [57] Borysow, J., del Rosso, L., Celli, M., Moraldi, M. & Ulivi, L. Spectroscopic and thermodynamic properties of molecular hydrogen dissolved in water at pressures up to 200 MPa. *J. Chem. Phys.* **140**, 164312 (2014).
- [58] Choukroun, M. & Grasset, O. Thermodynamic model for water and high-pressure ices up to 2.2 GPa and down to the metastable domain. *J. Chem. Phys.* **127**, 124506 (2007).

- [59] Lokshin, K. A. & Zhao, Y. Fast synthesis method and phase diagram of hydrogen clathrate hydrate. *Appl. Phys. Lett.* **88**, 131909 (2006).
- [60] Efimchenko, V. S., Antonov, V. E., Barkalov, O. I., Beskrovnyy, A. I., Fedotov, V. K. & Klyamkin, S. N. Phase transitions and equilibrium hydrogen content of phases in the water–hydrogen system at pressures to 1.8 kbar. *Hi. Press. Res.* **26**, 439-443 (2006).
- [61] Antonov, V. E., Efimchenko, V. S. & Tkacz, M. Phase transitions in the water - hydrogen system at pressures up to 4.7 kbar. *J. Phys. Chem. B* **113**, 779-785 (2008).
- [62] Lokshin, K. A., Zhao, Y., He, D., Mao, W. L., Mao, H. K., Hemley, R. J., Lobanov, M. V. & Greenblatt, M. Structure and dynamics of hydrogen molecules in the novel clathrate hydrate by high pressure neutron diffraction. *Phys. Rev. Lett.* **93**, 125503 (2004).
- [63] Strobel, T. A., Hester, K. C., Koh, C. A., Sum, A. K. & Sloan, E. D. Properties of the clathrates of hydrogen and developments in their applicability for hydrogen storage. *Chem. Phys. Lett.* **478**, 97-109 (2009).
- [64] Zaghloul, M. A. S., Celli, M., Salem, N. M., Elsheikh, S. M. & Ulivi, L. High pressure synthesis and in situ Raman spectroscopy of H₂ and HD clathrate hydrates. *J. Chem. Phys.* **137**, 164320 (2012).
- [65] Walsh, M. R., Koh, C. A., Sloan, E. D., Sum, A. K. & Wu, D. T. Microsecond simulations of spontaneous methane hydrate nucleation and growth. *Science* **326**, 1095-1098 (2009).
- [66] del Rosso, L., Celli, M. & Ulivi, L. Raman measurements of pure hydrogen clathrate formation from a supercooled hydrogen–water solution. *J. Phys. Chem. Lett.* **6**, 4309-4313 (2015).

- [67] Celli, M., Zoppi, M., Zaghloul, M. A. S. & Ulivi, L. High pressure optical cell for synthesis and in situ Raman spectroscopy of hydrogen clathrate hydrates. *Rev. Sci. Instr.* **83**, 113101 (2012).
- [68] Giannasi, A., Celli, M., Ulivi, L. & Zoppi, M. Low temperature Raman spectra of hydrogen in simple and binary clathrate hydrates. *J. Chem. Phys.* **129**, 084705 (2008).
- [69] Strobel, T. A., Taylor, C. J., Hester, K. C., Dec, S. F., Koh, C. A., Miller, K. T. & Sloan, E. D. Molecular hydrogen storage in binary THF-H₂ clathrate hydrates. *J. Phys. Chem.* **110**, 17121 (2006).
- [70] Johnson, W. H. On some remarkable changes produced in iron and steel by the action of hydrogen and acids. *Proceed. Roy. Soc. London* **23**, 168-179 (1875).
- [71] Spain, I. L. & Paauwe, J. *High Pressure Technology* (Dekker, New York, 1977).
- [72] Long, D. A. *Raman spectroscopy* (McGraw-Hill, U.K., 1977).
- [73] Califano, S. *Vibrational states* (John Wiley & Son, Bristol, 1976).
- [74] Erzberg, G. *Spectra of diatomic molecules* (Van Nostrand Reinhold Company, 1950).
- [75] Borysow, J. & Moraldi, M. On the interpretation of the Q-branch of hydrogen in water. *J. Phys. B* **49**, 115202 (2016).
- [76] Tinkham, M. *Group Theory and Quantum Mechanics* (McGraw-Hill, U.S.A., 1964).
- [77] Turrell, G. *Infrared and Raman Spectra of Crystals* (Academic Press, London, 1972).

- [78] Wong, P. T. T. & Whalley, E. Optical spectra of orientationally disordered crystals. VI. The Raman spectrum of the translational lattice vibrations of ice Ih. *J. Chem. Phys.* **65**, 829-836 (1976).
- [79] Li, J. C., Nield, V. M. & Jackson, S. M. Spectroscopic measurements of ice XI. *Chem. Phys. Lett.* **241**, 290-294 (1995).
- [80] Abe, K. & Shigenari, T. Raman spectra of proton ordered phase XI of ICE I. Translational vibrations below 350 cm^{-1} . *J. Chem. Phys.* **134**, 104506 (2011).
- [81] Striganov, A. R. & Sventitskii, N. S. *Tables of spectral lines of neutral and ionized atoms* (Plenum, New York, 1968).
- [82] Norlén, G. Wavelengths and energy level of ArI and ArII based on new interferometric measurement in the region 3400-9800 Å. *Phys. Scr.* **8**, 249-268 (1973).
- [83] Squires, G. L. *Introduction to the theory of thermal neutron scattering* (Dover Publication Inc., Mineola, New York, 1996).
- [84] Lovesey, S. W. *Theory of neutron scattering from condensed matter. Volume 1* (Clarendon Press, Oxford, 1984).
- [85] Furrer, A., Mesot, J. & Strassle, T. *Neutron Scattering in Condensed Matter Physics* (World Scientific, Singapore, 2010).
- [86] Young, J. A. & Koppel, J. U. Slow neutron scattering by molecular hydrogen and deuterium. *Phys. Rev. A* **135**, 603-611 (1964).
- [87] Zoppi, M. Neutron scattering of homonuclear diatomic liquids. *Physica B* **183**, 235-246 (1993).

-
- [88] Colognesi, D., Celli, M., Neumann, M. & Zoppi, M. Microscopic self-dynamics in liquid hydrogen and in its mixtures with deuterium. *Phys. Rev. E* **70**, 061202 (2004).
- [89] Celli, M., Colognesi, D. & Zoppi, M. Direct experimental access to microscopic dynamics in liquid hydrogen. *Phys. Rev. E* **66**, 021202 (2002).
- [90] Colognesi, D., Celli, M., Cilloco, F., Newport, R. J., Parker, S. F., Rossi-Albertini, V., Sacchetti, F., Tomkinson, J. & Zoppi, M. TOSCA neutron spectrometer: The final configuration. *Appl. Phys. A* **74** [Suppl.], S64-S66 (2002).
- [91] Ulivi, L., Celli, M., Giannasi, A., Ramirez-Cuesta, A. J., Bull, D. J. & Zoppi, M. Quantum rattling of molecular hydrogen in clathrate hydrate nanocavities. *Phys. Rev. B* **76**, 161401 (2007).
- [92] Celli, M., Colognesi, D., Ulivi, L., Zoppi, M. & Ramirez-Cuesta, A. J. Phonon density of states in different clathrate hydrates measured by inelastic neutron scattering. *J. Phys. Conf. Ser.* **340**, 012051 (2012).
- [93] Martín y Marero, D., Engberg, D. & Andersen, K. H. The polarisation analysis spectrometer and diffractometer at ISIS. *Phys. B*, **150** 276-278 (2000).
- [94] Telling, M. T. F. & Andersen, K. H. *The OSIRIS user guide* (ISIS Facility, Didcot, 2008).
- [95] Arnold, O., Bilheux, J. C., Borreguero, J. M., Buts, A., Campbell, S. I., Chapon, L., Doucet, M., Draper, N., Ferraz Leal, R., Gigg, M. A., Lynch, V. E., Markvardsen, A., Mikkelsen, D. J., Mikkelsen, R. L., Miller, R., Plamen, K., Parker, P., Passos, G., Perring, T. G., Person, P. F., Ren, S., Reuter, M. A., Savici, A. T., Taylor, J. W., Taylor, R. J., Tolchenov,

- R., Zhou, W. & Zikovsky, J. Mantid—Data analysis and visualization package for neutron scattering and μ SR experiments. *Nucl. Instr. Meth. Phys. Res. A* **764**, 156-166 (2014).
- [96] Chapon, L. C., Manuel, P., Radaelli, P. G., Benson, C., Perrott, L., Ansell, S., Rhodes, N. J., Raspino, D., Duxbury, D., Spill, E. & Norris, J. Wish: the new powder and single crystal magnetic diffractometer on the second target station. *Neutron News* **22**, 22-25 (2011).
- [97] Bertie, J. E. & Francis, B. F. Raman spectra of ices II and IX above 35 K at atmospheric pressure: Translational and rotational vibrations. *J. Chem. Phys.* **71**, 1-14 (1982).
- [98] Pimentel, G. C. & Sederholm, C. H. Correlation of infrared stretching frequencies and hydrogen bond distances in crystals. *J. Chem. Phys.* **24**, 639-641 (1956).
- [99] Pruzan, P. Pressure effects on the hydrogen bond in ice up to 80 GPa. *J. Mol. Struct.* **322**, 279-286 (1994).
- [100] Vos, W. L., Finger, L. W., Hemley, R. J., & Mao, H. K. Pressure dependence of hydrogen bonding in a novel $\text{H}_2+\text{H}_2\text{O}$ clathrate. *J. Chem. Phys. Lett.* **257**, 524-530 (1996).
- [101] Van Kranendonk, J. *Solid hydrogen* (Plenum Press, New York, 1983).
- [102] Grazzi, F., Santoro, M., Moraldi, M. & Ulivi, L. Anisotropic interactions of hydrogen molecules from the pressure dependence of the rotational spectrum in the $\text{Ar}(\text{H}_2)_2$ compound. *Phys. Rev. Lett.* **87**, 125506 (2001).
- [103] Grazzi, F., Santoro, M., Moraldi, M. & Ulivi, L. Roton excitations of the hydrogen molecule in the $\text{Ar}(\text{H}_2)_2$ compound. *Phys. Rev. B* **66**, 144303 (2002).

- [104] Bendtsen, J. The rotational and rotation-vibrational Raman spectra of $^{14}\text{N}_2$, $^{14}\text{N}^{15}\text{N}$ and $^{15}\text{N}_2$. *J. Raman Spectr.* **2**, 133145 (1974).
- [105] Ouillon, R., Turc, C., Lemaistre, J. P. & Ranson, P. High resolution Raman spectroscopy in the α and β crystalline phases of N_2 . *J. Chem. Phys.* **93**, 3005 (1990).
- [106] Lobban, C., Finney, J. L. & Kuhs, W. F. The p-T dependency of the ice II crystal structure and the effect of helium inclusion. *J. Chem. Phys.* **117**, 3928-3934 (2002).
- [107] Schlichtenmayer, M. & Hirscher, M. The usable capacity of porous materials for hydrogen storage. *Appl. Phys. A* **122**, 379 (2016).
- [108] Grazzi, F. & Ulivi, L. Measurements of the ortho-to-para hydrogen conversion in the high-pressure compound $\text{Ar}(\text{H}_2)_2$. *Europhys. Lett.* **52**, 564-570 (2000).
- [109] Ulivi, L., Celli, M., Giannasi, A., Ramirez-Cuesta, A. J. & Zoppi, M. Inelastic neutron scattering from hydrogen clathrate hydrates. *J. Phys. Cond. Mat.* **20**, 104242 (2008).
- [110] Li, J. Inelastic neutron scattering studies of hydrogen bonding in ices. *J. Chem. Phys.* **105**, 6733-6755 (1996).
- [111] Breuer, N. Determination of the phonon spectrum from coherent neutron scattering by polycrystals. *Zeits. Phys.*, **271**, 289-293 (1974).
- [112] Qian, G. R., Lyakhov, A. O., Zhu, Q., Oganov, A. R. & Dong, X. Novel hydrogen hydrate structures under pressure. *Sci. Rep.* **4**, 5606 (2014).
- [113] Kumar, R., Klug, D. D., Ratcliffe, C. I., Tulk, C. A. & Ripmeester, J. A. Low-pressure synthesis and characterization of hydrogen-filled ice Ic. *Angew. Chem.* **125**, 1571-1574 (2013).

-
- [114] Larson, A. C. & Von Dreele, R. B. General Structure Analysis System (GSAS). *Los Alamos Nat. Lab. Rep. LAUR*, 86-748 (2004).
- [115] Toby, B. H. R factors in Rietveld analysis: How good is good enough? *Powder Diffraction*. **21**, 67-70 (2006).
- [116] Rottger, K., Endriss, A., Ihringer, J., Doyle, S. & Kuhs, W. F. Lattice constants and thermal expansion of H₂O and D₂O ice *Ih* Between 10 and 265 K. *Acta Cryst.* **B50**, 644-648 (1994), and addendum *Acta Cryst.* **B68**, 91 (2012).
- [117] Watanabe, N., Asano, H., Iwasa, H., Satoh, S., Murata, H., Karahashi, K., Tomiyoshi, S., Izumi, F. & Inoue, K. High resolution neutron powder diffractometer with a solid methane moderator at pulsed spallation neutron source. *Jap. J. Appl. Phys.* **26**, 1164-1169 (1987).
- [118] Alavi, S., Ripmeester, J. A. & Klug, D. D. Molecular-Dynamics study of structure II hydrogen clathrates. *J. Chem. Phys.* **123**, 024507 (2005).



Acknowledgements

I want to sincerely thank my supervisor Dr. Lorenzo Ulivi (ISC-CNR) and Dr. Milva Celli (ISC-CNR) for believing in my abilities and shared the enthusiasm in the research. I'm also really grateful for the support of Dr. Francesco Grazzi (ISC-CNR) in the analysis of the X-rays and neutron diffraction data and of Dr. Daniele Colognesi (ISC-CNR) as careful co-investigator in the neutron scattering experiments. The skilful technical work of Mr. Andrea Donati (ISC-CNR) has been precious for this experimental work and I sincerely want to thank him. Moreover, I thank all the personnel at the Centro di Cristallografia CRIST (University of Florence) for their assistance in the X-rays measurements, the STFC for the neutron beam time granted at the ISIS (RAL, U.K.) spallation source, Dr. Svemir Rudić (TOSCA instrument scientist) and Dr. Victoria Garcia-Sakai (OSIRIS instrument scientist) for their kind technical support, and the ISIS sample environment team for their highly professional work. Fruitful discussions about neutron diffraction with Prof. Michele Catti, (University of Milano Bicocca) are gratefully acknowledged.

I want to thank my family (Anna Maria, Daniele, Nicolò) and my life partner Martina because they allow me to be who I am, my friends (on and off the tatami) because I can always learn with them and Sensei Munenori Shiigi for his kindness.

Leonardo del Rosso

Sesto Fiorentino, 16/01/2017

“Be strong, be gentle, be beautiful”
[Keiko Fukuda]